THESIS FOR THE DEGREE OF DOCTOR OF PHILOSOPHY

Mass Transport via Thermoplasmonics

STEVEN C. JONES

Department of Physics
CHALMERS UNIVERSITY OF TECHNOLOGY
Gothenburg, Sweden 2020

Mass Transport via Thermoplasmonics
Steven Jones

© Steven Jones, 2020
ISBN 978-91-7905-395-6

Doktorsavhandlingar vid Chalmers tekniska högskola, Ny serie nr 4862
ISSN 0346-718X

Division of Nano & Biophysics
Department of Physics
Chalmers University of Technology
SE-412 96 Göteborg
Sweden
Telephone: +46 (0)31 – 772 10 00

Printed in Sweden by
Chalmers Reproservice
Chalmers Tekniska Högskola
Göteborg, Sweden, 2020

Mass Transport via Thermoplasmonics

Steven Jones
Department of Physics
Chalmers University of Technology

Abstract

When a metallic nanoparticle is illuminated with light under resonant conditions, the free electron gas oscillates in such a way that substantial amplification of the local electric field amplitude is achieved – this is known as a plasmonic resonance. This resonance enhances both the optical scattering as well as absorption. In many applications, the enhanced scattering can facilitate efficient coupling between the near-field and the far-field, which enables optical interrogation of nanoscale volumes. Simultaneously, however, the enhanced absorption results in localized heating and substantial temperature gradients. The resulting temperature profile can drive other thermal processes, some beneficial others detrimental. Thermoplasmonics is the study of these plasmonically enhanced thermal processes.

Elevated temperatures increase the Brownian motion of small particles. Moreover, if large temperature gradients are present, then a process known as *thermophoresis* is likely to occur. Thermophoresis tends to cause a local depletion of Brownian particles around a hot region. From the context of "conventional" plasmonic applications (like molecular sensing), these thermally driven mass transport mechanisms are adverse side effects since they reduce the interaction rate between the plasmonic system and the analyte. An investigation of thermal effects in *plasmonic optical tweezers* showed that the increased Brownian motion essentially negated the optical tweezing effect, resulting in an overall insensitivity between the resonance condition of the antenna and the particle confinement when evaluated in terms of the local temperature increase. Additionally, a significant thermophoretic depletion of analytes occurred, extending tens of microns from the plasmonic structure. This depletion acts in opposition to the plasmonically enhanced optical forces, which are restricted to a region of only a few hundred nanometres.

However, thermoplasmonic effects can also be used for advantageous means. Once example is by driving *thermocapillary flows* directed towards the plasmonic system, thereby facilitating the efficient accumulation of analytes. One method of employing this effect is to superheat a plasmonic particle to a high enough temperature such that a bubble is nucleated. Once a bubble is formed, thermocapillary effects at the bubble interface drive fluid motion with a flow profile similar to that of a *Stokeslet*. This fluid flow can be utilized for analyte accumulation near the plasmonic structure. In addition to the thermocapillary induced flow, it was found that even more intense flow speeds were achieved immediately upon nucleation due to the mechanical action of the bubble. This transient peak in flow speed was approximately an order of magnitude faster than the subsequent persistent (thermocapillary) flow. By designing the plasmonic nanoparticle so that the Laplace pressure restricted the ultimate bubble size, these bubbles could be kept small enough to permit high modulation rates and maximize the relative effect of the peak transient flow.

Keywords: thermoplasmonics, thermophoresis, plasmonic tweezers, bubbles, Stokeslet, thermocapillary, microfluidics

List of Publications

LIST OF PUBLICATIONS INCLUDED IN THIS THESIS
This thesis is based on the work contained in the following papers.
Contributions by the author are included below each work.

i. **Photothermal Heating of Plasmonic Nanoantennas: Influence on Trapped Particle Dynamics and Colloid Distribution**
Steven Jones, Daniel Andrén, Pawel Karpinski, & Mikael Käll
ACS Photonics, **5**, 2878-2887 (2018).
- Contributed to conceptual design, designed & built the experimental setup, designed and simulated plasmonic structures (optical and thermal response), created experimental control software, performed all experiments and data analysis, and wrote the initial manuscript.

ii. **Ultrafast Modulation of Thermoplasmonic Nano-Bubbles in Water**
Steven Jones, Daniel Andrén, Tomasz J. Antosiewicz, & Mikael Käll
Nano Letters, **19**, 8294-8302 (2019).
- Contributed to conceptual design, designed & built the experimental setup, designed and simulated plasmonic structures (optical and thermal response), created experimental control software, performed all experiments and data analysis, and wrote the initial manuscript.

iii. **Strong Transient Flows Generated by Thermoplasmonic Bubble Nucleation**
Steven Jones, Daniel Andrén, Tomasz J. Antosiewicz, Alexander Stilgoe, Halina Rubinsztein-Dunlop, & Mikael Käll
Submitted (arxiv.org/abs/2009.01547)
- Contributed to conceptual design, designed & built the experimental setup, designed and simulated plasmonic structures (optical and thermal response), created experimental control software, performed all experiments and data analysis, and wrote the initial manuscript.

LIST OF PUBLICATIONS NOT INCLUDED IN THIS THESIS

i. **Optically Controlled Stochastic Jumps of Individual Gold Nanorod Rotary Motors**
Lei Shao, Daniel Andrén, Steven Jones, Peter Johansson, & Mikael Käll
Physical Review B, **98**, 085404-6 (2018).

ii. **Counter-Propagating Optical Trapping of Resonant Nanoparticles Using a Uniaxial Crystal**
Pawel Karpinski, Steven Jones, Daniel Andrén, & Mikael Käll
Laser & Photonics Reviews, **12**, 1800139-5 (2018).

iii. **Surface Interactions of Gold Nanoparticles Optically Trapped Against an Interface**
Daniel Andrén, Nils Odebo Länk, Hana Šípová-Jungová, Steven Jones, & Mikael Käll
The Journal of Physical Chemistry C, **123**, 16406-16414 (2019).

iv. **Nanoscale Inorganic Motors Driven by Light: Principles, Realizations, and Opportunities**
Hana Šípová-Jungová, Daniel Andrén, Steven Jones, & Mikael Käll
Chemical Reviews, **120**, 269-287 (2019).

v. **Low-loss Hybrid High-index Dielectric Particles on a Mirror for Extreme Light Confinement**
Aili Maimaiti, Partha Pratim Patra, Steven Jones, Tomasz J. Antosiewicz, & Ruggero Verre
Advanced Optical Materials, **8**, 1901820-9 (2020).

vi. **Optical Rotation and Thermometry of Laser Tweezed Silicon Nanorods**
Pawel Karpinski, Steven Jones, Hana Šípová-Jungová, Ruggero Verre, & Mikael Käll
Nano Letters, **20**, 6494-6501 (2020).

Acknowledgements

If I were to give proper credit to all who deserve it, this thesis would likely double in size. With that said, I will see what I can fit within one page.

To my loving parents. Your steadfast support throughout my academic career (and the rest of my life) has made this possible. My gratitude is beyond words.

To my loving wife. Thank you for being you and all that entails.

Daniel. I think by this point, it goes without saying. Thanks for everything bud.

Mikael. I could not imagine a better supervisor. I am eternally grateful for your tutelage. I hope we keep in contact.

Tomasz. I think there is consensus in the global community that the worst part of this whole pandemic is that it cancelled your next visit and our trip to the pub.

Hana. I am super happy to see your beautiful family growing in leaps and bounds. Do not forget about science though. Science loves you too.

Halina & Alex. Thanks for having me out to Brisbane and teaching me so much. It was a pleasure working with you two.

Nils. Miss you bud, hope to see you around sometime. Congrats on the kid.

Ruggero. Best of luck on your new path. I am sure wherever you go, and whatever you do, your jubilant charm will always bring you happiness.

Reuven. Thanks for getting me started with this whole science thing. I hope to see you again soon.

Pantea & Mahdi. I look forward to keeping tabs on your two as you go through this journey. I know you will do well.

Peter Apell. It is always a pleasure to see you. Thanks for the book!

Noemi, Pawel, Ximin, Srdjan, Timur, Denis, Battulga, Adriana, Kate, Betül, Martin, Benjamin, Lei, Peter Johansen, Lin, Peter, and everyone else I have been fortunate enough to know from BNP and Chalmers/GU. Thanks for everything. It has been a blast.

Steven Jones
2020.10.21

“The iron is the great reference point, the all-knowing perspective giver.
Always there like a beacon in the pitch black.”

- Henry Rollins

Contents

Mass Transport via Thermoplasmonics

1 Introduction

What is thermoplasmonics?

Thermoplasmonics is the amalgamation of two fields: thermodynamics and plasmonics. Before proceeding, let us first examine the general concept of each of these subfields and then go on to define "thermoplasmonics" within the scope of this thesis.

Plasmonics describes the interaction between light and highly conductive metallic nanostructures (e.g. nanoparticles made from noble metals such as gold or silver). The way that these nanostructures interact with light is fundamentally the same as all other light-matter interactions. The only difference is that due to their geometric properties (size and shape) and their material properties (electric permittivity), these interactions are strongly enhanced. This enhancement essentially means that these "plasmonic structures" act as efficient antennas for visible and near-infrared light. As a result, these antennas facilitate interactions between light and nanoscale objects that would otherwise be incredibly inefficient.(*1–3*) In general, most of these applications have focused on the optical properties of these metallic nanostructures, i.e. the plasmonically enhanced *scattering*.

Thermodynamics, in its most generic form, is the study of heat transfer and other thermally driven processes. Thermodynamics is an immense field that covers everything from engines and refrigerators, to chemical reaction rates and the motion of microscopic particles. Thermodynamics essentially looks at macroscopic properties (e.g. temperature) which are the result of microscopic activity (e.g. atomic/molecular vibrations). Thermodynamics uses these macroscopic properties to describe the behaviour of a system without needing to concern itself with the specifics of individual microscopic actors.

Thermoplasmonics thus concerns itself with the intersection of these two fields. To state it another way, it can be said that thermoplasmonics deals with the thermodynamic consequences that arise as a result of plasmonically enhanced optical interactions. While *plasmonics* is often focused on optical scattering, *thermoplasmonics* is more concerned about the plasmonically enhanced heating via *absorption.*

Why is thermoplasmonics interesting?

When light interacts with plasmonic structures, both scattering and absorption always occur to varying degrees. The scattering enables light to couple between the optical near-field and far-field, helping researchers manipulate/interrogate nanoscale environments with standard optical techniques. When light is absorbed, however, this results in localized heating. Because of the strong light-

matter interaction, this local heating can often lead to a very significant temperature increase that drives other thermodynamic processes; some intended, others unintended; some beneficial, others detrimental. In this way, thermoplasmonics deals with both "good" and "bad" aspects of these thermally driven effects.

A typical application of plasmonics is to utilize gold nanoparticles to monitor biological interactions. The illumination of these nanoantennas is thus necessary to optically monitor the surrounding environment. However, if plasmonically enhanced absorption causes the local temperature to increase beyond acceptable levels, then adverse thermodynamic effects can occur. Such "adverse effects" include changing the biomolecule behaviour (e.g. increased Brownian motion) or even resulting in thermally induced damage. For this reason, it is imperative to study these thermoplasmonic consequences so that they can be mitigated or accounted for.

Conversely, various thermally driven phenomena exist, which can be extremely beneficial.(*4–11*) For example, using thermoplasmonic effects, one can generate localized fluid flow for efficient particle transport, thereby increasing the interaction rate between sensors and analytes. Often in the aforementioned plasmonic systems, one wishes to detect analytes at low concentrations. However, under standard conditions, this would require prohibitively long signal integration times. Thus by using thermoplasmonically driven mass transport, this limitation can potentially be overcome.

This dichotomy between "good" and "bad" effects in thermoplasmonics is really at the heart of this field. Plasmonically enhanced absorption often results in undesirable consequences, and the study of thermoplasmonics can help avoid these pitfalls. Meanwhile, there are exciting new opportunities to utilize thermally driven processes facilitated by plasmonic absorption.

Model system

For the "theory" section of this thesis, the following framework will be frequently used for pedagogical purposes (with ad-hoc modifications). Consider a gold nanosphere, which is the prototypical plasmonic nanoantenna. This gold nanosphere is attached to a glass substrate and immersed in water while being illuminated with light. The situation is schematically illustrated in Figure 1. This simple example is representative of many common plasmonic sensing platforms and will provide a useful model for further discussion on the theory behind thermoplasmonics. It is essential to note that in this thesis, the discussion will be about continuous wave (CW) illumination and not pulsed illumination. The main distinction between these two scenarios is that transient optical effects are generally inconsequential in the CW regime.

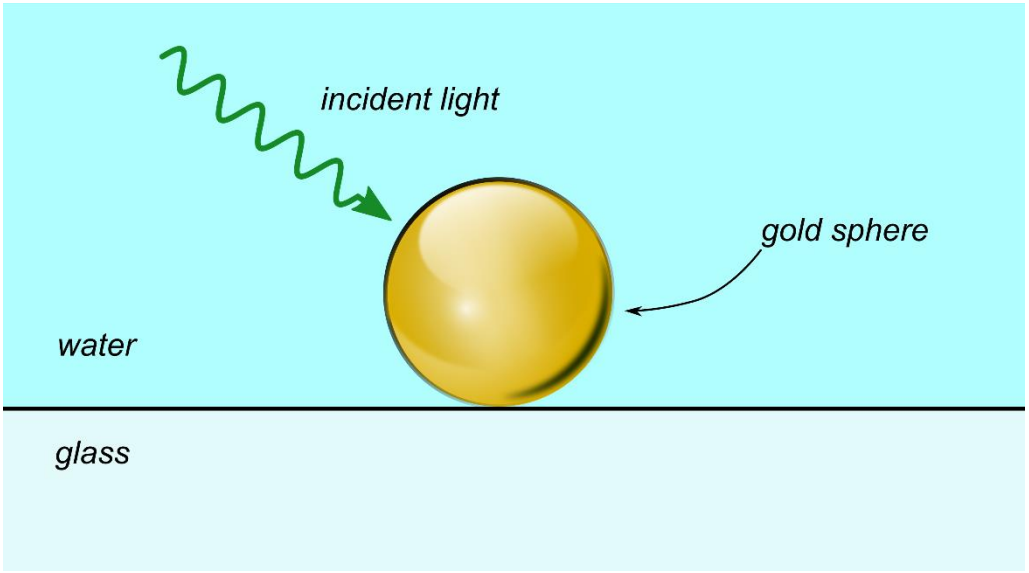

Figure 1 Model system: a gold sphere, illuminated by light, lying on a glass substrate, and immersed in water.

2 Theory - Thermoplasmonics

A general overview of the main concepts in thermoplasmonics is illustrated in Figure 2. The discussion will begin with light-matter interactions, including an overview of the relevant material properties before proceeding to the most crucial optical interaction mechanisms. Next, heat transfer is considered, which details how the energy dissipated due to optical absorption results in establishing a local increase in temperature. Finally, the concept of thermally induced phase changes is covered with a specific emphasis on the liquid to gas transition, which is particularly relevant for this thesis.

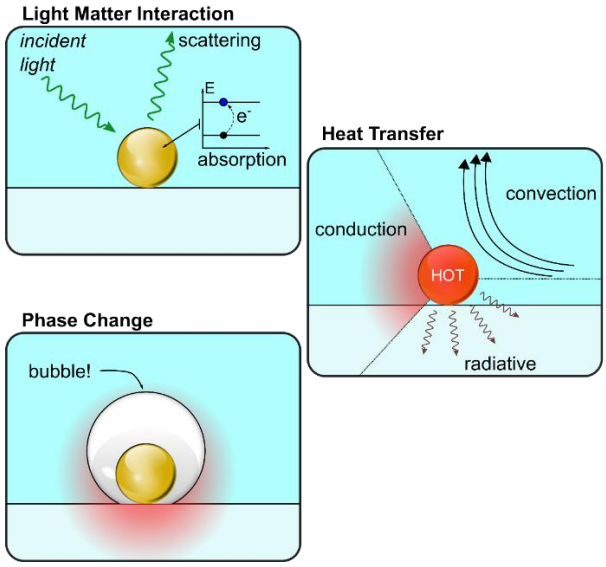

Figure 2 Overview of thermoplasmonic processes covered in this thesis. Top: light-matter interactions. Right: Heat transfer. Bottom; Thermally induced phase changes.

2.1 Light-Matter Interaction

The subject of light-matter interaction is a vast field that covers everything from the motion of a charged elementary particle in an oscillating electric field to exotic nonlinear effects such as second harmonic generation. For this thesis, the discussion is restricted to the effects most relevant within the context of the model system introduced in section 1. Specifically, we are primarily concerned with light that propagates through a homogeneous medium and interacts with a small object (e.g. a sphere). We will consider two fundamental processes: scattering and absorption. The relevant concepts are introduced generally before proceeding to develop them for the task at hand. In this section, we are mainly concerned with the "plasmonics" part of "thermoplasmonics."

What is light?

As preparation for our discussion, it is constructive to introduce the concept of light and some necessary notation. Light, in its simplest terms, is an oscillating wave of electromagnetic energy that propagates in space. It consists of an electric and magnetic field that oscillates in phase with one another. The direction of

oscillation of both the electric and magnetic fields are orthogonal to one another and the direction of propagation. Light propagates forward in a vacuum at the speed $c_0 \approx 3 \times 10^8$ m/s. By knowing the frequency, f, of these oscillations, as well as the speed of propagation, we can define the *wavelength* of light as the distance travelled over which one oscillation occurs, i.e.[1]

$$\lambda_0 = \frac{c_0}{f}. \qquad 2\text{-}1$$

For the applications discussed here, the interaction between light and matter is dominated by electric interactions, and thus it is often sufficient to consider only the oscillating electric field. The propagation of an oscillating electric field is described by[2]

$$\vec{E}(\vec{r},t) = \vec{E}_0 \cos\left(-\omega t + \vec{k}\cdot\vec{r} + \phi\right) = \mathcal{R}e\left\{\vec{E}_0 e^{i\left(-\omega t + \vec{k}\cdot\vec{r} + \phi\right)}\right\}, \qquad 2\text{-}2$$

where $\vec{E}$ is the electric field amplitude a time t and location $\vec{r}$, while $\vec{E}_0$ is the amplitude of the electric field oscillations. The term $\omega = 2\pi f$ is simply the frequency-converted from Hz into rad/s, and $\vec{k}$ is known as the wavevector, which describes the direction of propagation with a magnitude given by $\left|\vec{k}\right| = 2\pi/\lambda_0$. The constant ϕ is simply the relative phase offset of the oscillation determined by the electric field amplitude at $t = 0$ and $r = 0$.

Thus far, we have implicitly been discussing electromagnetic radiation (EMR) in general. The distinction between *light* and *EMR* is merely one of convention, where light is usually taken as the region of the electromagnetic spectrum which we can detect with our eyes, i.e. $\lambda_0 \approx 400 - 700$ nm. Fundamentally there is no difference between the radio waves ($\lambda_0 \approx 1$ mm $- 100$ km) and visible light, except for the way the EMR interacts with matter. Light-matter interaction depends on the wavelength/frequency of the EMR and the size/shape and material properties of the illuminated object. For this text, we will extend the conventional definition of light to around $\lambda_0 \approx 0.4 - 1.5$ μm, which includes both visible light and part of the near-infrared region of the EMR spectrum. Generally speaking, visible and near-infrared light behave nominally the same during light-matter interactions. The only significant difference is whether or not we can see the effects with the naked eye.

[1] λ_0 is used to denote the wavelength of light propagating in free space (i.e. vacuum) as opposed to when propagating through a homogeneous medium that is not vacuum.

[2] The description of light propagation given in equation 2-2 is for that of an infinite plane wave. Although this model is limited in its applicability to many "real" situations, it will be sufficient for much of the following discussion on light-matter interaction.

2.1.1 Optical Properties of Materials

To describe the interaction of an object/medium with light, we need only one material parameter:[3] the permittivity. The permittivity, ε, determines the displacement field that arises in a medium in response to an applied electric field, i.e.

$$\mathcal{D} = \varepsilon E = \varepsilon_0 E + \mathcal{P}\,, \qquad 2\text{-}3$$

where $\mathcal{D}$ is the displacement field, ε_0 is the permittivity of free space, and $\mathcal{P}$ is the macroscopic polarization density. The displacement field describes the response of both free and bound charges. Since the material cannot respond instantaneously to a change in the applied field, a phase difference must exist between $\mathcal{D}$ and E, thus implying that the permittivity must be complex-valued. We express the permittivity as[4]

$$\varepsilon(\omega) = \varepsilon_{\mathrm{r}}(\omega)\varepsilon_0 \qquad 2\text{-}4$$

with

$$\varepsilon_{\mathrm{r}}(\omega) = \varepsilon'(\omega) + i\varepsilon''(\omega)\,, \qquad 2\text{-}5$$

where ε_0 is the permittivity of free space and ε_{r} is the *relative* permittivity. For the dielectric materials considered here, the material response is fast enough to approximate the permittivity as constant and real-valued at optical wavelengths.[5] For conductive metals, on the other hand, this assumption cannot be made.

To first order, two main mechanisms dictate the permittivity of conductive metals under optical excitation: the response of conduction band electrons and interband transitions.(*12*) The effect of conduction electrons can be derived by determining the response of free electrons under the influence of an external oscillating electric field. We can thus solve the Lagrange equation for the Polarization density. This analysis results in the Drude-Sommerfeld model for the relative permittivity:

$$\varepsilon_{\mathrm{Drude}}(\omega) = 1 - \frac{\Omega_{\mathrm{c}}^2}{\omega(\omega + i\Gamma_{\mathrm{c}})}\,, \qquad 2\text{-}6$$

[3] Assuming we are restricting ourselves to purely electric interactions, otherwise the permeability would also be required.
[4] In general the permittivity is a function of state but for now we will just consider the frequency dependence.
[5] The term “optical” a synonym for visible in this context and the two terms will be used interchangeably.

where Ω_c is the plasma frequency of conduction band electrons,[6] and Γ_c accounts for losses.[7] Generally, an additional offset is added to the Drude-Sommerfeld model to account for the residual polarization coming from the positive ion cores, i.e.

$$\varepsilon_{\text{Drude}}(\omega) = \varepsilon_\infty - \frac{\Omega_c^2}{\omega(\omega + i\Gamma_c)}. \qquad 2\text{-}7$$

For the second mechanism, interband transitions, this type of response occurs when the incident photons have an energy greater than the energy gap between different electronic bands, thus causing bound electrons to transition to the conduction band. To account for this effect, we can use a generalized Lorentzian term

$$\varepsilon_{\text{Lorentz}}(\omega) = \frac{\Delta\varepsilon\Omega_v^2}{\Omega_v^2 - \omega^2 - i\Gamma_v\omega}, \qquad 2\text{-}8$$

where Ω_v and Γ_v are the plasma and damping frequencies of the bound electrons, and $\Delta\varepsilon$ accounts for the relative strength of the interband transitions in determining the permittivity. By combining equations 2-7 and 2-8, we obtain the Drude-Lorentz model. This phenomenologically driven equation is a suitable approximation for the experimentally observed permittivity of important plasmonic metals (e.g. gold) over our range of interest. See Figure 3 below for the permittivity of gold (experimental data from ref(*13*)).

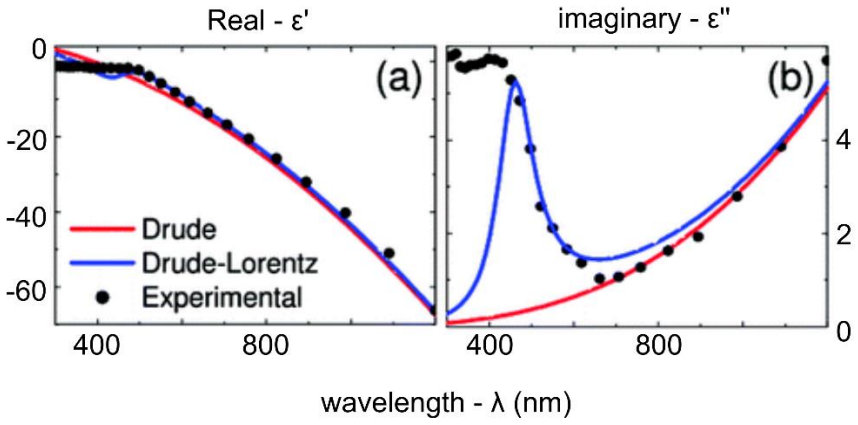

Figure 3 Permittivity of gold. Shown here are the real (top) and imaginary (bottom) permittivity of gold within the wavelength range of interest. The Drude model well encapsulates the data at longer wavelengths while the Drude-Lorentz model is needed to account for interband transitions that become significant for wavelengths less than $600\,nm$*. In principle, multiple Lorentz terms can be incorporated to fit the data better by describing different interband transitions. Adapted with permission from ref(12) Copyright 2011 American Chemical Society.*

[6] $\Omega_c = nq_e^2/\varepsilon_0 m_e$; n is the charge density, q_e is the charge of electrons, and m_e is the effective electron mass.
[7] $\Gamma_c = 1/\tau_c$ where τ_c is the relaxation time of the free electron gas.

The final point to discuss with regards to the optical properties of matter is the refractive index. The refractive index (n) is not a *new* optical property but rather a repackaging of the permittivity. However, it is useful in many scenarios and often more intuitive to work with, mainly when dealing with dielectrics. Starting from the permittivity of a material, we can extract the refractive index as[8]

$$n = \sqrt{\varepsilon_{\mathrm{r}}}\,. \qquad 2\text{-}9$$

The refractive index is often viewed as the optical "density" of a material since it determines the wavelength and speed of light that propagates through that material, i.e. $\lambda = \lambda_0/n$ and $c = c_0/n$.[9] In general, the refractive index is also complex-valued with the real part describing the propagation velocity/wavelength while the imaginary part (also called the extinction coefficient) dictates the attenuation of the wave as it propagates.

2.1.2 Scattering and Absorption

Among the most fundamental light-matter interactions are scattering and absorption. Scattering is the process where an object is illuminated with light, and the object radiates that light back into the surrounding medium with the same energy but in different directions. Absorption, on the other hand, occurs when the incident light causes either an electronic or vibrational transition within the object, and the energy of the incident photon is retained within the object.[10] These processes are illustrated in Figure 4 below. Here we consider the case of scattering/absorption by a spherical particle in a homogeneous dielectric medium.

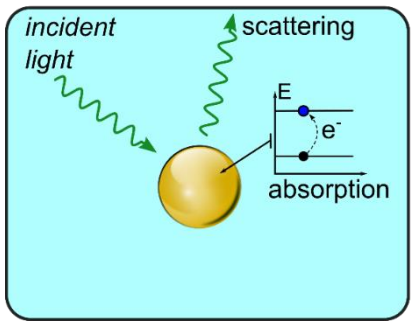

Figure 4 Optical scattering and absorption by a particle in a homogeneous medium. Note that the energy level diagram is for illustrative purposes only and is not representative of the absorption process in gold.

[8] This is for the case where we deal only with electric interactions. If magnetic contributions are included, then $n = \sqrt{\varepsilon_r \mu_r}$ where μ_r is the permeability of a material which is essentially the magnetic analog to the permittivity. For all materials considered in this thesis we can make the approximation $\mu_r = 1$.

[9] Here when we talk about the *speed* of light in a medium, we are referring to the phase velocity of the oscillating field.

[10] After being absorbed, this energy is subsequently dissipated as heat causing a local temperature increase. This process is the primary mechanism that is of interest in thermoplasmonics and is discussed further in section 2.2.

Three general regimes need to be considered: $\lambda \gg a$, $\lambda \approx a$, and $\lambda \ll a$ – where a is the radius of the sphere. In the first regime ($\lambda \gg a$), we can assume that the electric field is constant over the volume of the particle at any point in time. This constraint allows one to solve the system using the quasi-static approximation and is generally representative of nanoparticles with $a \leq 50$ nm.(*14*) In the second regime ($\lambda \approx a$), exact solutions exist using Mie theory, which expands the incident plane wave and scattered field into spherical harmonics. In the last regime, $\lambda \ll a$, the interface of the particle can be approximated as flat (locally), and the Fresnel equations can be used to determine how light propagates.

For thermoplasmonics, we are generally interested in the first and second regimes. However, for most *real* situations, numerical methods, such as finite difference time domain or finite element method, are required if accuracy is needed in anything other than the simplest of geometries (e.g. if the particle is not spherical/ellipsoidal). Therefore, we will restrict ourselves to the first regime (also known as the "Rayleigh" regime) since it provides instructive results without the need for overly cumbersome mathematics.

In the Rayleigh approach, we first solve the Laplace equation of the system $\nabla^2\Phi = 0$, where Φ is the electric potential. This allows us to calculate the electric field distribution, $\vec{E} = -\nabla\Phi$, assuming a static external electric field as illustrated in Figure 5a. Following the method of Jackson,(*15*) the general solution for a Laplace equation possessing azimuthal symmetry is (in spherical coordinates)

$$\Phi(r,\varphi) = \sum_{l=0}^{\infty} [A_l r^l + B_l r^{-l-1}]\, \mathbb{P}_l(\cos(\varphi))\,, \qquad 2\text{-}10$$

where A_l and B_l are coefficients that can be determined from the boundary conditions and $\mathbb{P}_l$ is the Legendre polynomial (order l) with argument $\cos(\varphi)$ – φ being the angle between the position vector and the electric field vector.

We now break the problem into finding the solution "inside" and "outside" of the sphere. Within the sphere, we require that the potential be finite everywhere and thus $B_{l,\text{in}} = 0\ \forall\ l$ (since the term r^{-l-1} is divergent as $r \to 0$). The next boundary condition we employ is that as $r \to \infty$ the potential must tend to $\Phi_{\text{out}} \to -E_0 r\cos(\varphi)$. Therefore, $A_{l,\text{out}} = 0\ \forall\ l \neq 1$, and $A_{1,\text{out}} = -E_0$ at $l = 1$.[11] By Faraday's law, we know that the tangential component of the electric field is continuous across the interface, therefore at $r = a$ we have

[11] Note, $\mathbb{P}_1(\cos(\varphi)) = \cos(\varphi)$.

$$\frac{\partial \Phi_{\text{in}}}{\partial \varphi} = \frac{\partial \Phi_{\text{out}}}{\partial \varphi} \ . \qquad 2\text{-}11$$

Since there are no unbound charges, the normal displacement field must also be continuous across the interface, i.e.

$$\varepsilon_r \frac{\partial \Phi_{\text{in}}}{\partial r} = \varepsilon_{\text{m}} \frac{\partial \Phi_{\text{out}}}{\partial r} , \qquad 2\text{-}12$$

where ε_{r} is the complex permittivity of the particle, and ε_{m} is the relative permittivity of the surrounding medium.[12] Since $B_{l,\text{in}} = 0 \ \forall \ l$ and $A_{l,\text{in}} = 0 \ \forall \ l \neq 1$ then $A_{l,\text{in}} = B_{l,\text{out}} = 0 \ \forall \ l \neq 1$. Solving equations 2-11 and 2-12 at $r = a$ and $l = 1$ determines the remaining non-zero coefficients and the resulting potential is given by

$$\Phi_{\text{in}} = -E_0 \frac{3\varepsilon_{\text{m}}}{\varepsilon_r + 2\varepsilon_{\text{m}}} r \cos(\varphi) \qquad 2\text{-}13$$

and

$$\Phi_{\text{out}} = -E_0 r \cos(\varphi) + E_0 \frac{\varepsilon_{\text{r}} - \varepsilon_{\text{m}}}{\varepsilon_{\text{r}} + 2\varepsilon_{\text{m}}} \frac{a^3}{r^2} \cos(\varphi) \ . \qquad 2\text{-}14$$

Equation 2-14 is simply a superposition of the incident field (first term) and a dipole (second term). Explicitly writing out equation 2-14 in vectorial form and highlighting the dipolar nature of the second term, i.e.

$$\Phi_{\text{out}} = -\vec{E}_0 \cdot \vec{r} + \frac{\vec{p} \cdot \vec{r}}{4\pi\varepsilon_0 \varepsilon_{\text{m}} r^2} , \qquad 2\text{-}15$$

where $\vec{p}$ is the dipole moment induced in the sphere,(*16*)

$$\vec{p} = 4\pi\varepsilon_0 \varepsilon_{\text{m}} a^3 \frac{\varepsilon_{\text{r}} - \varepsilon_{\text{m}}}{\varepsilon_{\text{r}} + 2\varepsilon_{\text{m}}} \vec{E}_0 \ . \qquad 2\text{-}16$$

We can now introduce the *polarizability* of the particle, α, as defined by the equation

$$\vec{p} = \varepsilon_0 \varepsilon_{\text{m}} \alpha \vec{E}_0 , \qquad 2\text{-}17$$

with the polarizability[13] given explicitly as

[12] For our purposes ε_{m} can be assumed to be real-valued and constant.
[13] Technically this is a polarizability volume.

$$\alpha = 4\pi a^3 \frac{\varepsilon_\mathrm{r} - \varepsilon_\mathrm{m}}{\varepsilon_\mathrm{r} + 2\varepsilon_\mathrm{m}}. \qquad 2\text{-}18$$

The electric field corresponding to the potential given in equations 2-13 and 2-14 is given by

$$\vec{E}_\mathrm{in} = \frac{3\varepsilon_\mathrm{m}}{\varepsilon_\mathrm{r} + 2\varepsilon_\mathrm{m}} \vec{E}_0 \qquad 2\text{-}19$$

and

$$\vec{E}_\mathrm{out} = \vec{E}_0 + \frac{3\hat{r}(\hat{r} \cdot \vec{p}) - \vec{p}}{4\pi\varepsilon_0\varepsilon_\mathrm{m} r^3}, \qquad 2\text{-}20$$

with $\hat{r}$ denoting the unit vector parallel to $\vec{r}$. The electric field near a sphere in a static external field is plotted in Figure 5b. Essentially, the above states that under the influence of an external electric field, the particle acts as a dipole aligned parallel to the external field.

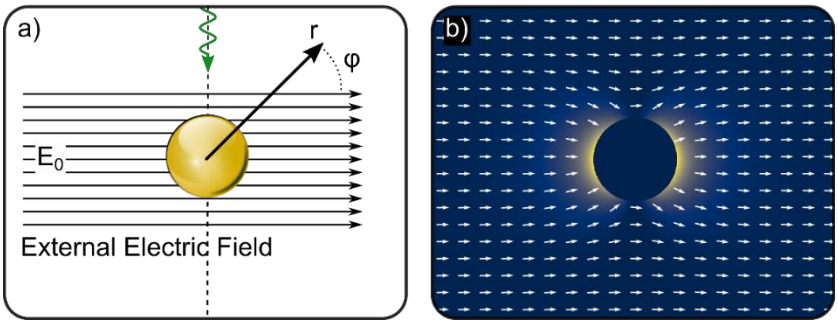

Figure 5 Static solution to a spherical particle in a uniform external electric field. a) Illustration of the example considered. A plane wave propagates along the optical axis (dotted line) past a sphere in a homogeneous dielectric medium. The electric field imposed on the sphere by the plane wave is approximated as a static and uniform electric field. b) Resulting electric field distribution according to equations 2-19 and 2-20 for $\varepsilon_m = 2$, $\varepsilon' = -10$, and $\varepsilon'' = 1$.

Thus far, we have been describing the response of a subwavelength sphere to a *static* electric field; however, we wish to understand the response to an oscillating electric field. As outlined by Bohren and Huffman,(*17*) we next assume that in the presence of an oscillating plane wave, it will suffice to replace the sphere by a dipole with the dipole moment given by equation 2-17, but in place of a static electric field we use a plane wave given by equation 2-2 which results in an oscillating dipole $\vec{p} = \varepsilon_0\varepsilon_\mathrm{m}\alpha\vec{E}_0 e^{-i\omega t}$. Additionally, for the polarizability (equation 2-18), we use the frequency-dependent permittivity to calculate the polarizability of the dipole. [14]

[14] The definition of the polarizability given in equation 2-18, known as the Clausius-Mossotti polarizability, does not properly account for the interaction of the particle with its own scattered

In the "far-field,"[15] the electric field radiated or "scattered" by the dipole is given by(*17*)

$$\vec{E}_{\mathrm{scatt}} = -\frac{k^2}{4\pi\varepsilon_{\mathrm{m}} r}[\hat{r} \times (\hat{r} \times \vec{p})]e^{-i(\omega t - kr)} \,. \tag{2-21}$$

This propagating wave carries power determined by its Poynting vector. The scattered field can be approximated by a plane wave at large distances from the sphere; therefore, we can express the cycle averaged Poynting vector as

$$\langle S \rangle = \frac{c_0 n_{\mathrm{m}} \varepsilon_0}{2} |E_{\mathrm{scatt}}|^2 \,. \tag{2-22}$$

If we integrate equation 2-22 over the surface of a large sphere containing the dipole at the origin, we obtain the total power scattered by our sphere ($\dot{Q}_{\mathrm{scatt}} = \oint \langle S \rangle$). Using this total power, we can define a useful quantity, the scattering cross-section (σ_{scatt}), defined by

$$\dot{Q}_{\mathrm{scatt}} = \sigma_{\mathrm{scatt}} I_0 \,, \tag{2-23}$$

where I_0 is the intensity of the incident plane wave,

$$I_0 = \frac{c_0 n_{\mathrm{m}} \varepsilon_0}{2} |E_0|^2 \,. \tag{2-24}$$

The scattering cross-section determines the "efficiency" of the particle at scattering light. For subwavelength particles, it can be rewritten in terms of the polarizability as(*14*)

$$\sigma_{\mathrm{scatt}}(\omega) = \frac{k^4}{6\pi} |\alpha(\omega)|^2 \,. \tag{2-25}$$

Similarly, we can define the absorption cross-section, which defines the amount of incident light that is absorbed by the particle,

$$\dot{Q}_{\mathrm{abs}} = \sigma_{\mathrm{abs}} I_0 \,. \tag{2-26}$$

The heat generated arises due to the Joule effect, the heat source density due to oscillating currents driven by the external electric field is given by(*18*, *19*)

$$\dot{q}(r) = \frac{1}{2} \mathcal{R}e\{J_C^\star(r) \cdot E(r)\} \,, \tag{2-27}$$

---

field in an oscillating external field. See ref(*33*)-chapter 3 for a more detailed derivation of the polarizability including the radiative reaction correction.

[15] i.e. $kr \gg 1$ (many wavelengths away from the dipole).

where $J_C = i\omega\varepsilon_0\varepsilon_r(\omega)E$ is the electric current density. Thus, the heat source density can be rewritten as

$$\dot{q}(r) = \frac{\omega\varepsilon_0}{2}\mathcal{I}m\{\varepsilon_r(\omega)\}|E(r)|^2 . \qquad 2\text{-}28$$

Using the internal electric field from equation 2-19 and integrating over the volume of the sphere to obtain the total power dissipated allows us to write the absorption cross-section in terms of the polarizability as(*14*)

$$\sigma_{\text{abs}} = k\,\mathcal{I}m\{\alpha(\omega)\} . \qquad 2\text{-}29$$

At this point, we can make two general observations. The first observation is that the scattering cross-section is proportional to λ^{-4} while the absorption cross-section is proportional to λ^{-1}. Secondly, the scattering cross-section is proportional to a^6 while the absorption cross-section is proportional to a^3. Thus, all other things being equal,[16] we would expect that absorption and scattering will strictly decrease for smaller particles or longer wavelengths. However, all other things are *not* equal. As we will see in the next section, when we start to consider the specific material properties of plasmonic materials, such as gold, surprising optical behaviour can occur.

2.1.3 Plasmonics

Although we have been nominally discussing plasmonics, the discussion in the previous section has been general. Note that there were no conditions imposed on the material under consideration in the derivation of the polarizability, scattering, or absorption of a subwavelength sphere. Indeed equations 2-18, 2-25, and 2-29 hold for *any* subwavelength particle as long as the internal electric field can be approximated as constant.

From the form of equation 2-18, we can see that a resonance condition is imposed when $\varepsilon_{\text{r}} = -2\varepsilon_{\text{m}}$. For noble metals, such as gold or silver, this condition can be approximately satisfied at optical wavelengths for various important host dielectrics.[17] Shown in Figure 6 is the Rayleigh approximation for the polarizability, absorption cross-section, and scattering cross-section for a 50 nm gold sphere embedded in different dielectric media characterized by ε_{m}. As clearly shown in Figure 6, the absorption and scattering cross-sections deviate significantly from the simple λ^{-4} and λ^{-1} (respective) relations that were predicted previously. These resonances occur because the polarizability of the

[16] i.e. complex permittivity.
[17] Such as air ($\varepsilon = 1$), water ($\varepsilon = 1.77$), or glass ($\varepsilon = 2.1$).

sphere has a strong wavelength dependence, particularly when $\varepsilon_r \approx -2\varepsilon_{\mathrm{m}}$. This is a plasmonic resonance.[18]

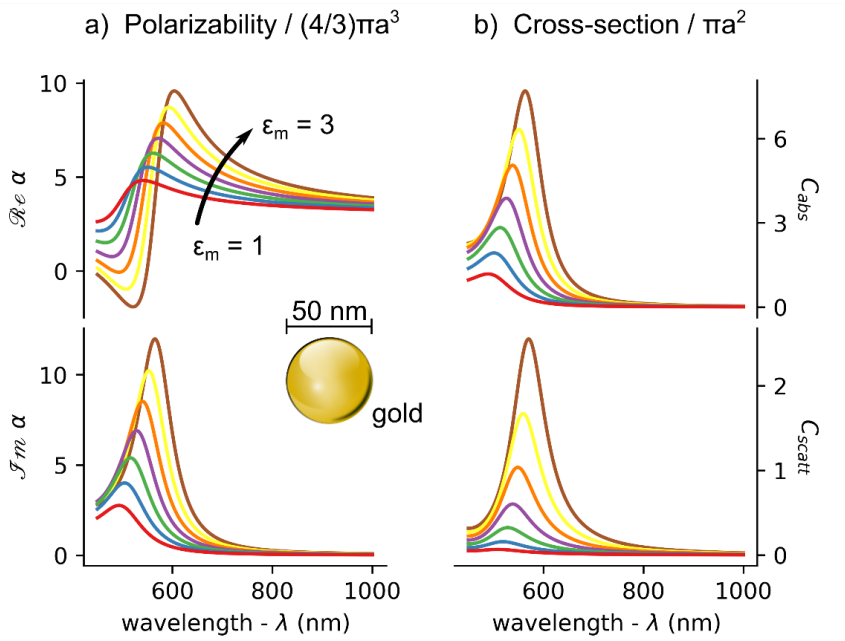

Figure 6 Rayleigh approximation of polarizability and cross-sections for a 50 nm gold sphere. a) Polarizability normalized by volume (real – top, imaginary – bottom) for medium relative permittivities from 1 to 3. b) Optical cross-sections normalized to the geometric cross-section for absorption (top) and scattering (bottom) under the same conditions as a). The permittivity of gold is based on the Drude-Lorentz model from ref(20).

Traditionally, among the most utilized properties of these plasmonic resonances is the scattering enhancement. This has facilitated the development of a plethora of optical sensors based on their ability to couple light between the near-field and the far-field. The electric field near plasmonic particles is strongly enhanced (as illustrated in Figure 5b) and scales approximately with the scattering cross-section. Because of the local electric field enhancement, optically excited plasmonic nanoantennas can interact with nearby particles (such as biomolecules) and then retransmit this signal back into the far-field where it can easily be detected. This property is used for signal enhancement in many spectroscopic interrogation techniques such as surface-enhanced Raman scattering,(*21*) surface-enhanced fluorescence,(*1*) and surface-enhanced infrared absorption spectroscopy.(*22*)

Raman spectroscopy, for instance, is a powerful spectroscopic technique that provides information about the vibrational modes of molecules and bioparticles.(*23*) These vibrational modes are identified as narrow spectral peaks in the inelastically scattered light when a particle is illuminated with a monochromatic light source. Because these spectral peaks can be directly

[18] Strictly speaking this is a *localized* surface plasmon resonance which is distinct from surface plasmon resonances which occur in thin conducting (e.g. gold) films, and volume plasmons which occur in bulk conductive materials.

correlated to individual vibrational modes, the observed spectrum provides information about the molecular structure and acts as a unique spectral fingerprint. The efficiency of this process, however, is typically very weak. By utilizing plasmonic structures, the local electric field is enhanced by a factor E/E_0, which corresponds to an increased interaction efficiency with the analyte of $|E/E_0|^2$. Additionally, the light scattered back into the far-field for collection is also enhanced by a similar factor resulting in an overall signal enhancement on the order of $|E/E_0|^4$.(*24*) Thus, even a modest field enhancement of $10\times$ can result in a signal enhancement on the order of 10^4. With proper structure design[19] (to optimize the electric field enhancement), the collected signal can be enhanced by up to $10^7 - 10^{10}$.(*25*) These levels of enhancements, in both SERS and other spectroscopic techniques, have enabled optical bio/chemical sensors to achieve the "single-molecule limit,"(*26*, *27*) thus greatly facilitating the ability to sense analytes at low concentrations.[20]

Additionally, the changes in the resonance condition of the plasmonic antenna in response to the presence of molecules has also been widely used for sensing. As shown in Figure 6b (bottom), the scattering resonance condition, and therefore peak-scattering wavelength, is highly dependent on the permittivity of the surrounding medium. Due to the localized electric field enhancement, the change in resonance condition is most strongly affected by the immediate vicinity, enabling the plasmonic antenna to act as highly efficient sensors of their local environment – a technique known as localized surface plasmon resonance sensors. In this scheme, the plasmonic structures are illuminated with a broadband light source,[21] and only the scattered light is collected. By monitoring changes in the resonance wavelength, changes in the permittivity of the local environment can be deduced. Depending on the experimental configuration, changes in the resonance condition can be attributed to various physical phenomena. This technique is most often used to monitor molecular binding – also having achieved the level of single-molecule sensitivity.(*28–30*)

Most of the prominent applications of plasmonics utilize the electric field and scattering cross-section enhancements. However, as shown in Figure 6, the absorption cross-section is also greatly enhanced. The majority of absorbed power is dissipated as heat, potentially causing a significant temperature increase (see section 2.2). As discussed in the Introduction, the result of thermally driven phenomena enhanced by the plasmonic absorption can be detrimental for many of the applications described above. However, there are also methods to utilize

[19] Note that "proper structure design" typically requires pairs of plasmonic nanoparticles that are electromagnetically coupled.
[20] However, as we will see later, the "sensing efficiency" is not the only factor that determines the signal rate in detection at low analyte concentrations. In particular the transport rate of analytes becomes significant at low concentrations and thus efficient mass transport is necessary.
[21] i.e. "white" light.

thermal phenomena for entirely new purposes and further optimize the performance of conventional (plasmonic) sensors. The various thermally driven phenomena relevant to this thesis are discussed in section 3.

2.1.4 A Note on Optical Forces

As a prelude to some of the experimental techniques used in this thesis, it is instructive to introduce the concept of optical forces and to make the connection between these forces and the ideas developed in section 2.1.2. Optical forces occur because light carries momentum. Thus, any optical interaction with an object that changes the net momentum of transmitted light (either through scattering or absorption) must, according to the law of conservation of momentum, impart a force on the illuminated object.

To envision this momentum transfer and the associated force, consider a collimated beam of light that strikes a perfect mirror at normal incidence. Each photon of light carries a single quantum of momentum of magnitude h/λ where h is Plank's constant. Upon reflection from the perfect mirror, the photon now travels in the opposite direction with the same momentum, and thus, the net change in momentum per photon is $2h/\lambda$. Alternatively, if the perfect mirror were replaced with a perfectly absorbing material, then the change in momentum would only be h/λ. In either case, to conserve momentum, this change in momentum carried by the light must be accounted for by a change in momentum of the mirror/absorber. If we know the rate of photons striking the surface, we can determine the force acting on the object.

Typically these forces are negligible when viewed from a macroscopic perspective. At the micro-/nano-scale, however, these optical forces can be significant. The first demonstratable use of these forces came in the 1970s when Arthur Ashkin first developed the concept of optical tweezers.(*31*, *32*) Using this technique, a tightly focused laser beam can confine and/or manipulate micro/nanoscopic particles. The experimental realization of this phenomenon will be explored in more detail in sections 4.3 and 4.4. Here, we will content ourselves with a brief overview of the underlying physics behind optical forces.

There are two main *types* of optical forces: the radiation pressure force and the gradient force.(*33*) The radiation pressure force simply acts to push particles in the direction of the incident light, similar as outlined above in the discussion of reflection/absorption from a perfect mirror/absorber.[22] On the other hand, the gradient force tends to pull particles into regions of higher light intensity – and is thus the basis for optical tweezers. Once again, the analysis is generally broken down into the three regimes which were discussed in section 2.1.2. Continuing

[22] Strictly speaking the radiation pressure force can be more complex than this if the scattered light is not isotropic. For Rayleigh particles the scattering is seen as isotropic and thus this complexity is often neglected. See notes 23 and 24 for further details.

with the thread introduced in that section, we will restrict ourselves to dealing with the situation where $\lambda \gg a$.

The radiation pressure force is easy to imagine. Here the total power not transmitted by the particle must induce the particle to move in the direction of the incident light. The total light not transmitted through the object can be obtained from the scattering and absorption cross-sections, and thus by combining equations 2-23 and 2-26, we get[23]

$$\dot{Q}_{\text{extinct}} = (\sigma_{\text{abs}} + \sigma_{\text{scatt}})I_0 \,. \tag{2-30}$$

The force which results from this extinction of transmitted light is given by(*34*, *35*)

$$F_{\text{radiation}} = \frac{n_{\text{m}}}{c_0}\dot{Q}_{\text{extinct}} \,, \tag{2-31}$$

with $\vec{F}_{\text{radiation}} \parallel \vec{k}$, i.e. directed parallel to the incident light.[24]

To understand the gradient force, we must investigate how a dipole interacts with an external electric field intensity distribution. This force, which pulls a particle into regions of higher electric field intensity, is ultimately the result of the Lorentz force,(*36*, *37*)

$$\vec{F}_{\text{Lorentz}} = (\vec{p} \cdot \nabla)\vec{E} + \frac{d\vec{p}}{dt} \times \vec{B} \,, \tag{2-32}$$

where $\vec{p}$ is the particle dipole moment, as defined in equation 2-17 and $\vec{B}$ is the magnetic field. Expressing this in terms of the polarizability of the particle yields

$$\vec{F}_{\text{Lorentz}} = \varepsilon_0 \varepsilon_{\text{m}} \alpha \left((\vec{E} \cdot \nabla)\vec{E} + \frac{\partial \vec{E}}{\partial t} \times \vec{B} \right). \tag{2-33}$$

Now, using the vector identity $\nabla(\vec{A}_1 \cdot \vec{A}_2) = \vec{A}_1 \times (\nabla \times \vec{A}_2) + \vec{A}_2 \times (\nabla \times \vec{A}_1) + (\vec{A}_1 \cdot \nabla)\vec{A}_2 + (\vec{A}_2 \cdot \nabla)\vec{A}_1$ with $\vec{A}_1 = \vec{A}_2 = \vec{E}$ gives

$$\frac{1}{2}\nabla|E|^2 = \vec{E} \times (\nabla \times \vec{E}) + (\vec{E} \cdot \nabla)\vec{E} \,. \tag{2-34}$$

[23] In principle equation 2-31 should include a coefficient in front of σ_{scatt} to account for the fact that "forward" and "backward" scattered light may have different magnitudes.

[24] This assumes that the scattering is symmetric about the axis of incidence as well as a plane orthogonal to that axis. This approximation generally holds well for deeply subwavelength particles (i.e. the Rayleigh regime).

Combining 2-33 and 2-34 with Faraday's law ($\nabla \times \vec{E} = -\partial_t \vec{B}$) allows us to rewrite the Lorentz force as

$$\vec{F}_{\text{Lorentz}} = \frac{1}{2}\varepsilon_0 \varepsilon_{\text{m}} \alpha \nabla |E|^2 + \varepsilon_0 \varepsilon_{\text{m}} \alpha \frac{\partial}{\partial t}\left(\vec{E} \times \vec{B}\right). \qquad 2\text{-}35$$

Now, taking the temporal average over the electromagnetic field oscillation period

$$\vec{F}_{\text{gradient}} = \langle \vec{F}_{\text{Lorentz}} \rangle_T = \frac{1}{4}\varepsilon_0 \varepsilon_{\text{m}} \alpha \nabla |E|^2 + \varepsilon_0 \varepsilon_{\text{m}} \alpha \mu_0 \frac{\partial S}{\partial t}. \qquad 2\text{-}36$$

If we assume a time-constant electric field intensity distribution, the equation above, therefore, reduces to the well-known optical gradient force:[25]

$$\vec{F}_{\text{gradient}} = \frac{1}{4}\varepsilon_0 \varepsilon_{\text{m}} \alpha \nabla |E|^2 . \qquad 2\text{-}37$$

As shown by equation 2-37, for positive polarizability, the gradient force acts to pull particles along the electric field intensity gradient.

2.2 Heat Transfer

In sections 2.1.2 and 2.1.3, it was shown that under certain conditions, the absorption of light by a small metallic sphere could be significantly enhanced by plasmonic resonances. Most of the absorbed energy will be dissipated as heat. In other words, through a series of scattering events the energy absorbed by an electronic transition will be shared among the different degrees of freedom (e.g. vibrational modes) of the constituent elements that comprise the nanoparticle as well as the surrounding medium. The dissipation of this energy is referred to as heat transfer, and the increase in the average kinetic energy of each degree of freedom results in an increase in temperature.

The extent to which the temperature increases locally depends on how efficiently the heat can be dissipated to the surroundings. Generally, we are interested in the *rate* of heat transfer ($\dot{Q}$),[26] which by conservation of energy must be equal to the absorbed power (equation 2-26), i.e. $\dot{Q}_{\text{abs}} = \sum_i \dot{Q}_i$, where the subscript refers to the different forms of heat transfer. There are generally three main heat transfer mechanisms that need consideration: conduction, convection, and radiative – as illustrated in Figure 7. All three of these mechanisms will be introduced in

[25] This derivation for the gradient force assumes that the polarizability is real-valued. Strictly speaking this is inconsistent with the definition of the radiation pressure force (equation 2-30) containing an absorptive term. Additionally, it does not account for the effect of the scattered field (see note 14). Regardless, the derivation above is sufficient for understanding the qualitative nature of the optical gradient force.

[26] Q refers to the heat energy (joules) and $\dot{Q}$ refers to the time derivative, i.e. heat power (watts).

section 2.2.2, 2.2.3, and 2.2.4; however, conductive heat transfer is typically dominant in the plasmonic systems considered here, so it will receive the most emphasis.

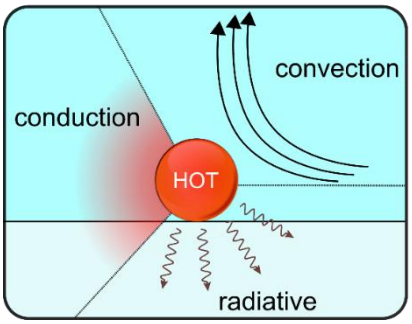

Figure 7 Overview of the primary heat transfer mechanisms discussed: conduction, convection, and radiative.

2.2.1 Thermal Properties of Materials

There are two key intrinsic quantities of a medium that determine the dissipation of heat: the thermal conductivity, κ, and the specific heat capacity, c_{P}. These parameters are primarily involved in solving for the heat transfer via conduction (section 2.2.2). Thermal conductivity describes the ability of a medium to conduct heat analogous to the concept of electrical conductivity for electrical currents. Formally, this quantity is defined as the proportionality constant between the local temperature gradient and heat flux ($J_{\dot{Q}}$), i.e. Fourier's law:

$$J_{\dot{Q}} = -\kappa \nabla T \,. \tag{2-38}$$

The second quantity, the specific heat capacity, is simply the energy that is required to increase the temperature of a medium, normalized by the mass, i.e.[27]

$$c_{\mathrm{P}} = \frac{1}{m} \cdot \frac{dQ}{dT} \,. \tag{2-39}$$

Using the thermal conductivity and specific heat capacity of a medium, we can define a third significant quantity, the thermal diffusivity

$$D_{\mathrm{th}} = \frac{\kappa}{\rho c_{\mathrm{P}}} \,, \tag{2-40}$$

where ρ is the density of the medium. The thermal diffusivity determines the speed at which heat can propagate through a material.

[27] Note, the subscript "*P*" on the specific heat capacity indicates that this value is determined at constant pressure which implicitly allows for the possibility that the material can expand due to a temperature increase.

The physical mechanisms which determine these quantities (κ, c_P, and D_{th}) vary between different materials. For instance, in conductive metals, the heat is transported primarily by electrons and thus typically have a much higher thermal conductivity than amorphous solids, such as glass, which conduct heat via phonons and have high scattering rates from grain boundaries. A summary of the broad range of thermal conductivities and diffusivities for different types of matter is shown in Figure 8.

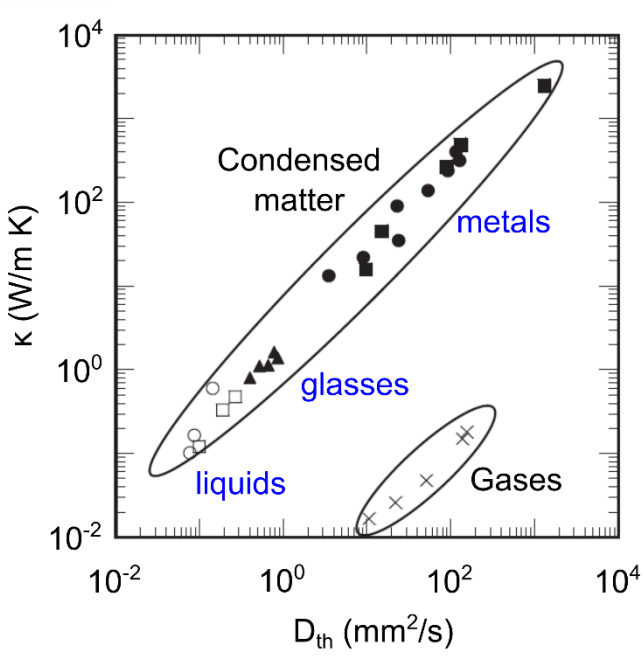

Figure 8 Thermal conductivity and diffusivity for different types of matter. Metals – filled circles, ceramics – filled squares, glasses – filled triangles, polymers – open squares, liquids – open circles, gasses – crosses. Adapted with permission from ref(38). © European Physical Society. Reproduced by permission of IOP Publishing. All rights reserved.

Temperature-dependent properties

In addition to the properties listed above, several other material parameters are temperature dependent, and therefore, the temperature can affect the behaviour of these materials. Of particular interest for this thesis are density and surface tension, which are briefly outlined below.

Density: Most materials tend to expand when heated. The increase in kinetic energy of the constituent atoms/molecules associated with a temperature increase causes a greater average separation distance. This effect corresponds to a volumetric expansion, i.e. a decrease in density. For most materials, the change in density with temperature is approximately linear over modest temperature changes. Linear changes in the density of a material with respect to changes in temperature are characterized by the thermal expansion coefficient β. Interestingly, however, for water, the relationship is highly non-linear near the freezing point, showing a maximum density at approximately 4°C.

Surface tension: Surface tension describes the effect that occurs at fluidic boundaries, such as a water-air interface. Essentially, water molecules are more strongly attracted to one another than to the air molecules, and as a result, the surface layer acts elastically to perturbations. Generally, the surface tension will decrease with increasing temperature since the increased kinetic energy causes a relative decrease in the strength of these attractive forces. For water in contact with air, the surface tension linearly decreases with increasing temperature over a broad temperature range.(*39*)

2.2.2 Conduction

Heat transfer by conduction can generally be envisioned as the transmission of thermal energy via collisions between neighbouring atoms/molecules. A schematic overview of this scenario being considered here (in the context of the model system introduced in section 1) is shown in Figure 9.

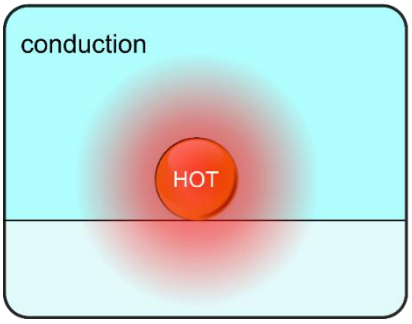

Figure 9 Heat transfer via conduction.

The general equation governing conductive heat transfer is known as the heat equation, given by[28]

$$\rho c_{\mathrm{P}} \frac{\partial T}{\partial t} - \kappa \nabla^2 T = \dot{q}\,, \qquad \text{2-41}$$

which must hold everywhere and is subject to appropriate boundary conditions. Note that $\dot{q}$ is the heat source density (units $\mathrm{W/m^3}$).

Steady-state

We will now analyze the thermal characteristics of the situation developed in section 2.1.2, i.e. the temperature profile induced by optical absorption in a spherical gold particle in a homogeneous water medium. Equation 2-41 is most easily solved under steady-state conditions where $\partial T/\partial t = 0$. Because of the radial symmetry of this problem, and the steady-state condition, equation 2-41 can be simplified to

[28] We are implicitly assuming here that the thermal properties are temperature independent and spatial homogeneous within each medium.

$$-\kappa \frac{1}{r^2}\frac{\partial}{\partial r}\left(r^2 \frac{\partial T}{\partial r}\right) = \dot{q}\,. \qquad 2\text{-}42$$

There are two different regions where this equation must be solved: I – within the nanoparticle ($r \leq a$), and II – in the surrounding medium ($r > a$). In regime I, we will assume that the heat source density is uniformly distributed. In regime II we assume that there is negligible absorption and thus $q_{\mathrm{II}} = 0$ everywhere.

For regime II, equation 2-42 can therefore be reduced to

$$\frac{\partial T_{\mathrm{II}}}{\partial r} = -C_0 r^{-2}\,. \qquad 2\text{-}43$$

And solving for the temperature profile, we get

$$T_{\mathrm{II}}(r) = -C_0 r^{-1} + C_1\,. \qquad 2\text{-}44$$

To solve for the coefficients, we apply the boundary conditions. We require that as $r \to \infty$ the temperature approaches the ambient temperature T_∞. For simplicity, we take $T_\infty = 0$ and are therefore solving for the temperature increase of the system due to optical heating. The constant offset in equation 2-44 is therefore $C_1 = T_\infty = 0$.[29]

To solve for the other integration coefficient, C_0, we apply the boundary condition at the interface between regions I and II. We know the total power absorbed by our particle from equation 2-26,[30] and due to the spherical symmetry of the problem, the heat flux everywhere in region II can be given by

$$J_{\dot{Q}} = \frac{\dot{Q}_{\mathrm{abs}}}{4\pi r^2}\,. \qquad 2\text{-}45$$

Thus, solving Fourier's law (equation 2-38) at the boundary between regions I and II ($r = a$) results in

$$\frac{\dot{Q}_{\mathrm{abs}}}{4\pi a^2} = -\kappa_{\mathrm{II}} \frac{\partial T_{\mathrm{II}}}{\partial r} = -\kappa_{\mathrm{II}} \cdot \frac{C_0}{a^2}\,, \qquad 2\text{-}46$$

where the temperature gradient from equation 2-43 is used. This results in

$$C_0 = -\frac{\dot{Q}_{\mathrm{abs}}}{4\pi\kappa_{\mathrm{II}}}\,, \qquad 2\text{-}47$$

[29] We can simply add the value of T_∞ to the temperature increase at any time if we wish to know the absolute temperature.
[30] Here we are implicitly assuming that conduction is the dominant heat transfer mechanism.

and finally, determining the temperature profile in region II as:

$$T_{\mathrm{II}}(r) = \frac{\dot{Q}_{\mathrm{abs}}}{4\pi\kappa_{\mathrm{II}}} \cdot r^{-1} \,. \qquad 2\text{-}48$$

Interestingly, the temperature profile in region II depends only on the thermal conductivity of region II, and the total heat dissipated within region I and is therefore independent of the material properties of our nanoparticle.[31]

To determine the temperature profile in our nanoparticle, we now solve equation 2-42 for $r \leq a$, i.e.

$$\frac{\partial T_{\mathrm{I}}}{\partial r} = -\frac{\dot{q}_{\mathrm{I}}}{3\kappa_{\mathrm{I}}} r + B_0 r^{-2} \qquad 2\text{-}49$$

and

$$T_{\mathrm{I}}(r) = -\frac{\dot{q}_{\mathrm{I}}}{6\kappa_{\mathrm{I}}} r^2 - B_0 r^{-1} + B_1 \,. \qquad 2\text{-}50$$

To have the temperature be finite at the origin implies that $B_0 = 0$. We also assume that the temperature is everywhere continuous, thus $T_{\mathrm{I}}(a^-) = T_{\mathrm{II}}(a^+)$.[32] Therefore, using the substitution $\dot{q}_{\mathrm{I}} = \dot{Q}_{\mathrm{abs}} \cdot \left(\frac{4}{3}\pi a^3\right)^{-1}$ the temperature profile in region I can be written as

$$T_{\mathrm{I}}(r) = \frac{\dot{Q}_{\mathrm{abs}}}{4\pi\kappa_{\mathrm{II}} a}\left[1 + \frac{\kappa_{\mathrm{II}}}{2\kappa_{\mathrm{I}}}\left(1 - \frac{r^2}{a^2}\right)\right]. \qquad 2\text{-}51$$

Since $\kappa_{\mathrm{I}} \gg \kappa_{\mathrm{II}}$, the terms in brackets above is approximately equal to one, implying that the temperature inside the nanoparticle is nearly constant, i.e.

$$T_{\mathrm{I}} \approx \frac{\dot{Q}_{\mathrm{abs}}}{4\pi\kappa_{\mathrm{II}} a}. \qquad 2\text{-}52$$

The exciting feature of equation 2-52 is that the temperature increase of our nanoparticle depends only on the thermal properties of the surrounding medium.[33] In general, this relation holds for thermoplasmonics: optical interactions are dictated by the properties of both the plasmonic particles and the surrounding medium; conversely, the thermal effects are dominated by the

[31] Provided that $\kappa_{\mathrm{II}} \ll \kappa_{\mathrm{I}}$ or that $q_{\mathrm{I}}(r)$ is spherically symmetric in region I.
[32] Continuity of temperature is not strictly required since effects like Kapitza resistances can cause a finite temperature discontinuity at the boundary between dissimilar mediums. This effect is addressed further in appended Paper i.
[33] Again we are assuming that $\kappa_{\mathrm{II}} \ll \kappa_{\mathrm{I}}$.

surroundings and tend to interact with and be influenced by, a much larger volume. As an additional note, although we are considering the case of a homogeneous environment, the same general behaviour holds for a particle at an interface with the substitution that κ_{II} becomes the average thermal conductivity of the two materials.[34](*40*) As a final note, if the temperature of the plasmonic particle is known (and assumed uniform), then the temperature outside the plasmonic structure (assuming a homogeneous environment) can be obtained by combining equations 2-48 and 2-52, i.e.

$$\Delta T(r) = \Delta T_{\mathrm{NP}} \cdot \frac{a}{r}. \qquad 2\text{-}53$$

Step-response

Here we investigate the transient evolution of the temperature profile in response to a heat source density that behaves as a step function, e.g. turning a heating laser "on" or "off." We restrict ourselves to analyzing the case of a point-like heat source representative of our model system for $r > a$. First, let us determine the response function of our system by taking the transient heat source to be a delta function. The heat equation (2-41) is, therefore,

$$\rho_{\mathrm{II}} c_{\mathrm{P,II}} \frac{\partial T_{\mathrm{II}}}{\partial t} - \kappa_{\mathrm{II}} \nabla^2 T_{\mathrm{II}} = Q_0' \delta(r)\delta(t)\,, \qquad 2\text{-}54$$

where Q_0' is the thermal energy of the delta pulse. The temperature response of this problem is given by(*41*, *42*)

$$T_{\mathrm{II}}(r,t) = \frac{Q_0'}{\rho_{\mathrm{II}} c_{\mathrm{P,II}}} \cdot \frac{\exp\left(-\frac{r^2}{4D_{\mathrm{th,II}}t}\right)}{\left(4\pi D_{\mathrm{th,II}}t\right)^{\frac{3}{2}}}. \qquad 2\text{-}55$$

Since a step-function can be represented as simply the integral over a delta-function, we can use equation 2-55 as a Green's function to determine the response of our system to a step-function,(*42*) i.e.

$$T_{\mathrm{II}}(r,t) = \frac{\dot{Q}_{\mathrm{abs}}}{\rho_{\mathrm{II}} c_{\mathrm{P,II}}} \int_0^t \frac{1}{\left(4\pi D_{\mathrm{th,II}}t'\right)^{3/2}} \cdot \exp\left(-\frac{r^2}{4D_{\mathrm{th,II}}t'}\right) dt'\,, \qquad 2\text{-}56$$

[34] Using the average thermal conductivity is only valid for larger distances away from the nanoparticle where the point-like approximation is valid. If one instead cares about the maximum temperature of the nanoparticle, the author has personally found that it is better to use the weighted average thermal conductivity where the substrate and superstrate contributions are weighted by the contact area.

where we assume our step function transitions from $\dot{Q} = 0 \rightarrow \dot{Q} = \dot{Q}_{\text{abs}}$ at $t = 0$. If we let $x = r\left(4D_{\text{th,II}}t'\right)^{-1/2}$ then $dx = -2D_{\text{th,II}}r\left(4D_{\text{th,II}}t'\right)^{-\frac{3}{2}}dt'$ and equation 2-56 can be rewritten as

$$T_{\text{II}}(r,t) = \frac{\dot{Q}_{\text{abs}}}{4\pi\kappa_{\text{II}}r}\left(1 - \text{erf}\left(\sqrt{\tau/t}\right)\right), \qquad 2\text{-}57$$

where $\text{erf}(a) = \frac{2}{\sqrt{\pi}}\int_0^a e^{-x^2}dx$ is the error function, and $\tau = r^2/4D_{\text{th,II}}$. Similarly, the response to an "off" transition is

$$T_{\text{II}}(r,t) = \frac{\dot{Q}_{\text{abs}}}{4\pi\kappa_{\text{II}}r}\text{erf}\left(\sqrt{\tau/t}\right) \qquad 2\text{-}58$$

for $\dot{Q} = \dot{Q}_{\text{abs}} \rightarrow \dot{Q} = 0$ at $t = 0$. Note that equations 2-57 and 2-58 are only valid for $t > 0$.

The key observation to be made here is that the temperature evolution is a function of *distance* from the heat source. Specifically, the time constant τ depends quadratically on the distance from the heat source. The thermal dynamics are significantly slower at large distances, as illustrated in Figure 10 below.

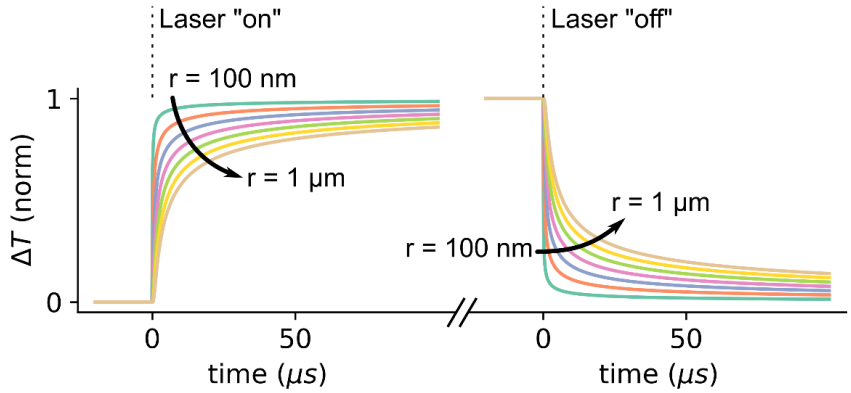

Figure 10 Temperature change at various distances to a step-function change in the heating laser power. Note that each curve has been normalized to the value at $t = \infty$ or $t = 0$ (for the "on" and "off" transitions, respectively) to highlight changes in the time dynamics.

Harmonic heating

If we restrict the time dynamics to the transient response of harmonic oscillation in $\dot{Q}_{\text{abs}}$ we can solve for the temperature profile of the system.[35] Equation 2-41 for this situation can be written as

[35] Note that we are no longer considering a "point-like" heat source as was done in for the step response, but now consider a finite size for the plasmonic nanoparticle.

$$\rho c_{\mathrm{P}} \frac{\partial T}{\partial t} - \kappa \nabla^2 T = \dot{q}_0 \left(1 + e^{-i\nu t}\right), \tag{2-59}$$

where ν is the heating modulation frequency, and we are concerned only with the real part of the solution. The equation above can be separated into the constant and harmonic components, where the solution to the constant part is of the form given in equations 2-48 and 2-52.

Focusing on the harmonic part, we once again separate the heat equation into regions I and II and, in both cases, assume a linear, and therefore harmonic response. For region II the heat equation becomes

$$-i\nu T_{\mathrm{II}} = D_{\mathrm{th,II}} \nabla^2 T_{\mathrm{II}}\,. \tag{2-60}$$

In region I, we approximate that the internal temperature is uniform and equal to the temperature at the boundary. Therefore it is sufficient to ensure the conservation of energy, i.e.

$$\left(\frac{4}{3}\pi a^3\right) \cdot \rho_{\mathrm{I}} c_{\mathrm{P,I}} (-i\nu T_{\mathrm{I}}) = (4\pi a^2) \cdot \kappa_{\mathrm{II}} \nabla T_{\mathrm{II}}(r = a) + \tilde{\dot{Q}}\,, \tag{2-61}$$

where $\dot{Q}_{\mathrm{abs}} = \dot{Q}_0 + \tilde{\dot{Q}} = \dot{Q}_0\left(1 + e^{-i\nu t}\right)$. The equation above simply states that the change in thermal energy within the particle is equal to the energy transmitted through the interface (see Fourier's law for flux, equation 2-38) plus the power absorbed. Note that $T_{\mathrm{I}} = T_{\mathrm{II}}(r = a)$.

In region II, we look for a solution of the form $T_{\mathrm{II}} = T_0 a r^{-1} e^{i(\Lambda \mathrm{r} - \nu \mathrm{t})}$, putting this ansatz into 2-60 allows us to solve for the functional form of Λ, i.e.

$$\Lambda^2 = \frac{i\nu}{D_{\mathrm{th,II}}}\,. \tag{2-62}$$

Putting our ansatz into the conservation of energy equation (2-61) to solve for T_0 and combining with the steady-state solution yields(*43*)

$$T_{\mathrm{I}}(t) = \frac{\dot{Q}_0}{4\pi\kappa_{\mathrm{II}} a} \cdot \left[1 + \frac{e^{-i\nu t}}{\left(1 - ia\Lambda - i\nu\rho_{\mathrm{I}} c_{\mathrm{P,I}} a^2/3\kappa_{\mathrm{II}}\right)}\right], \tag{2-63}$$

In region I. The solution in region II is

$$T_{\mathrm{II}}(r, t) = \frac{\dot{Q}_0}{4\pi\kappa_{\mathrm{II}} r} \cdot \left[1 + \frac{e^{i(\Lambda[r-a] - \nu t)}}{\left(1 - ia\Lambda - i\nu\rho_{\mathrm{I}} c_{\mathrm{P,I}} a^2/3\kappa_{\mathrm{II}}\right)}\right]. \tag{2-64}$$

The key observation is that the amplitude of temperature modulations decreases with increasing modulation frequency and distance from the origin. For high enough modulation frequencies, the heat cannot dissipate quickly enough to allow an appreciable change in temperature, and so only the steady-state solution remains (see Figure 11).[36]

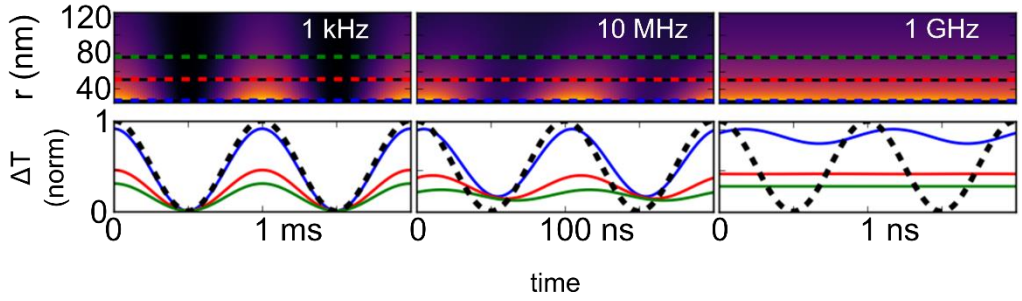

Figure 11 Harmonic heating of a gold nanosphere in water at different modulation frequencies (diameter = 50 nm). Top row: radial temperature maps vs time. Bottom row: Temperature modulation plotted at select distances (indicated by dashed lines in the top row). Dashed black lines on the bottom row show the heating modulation profile.

Collections of particles

Because of the linearity of the problem, when a collection of particles is optically heated, the resulting temperature field is simply the superposition of the contribution from each nanoparticle, i.e.

$$T_{\text{total}}(r,t) = \sum_i T_i(r,t)\,. \qquad \text{2-65}$$

This approximation is valid for both steady-state and transient heating as long as we can assume that the effective thermal properties of the medium are insensitive to the packing density.

Although this point may seem trivial, it has large implications. For instance, a collection of plasmonic spheres with interparticle spacing on the same order of magnitude as the particle size will tend to heat the surrounding in a manner comparable to that of a single large heat source. The volume of water that is effectively heated therefore scales with the diameter of the *collective* structure cubed instead of the individual nanoparticle size.(*44*) For modulated heating, the effects are also pronounced as the ability to effectively modulate the temperature in the surroundings diminishes rapidly as the number of plasmonic structures increases (see Figure 12).

[36] Consistent with our findings from the step response.

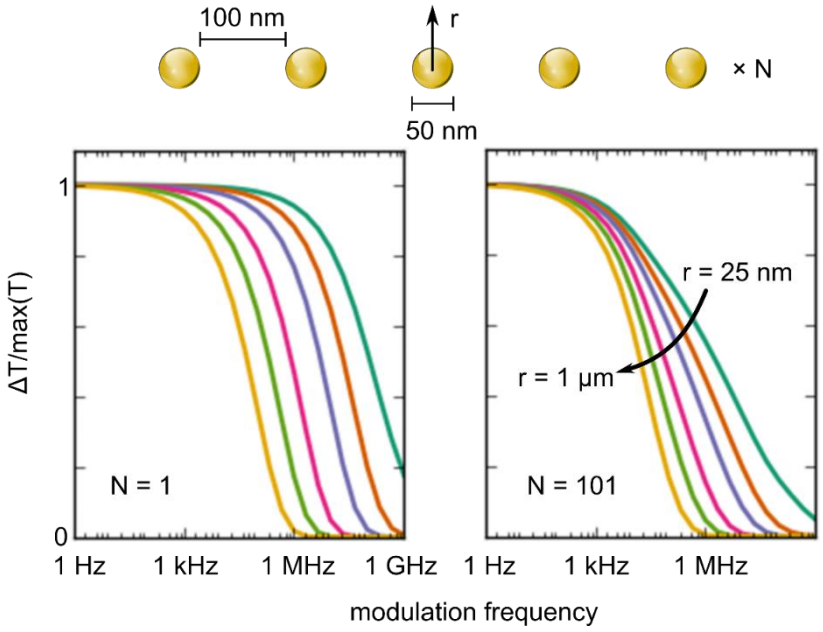

Figure 12 Collective heating effects on temperature modulation. A linear arrangement of 50 nm gold spheres in water are heated with a harmonic heat source density. Shown here is the relative modulation amplitude at varying distances from the central sphere (measurement vector is perpendicular to the axis of the spheres). For longer arrangements of particles, the temperature in the environment is modulated to a significantly lower extent due to collective heating effects.

2.2.3 Convection

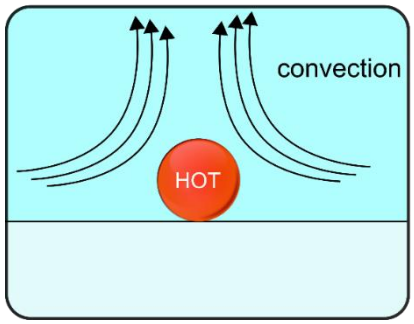

Figure 13 Heat transfer via convection.

Heat transfer via convection occurs when fluid flow causes heat transport, e.g. when you blow on your hand to cool it down after a burn. In this heat transfer mechanism, the mass transport resulting from fluid flow simply transports hot fluid molecules, thereby causing heat transfer. In general, there are two main types of convection: forced convection and natural convection. In forced convection, the fluid flow is externally imposed (such as by a fan or pump).

For natural convection, the fluid flow is generated by the heat source itself. The density of most fluids decreases with increasing temperature (see section 2.2.1); therefore, buoyant forces cause the heated fluid to rise and cooler fluids from the surroundings to flow into the heated region. If we consider a fluid that expands

linearly with coefficient β over some temperature change ΔT then the buoyant force density is[37](*45*, *46*)

$$\mathrm{f}_{\mathrm{buoyant}} = \rho_f \beta g \Delta T \,, \tag{2-66}$$

where g is the gravitational acceleration. This force term can then be inserted into the Navier-Stokes equation (see appendix) to determine the fluid flow resulting from a given temperature distribution.[38]

At macroscopic length scales, convection (either forced or natural) is often the dominant heat transfer mechanism for systems involving fluids. However, at the microscopic length scale (e.g. in thermoplasmonic systems), this is no longer the case. In order to estimate if conduction or convection is the dominant heat mechanism, it is useful to investigate the time scales associated with each process. If we consider a heated nanoparticle with radius $a = 100\,\mathrm{nm}$, surrounded by water, with $\Delta T_{\mathrm{NP}} = 50\,\mathrm{K}$, then the time scale for thermal conduction is roughly equal to[39]

$$\tau_{\mathrm{conduction}} \approx \frac{a^2}{D_{\mathrm{th}}} \approx 70\,\mathrm{ns}\,. \tag{2-67}$$

Meanwhile, the time scale for convection is on the order of[40]

$$\tau_{\mathrm{convection}} \approx \frac{\eta}{\rho_f \beta \Delta T g a} \approx 80\,\mathrm{s}\,, \tag{2-68}$$

where η is the viscosity of the fluid. The ratio of these two time-scales gives the Rayleigh number:

$$\mathrm{Ra\#} = \frac{\tau_{\mathrm{conduction}}}{\tau_{\mathrm{convection}}} = \frac{\rho_f \beta \Delta T g}{\eta D_{\mathrm{th}}} \cdot a^3 \approx 10^{-9}\,. \tag{2-69}$$

The Rayleigh number is often used as a rough estimate to determine if conduction or convection dominates heat transfer. If $\mathrm{Ra\#} \ll 1$, then conduction is dominant (since it is faster); conversely, if $\mathrm{Ra\#} \gg 1$, then convection is dominant. Notice that equation 2-69 scales with a^3 and so for larger heat sources,

[37] Here ρ_f is taken at ambient temperature.

[38] Note that this method would imply a pre-existing temperature distribution and would not properly account for the effect of convective heat transfer. However, as outlined below, conduction is typically dominant in thermoplasmonic systems and so this methodology is often sufficient for determining the relative effect of natural convection.

[39] Here $D_{\mathrm{th}} \approx 0.15 \times 10^{-6}\,\mathrm{m^2 s^{-1}}$ is the thermal diffusivity of water.

[40] Using values for water of: $\eta = 8.9 \times 10^{-4}\,\mathrm{Pa \cdot s}$, $\beta = 210 \times 10^{-6}\,\mathrm{K^{-1}}$, and $\rho_f = 1000\,\mathrm{kg/m^3}$.

the system the dominant heat transfer mechanism will quickly transition from conduction to convection.

2.2.4 Radiation

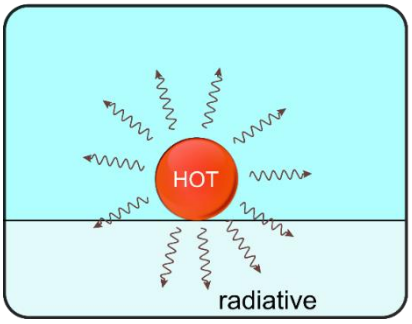

Figure 14 Heat transfer via radiation.

Radiative emission is the third fundamental heat transfer mechanism. For the thermoplasmonic situations discussed in this text, radiative heat transfer is generally inefficient, and it can be safely neglected. However, for the sake of completeness, a brief overview of the concept will be given here. Radiative heat transfer is the fundamental process where any matter at a temperature above 0 K will emit thermal radiation. The cause for this radiative emission is from the motion of charged particles within a material since whenever a charged particle changes its direction of motion, energy is emitted in the form of photons. The total power emitted via radiative heat transfer by a sphere is given by(*47*)

$$\dot{Q}_{\text{radiative}} = 4\pi\epsilon C_{\text{SB}} a^2 T^4 \,, \tag{2-70}$$

where ϵ is the emissivity of the particle[41] and C_{SB} is the Stefan-Boltzmann constant. However, since all matter emits thermal radiation, the surroundings will also transfer energy to the sphere. Thus the net radiative heat transfer is

$$\dot{Q}_{\text{radiative,net}} = 4\pi C_{\text{SB}} a^2 (T^4 - T_0^4) \,, \tag{2-71}$$

where T_0 is the temperature of the surroundings. Note that for simplicity, we have made the approximation $\epsilon = 1$. Since the water in contact with the gold nanosphere is approximately the same temperature as the nanosphere itself, the radiative heat transfer is approximately zero. In reality, the above approximation does not accurately account for all of the details of radiative heat transfer; however, generally, if a heat source is in physical contact with a medium that has a non-negligible thermal conductivity (such as water), then radiative heat transfer is inconsequential when compared to conductive heat transfer.

[41] A wavelength dependent measure of how efficiently a material can emit/absorb light.

2.3 Thermally Induced Bubbles

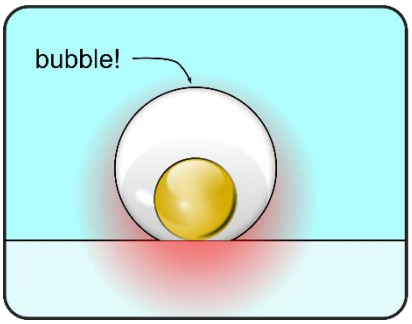

Figure 15 Overview of thermoplasmonic bubbles.

When thermoplasmonic effects increase the local temperature sufficiently, it is possible to induce phase transitions in the surrounding medium. In applications relevant to the discussion here, the ambient temperature and pressure are approximately $20°C$ and $1\,atm$, respectively. In this temperature/pressure regime, the most relevant phase transition that occurs is the transition of water from its liquid state to a gaseous state (see Figure 16). In the following section, the physical processes that occur during bubble formation & dissipation are discussed, as well as the associated effects on conductive heat transfer.

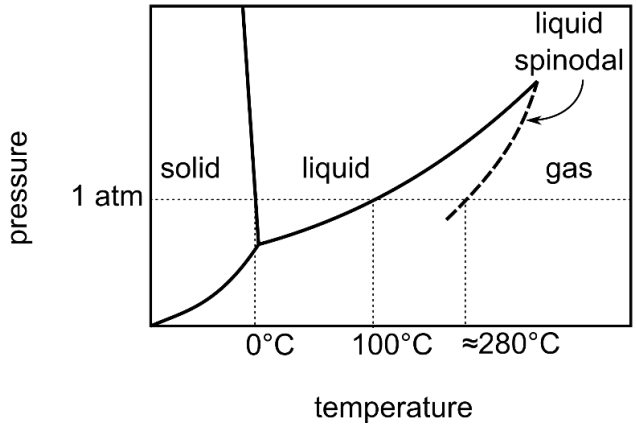

Figure 16 Phase diagram for water (not to scale). Dotted vertical lines indicate important temperatures at atmospheric pressure: freezing point, boiling point, and liquid spinodal temperature (left to right). Spinodal temperature estimate from ref(48).

Studies involving bubble generation instigated by optically heated plasmonic particles generally fall into one of two domains: either through pulsed illumination or via persistent heating with continuous-wave illumination. The physics involved in these two regimes are very distinct from one another, both in terms of the nucleation mechanism and the subsequent behaviour of the bubble. The following section will give an overview of the current understanding of the bubble formation around persistently heated gold nanoparticles.

2.3.1 Bubble “Life Cycle”

There are two broad stages to the “life cycle” of a thermoplasmonically induced bubble. The first stage occurs while the heating laser is applied (or “on”) and the subsequent stage where the heating laser is “off” – see Figure 17.

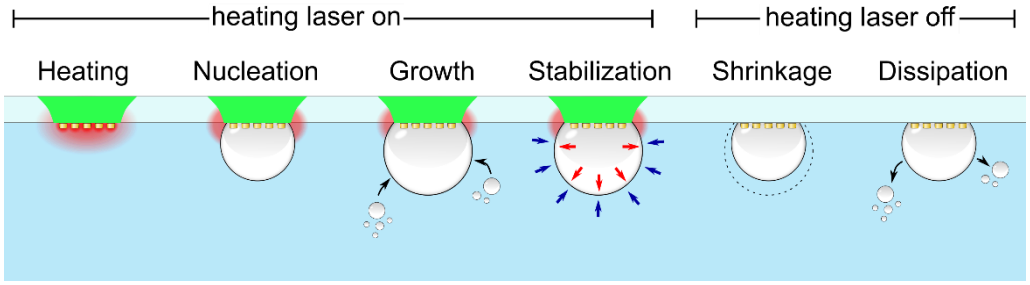

Figure 17 Schematic overview of the bubble life cycle.

During the first stage, immediately after the heating laser is switched “on,” the absorbed power is dissipated as heat leading to a local temperature increase (as discussed in section 2.2.2). Once the local temperature has increased sufficiently,[42] a spontaneous phase transition occurs, resulting in bubble formation. After the bubble has nucleated, it experiences a period of growth, and then depending on several factors, *can* achieve a stable steady-state size. Once the heating laser has been turned “off,” the bubble will proceed to shrink and dissipate. Below, each stage of the bubble life cycle is discussed in further detail.

Nucleation

When the liquid surrounding a thermoplasmonic nanostructure has been heated *sufficiently*, then a bubble is spontaneously nucleated. But what is meant by *sufficiently*? To discuss the necessary temperature increase required for bubble formation, it is worthwhile to briefly review the physics of intermolecular forces in fluids.

[42] “sufficiently” to be defined later.

Molecular interaction in fluids

Molecular interactions in fluids are characterized by attractive forces at large intermolecular separation distances and repulsive forces at short intermolecular distances. The attractive and repulsive effects can be incorporated into the standard ideal gas law (below) to qualitatively describe a real fluid and the associated liquid/gas phase transition. The ideal gas law can be written as

$$Pv = k_{\mathrm{B}}T\,, \tag{2-72}$$

where v is the molecular volume. The ideal gas law assumes that all particles are essentially non-interacting (apart from collisions) and therefore does not include *real* intermolecular effects necessary to describe phase transitions in fluids. In order to account for repulsive effects between molecules, each molecule can simply be assumed to occupy a region of space from which other molecules are excluded. To account for this exclusion zone, a constant, b, is subtracted from the molecular volume, i.e.

$$P(v - b) = k_{\mathrm{B}}T\,. \tag{2-73}$$

Additionally, the *real* pressure must be less than that of an ideal gas because of intermolecular attraction. The pressure correction term must also be dependent on the molecular volume in such a way that the molecular attraction grows at shorter intermolecular distances. By comparison with the Lennard-Jones potential,[43] the attractive component of the potential can be expected to scale according to $\propto v^{-2}$. The combination of an exclusion zone around each molecule (short distance repulsion) and molecular volume-dependent correction to the pressure (intermolecular attraction) results in the Van der Waals equation of state, i.e.(*42*)

$$\left(P + \frac{a^2}{v^2}\right)(v - b) = k_{\mathrm{B}}T\,, \tag{2-74}$$

where a and b are empirically determined constants, which respectively account for intermolecular attraction and repulsion. Using equation 2-74, the liquid/gas phase transition in many fluids can be qualitatively predicted/explained.

[43] The Lennard-Jones potential is often used to approximate intermolecular repulsion/attraction. This potential is given by $U(r) = A[(r_0/r)^{12} - (r_0/r)^6]$ where A describes the strength of the interaction and r_0 is the equilibrium displacement.

Figure 18 shows isotherms for a fluid obeying Van der Waals equation of state (equation 2-74). At a given pressure, up to three different regimes are possible depending on the temperature. At low temperatures (regime I), the corresponding isotherm only intersects the ambient pressure at one point, which corresponds to a small molecular volume, i.e. a stable liquid. Conversely, at very high temperatures (regime III), the only intersection occurs at large molecular volumes, corresponding to a stable gaseous state. At intermediate temperatures (regime II), the isotherm will intersect the ambient temperature at multiple points, indicating various fluid phases are possible and thus the potential for a metastable state.

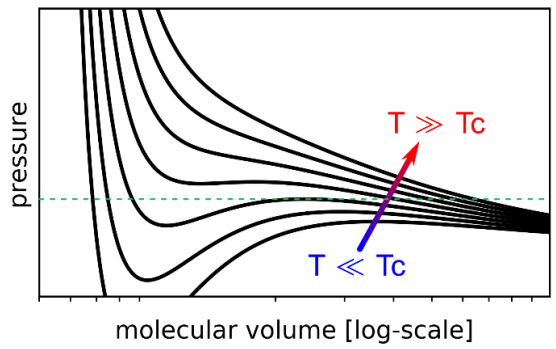

Figure 18 Isotherms for fluid obeying Van der Waals equation of state. A horizontal dashed line indicating constant ambient pressure is included to aid the discussion.

The lowest temperature of regime II corresponds to the normal boiling temperature, which for water at atmospheric pressure is around $100°C$. Importantly, it is still possible for water to remain in a liquid state for $T > 100°C$ since there is still an energy barrier preventing the phase transition from liquid to gas.[44] Meanwhile, at the highest temperature in regime II, the fluid can't remain in a liquid state – this is the liquid spinodal temperature (T_c) and corresponds to the spinodal line indicated in Figure 16.

In most thermoplasmonic systems, the local environment (e.g. a glass microscope slide) is particularly clean and smooth. It therefore does not contain pre-existing nucleation sites, and so the phase transition (bubble formation) occurs at local temperatures well above the boiling temperature.[45] As the temperature increases towards the spinodal temperature, the energy barrier preventing phase transition is reduced until thermal fluctuations (potentially facilitated by the presence of dissolved air molecules(*49*)) can overcome this barrier and cause the spontaneous nucleation of a bubble enveloping the heated plasmonic structure. Thus the heating *sufficient* for bubble nucleation occurs

[44] In most everyday circumstances however nucleation sites (such as pre-existing bubbles at small cavities in a kettle) act as a catalyst to overcome this energy barrier thus facilitating the phase transition to occur at $100°C$.
[45] See 44.

somewhere between the boiling temperature and the spinodal temperature.(*49*, *50*)

Once nucleated, the bubble is adhered to the glass substrate. In some instances, where larger bubbles are nucleated ($a_{\text{bubble}} > 10$ μm), transient oscillatory behaviour is observed immediately after nucleation.(*51*) Subsequently, there is a period of continued growth from further vapourization of the surrounding water.(*52*) The bubble has a nominally spherical shape. The contact angle at the intersection with the substrate is approximately the same as expected for macroscopic bubbles/liquid droplets, as determined by the hydrophobicity of the substrate.

Growth

After the bubble has been nucleated, the subsequent growth dynamics are highly dependent on the specific properties of the fluid.(*53*) For fluids such as water, where the solubility of dissolved air molecules decreases with increasing temperature, a second growth stage in the bubble life cycle occurs.(*52*) During this stage, water that was previously "air equilibrated" will become oversaturated with gas locally near the bubble. This causes a flux of air molecules into the newly formed bubble causing further bubble growth. In addition to increasing the size of the bubble, this growth stage also changes the internal composition. During this growth stage, the internal content of the bubble is increasingly composed of previously dissolved air molecules such as nitrogen and oxygen. In contrast, a newly formed bubble is predominantly composed of vaporized water molecules. Notably, in systems where the surrounding fluid has been previously removed of all gaseous content (i.e. degassed water), this growth stage is absent.(*52*, *54–56*)

Stabilization

Bubble growth "stabilization" (i.e. reaching a steady-state size under continued illumination) is not ubiquitous to all bubbles. Indeed in some cases, gaseous growth continues nearly unrestrained.[46] A bubble in a homogeneous environment has an inward acting surface pressure equal to

$$P_{\text{bubble}}^{\text{in}} = P_{\infty} + \frac{2\ell_{\text{interface}}}{a_{\text{bubble}}}, \qquad \text{2-75}$$

where P_{∞} is the ambient pressure (typically 1 atm) and $\ell_{\text{interface}}$ is the interfacial surface tension at the gas/liquid interface ($\approx 72 \times 10^{-3}$ N/m for air/water). The second term is known as the "Laplace pressure." We then find that the Laplace pressure is equal to the ambient pressure for a bubble radius of $a_{\text{bubble}} = a_{\text{bubble}}^{*} \approx 1.5$ μm. Thus, for $a_{\text{bubble}} \gg a_{\text{bubble}}^{*}$ the Laplace pressure is

[46] Unless prohibited by other factors such as a geometrically confined environment.

negligible, while for $a_{\text{bubble}} < a^*_{\text{bubble}}$ the Laplace pressure becomes dominant. Henceforth, "small" bubbles will refer to the case where $a_{\text{bubble}} < a^*_{\text{bubble}}$.

For the generation of small bubbles that stabilize, isolated plasmonic heating structures are a suitable heat source. This type of heating structure causes the resulting temperature increase to be highly localized. Thus, as the bubble grows, further growth via inward gas flux becomes chemically unfavourable since the temperature increase in the surrounding water quickly decreases the bubble grows. Additionally, the internal pressure which acts outward to oppose the inward acting surface pressure can be approximated from the ideal gas law,

$$P^{\text{out}}_{\text{bubble}} \propto a^{-3}_{\text{bubble}} . \qquad 2\text{-}76$$

Therefore for small bubbles, the ratio of outward *vs*. inward pressure scales with a^{-2}_{bubble}.[47] For this reason, further growth quickly becomes mechanically restricted by the inward acting pressure, and therefore the bubble becomes stable in size. These two factors (highly localized heating and significant Laplace pressure) cause small bubbles to remain small and quickly reach a steady-state size.

The case for *large* bubbles, however, is a bit more complicated. Here the inward acting pressure is simply P_∞ while the outward pressure is predominantly determined by the number of gas molecules that have been transferred into the bubble. Generally, large bubbles are nucleated around distributed heating structures,[48] resulting in a large region of heated water. Therefore, there is always a region near the gas/liquid/solid contact line where the local water temperature is significantly heated. As a result, continuous gas influx occurs, which leads to nearly unrestrained growth. Presumably, gaseous dissipation occurs at the "far" side of the bubble; however, this is a slow process (as discussed below) and therefore is not a significant factor in restricting bubble growth.[49]

Shrinkage & dissipation

Once the heating laser has been turned off, there is a fast initial shrinkage due to condensation of the vaporized water and a decrease in outward acting pressure.(*57*) Subsequently, the bubble dissipates the internal gas content back into the surrounding fluid.(*50*) As the gas is expelled into the water, the water at the bubble surface becomes oversaturated with gas. Therefore, the gas molecules in the water near the bubble interface must diffuse into the surroundings before

[47] Note that here we are neglecting changes in the bubble temperature which would occur with bubble growth. These effects, although likely not negligible, are difficult to accurately quantify. However, inclusion of these effects would cause the outward pressure to decrease *faster* with increasing bubble size and therefore the conclusions made here still stand.

[48] E.g. semi-continuous gold films or densely packed 2D nanoparticle arrays.

[49] Bubble growth in this stage can reach bubble diameters on the order of 100 μm without any appreciable change in growth dynamics. See ref(*52*).

further gas expulsion can occur.(*58*) For a gas bubble in a homogeneous liquid environment, the dissipation time (Δt_{off}) corresponding to a given initial bubble radius ($a_{\mathrm{bubble,init}}$) is given by(*59*)

$$\Delta t_{\mathrm{off}} = \frac{a_{\mathrm{bubble,init}}^2 K}{3 N_{\mathrm{A}} k_{\mathrm{B}} T D_f \chi}(1+\chi) \tag{2-77}$$

with

$$\chi = \frac{2\gamma_{\mathrm{interface}}}{a_{\mathrm{bubble,init}} P_\infty}, \tag{2-78}$$

where N_{A} is Avagadro's constant, K is Henry's constant for the gas/liquid combination, and D_f is the liquid diffusion coefficient. Note that χ is simply the ratio of the Laplace pressure to the ambient pressure. There are two limiting regimes for equation 2-77:[50] large bubbles ($\chi \ll 1$)

$$\Delta t_{\mathrm{off}} \approx \frac{P_\infty K}{6 N_{\mathrm{A}} k_{\mathrm{B}} T D \gamma_{\mathrm{interface}}} a_{\mathrm{bubble,init}}^3 \tag{2-79}$$

and *very* small bubbles ($\chi \gg 1$)

$$\Delta t_{\mathrm{off}} \approx \frac{K}{3 N_{\mathrm{A}} k_B T D} a_{\mathrm{bubble,init}}^2 . \tag{2-80}$$

The cubic dependence on the initial bubble size in equation 2-79 implies that the dissipation process can be incredibly slow for large bubbles, often requiring hundreds to thousands of seconds for full dissipation.(*50*, *55*, *57*) Conversely, by using isolated thermoplasmonic heat sources, small bubbles can be formed, with dissipation times on the order of $\mu s - ms$ depending on the plasmonic structure size.(*44*)

2.3.2 Bubble Effect on Heat Transfer

Because the thermal conductivity of gasses tends to be significantly lower than that of liquids or solids (see Figure 8), the formation of a bubble around a thermoplasmonic structure can substantially increase the temperature of the nanostructure. This is particularly impactful for bubble formation around nanoparticles in a homogeneous environment since the bubble will fully envelop the nanostructure and, therefore, drastically increase the nanoparticle temperature. When investigating bubble formation around nanoparticles on a substrate, the nanoparticle/substrate contact area becomes important in

[50] For intermediately sized bubbles ($a_{\mathrm{bubble}} \approx a_{\mathrm{bubble}}^*$) the nonlinear equation 2-77 must be solved numerically to obtain the dissipation time.

determining the overall temperature increase.[51] The ability of the substrate to dissipate heat efficiently can have important implications for the structural integrity of plasmonic nanostructures during bubble formation (see appended Paper ii for further details).

[51] See note 34.

3 Theory – Thermally Enhanced Mass Transport

In the following chapter, three different thermally induced mass transport mechanisms will be discussed: Brownian motion, thermophoresis, and flow induced transport. Regarding flow-induced transport, this is not exclusively a thermally induced phenomenon (e.g. it can be driven by external pressure differentials); however, this section will introduce the topic generally and then detail how flow can be generated via thermal effects.

3.1 Brownian Motion

It is well known that a small particle within a fluid will move with a seemingly random trajectory. This motion is typically referred to as "Brownian Motion" in reference to Robert Brown, who observed the effect by monitoring the motion of minute particles released by pollen grains in water.(*60*) Brown observed that these small molecules exhibited "vivid motion," which, he concluded, was not the result of currents or evaporation of the host fluid. Further experiments by Brown would show that the phenomenon also occurred with dead and inorganic particles.

From Einstein's seminal work,(*61*, *62*) we now know that Brownian motion results from random kinetic impulses from adjacent fluid molecules. To obtain a model for the effect of Brownian motion, we can start by writing the generalized Langevin equation and include a thermal force to account for these random kinetic impulses, i.e.

$$m\ddot{x}(t) + \gamma\dot{x} + Kx = F_{\text{thermal}} + F_{\text{ex}}\,, \tag{3-1}$$

where m is the mass of the particle, γ describes dissipative effects (i.e. friction), and K describes a Hookean restoring force (i.e. for a particle in a harmonic potential well). The term on the righthand side of the equation F_{thermal} and F_{ex} describe the thermal forces and any externally imposed forces, respectively. For now, we will consider "free" Brownian motion ($K = 0$) with no external forces ($F_{\text{ex}} = 0$) and assume that the friction coefficient is constant giving

$$m\ddot{x} + \gamma_0\dot{x} = F_{\text{thermal}}\,. \tag{3-2}$$

The stochastic motion of the particle is driven by the term $F_{\text{thermal}} = \varrho\xi(t)$ where ϱ determines the "amplitude" of the Brownian motion, and $\xi(t)$ is a Gaussian random variable which accounts for the fact that for our intents and purposes, the thermal forces are stochastic in nature. The stochastic term, $\xi(t)$, has zero mean and uncorrelated values ($\langle\xi(t)\xi(t')\rangle = \delta(t - t')$, where δ is the

Dirac delta function).[52] This stochastic force (hereafter referred to as the thermal force) encapsulates the aggregate effect of the host medium on the particle in question.

To put a bit more physical meaning into equation 3-2, let's assume that the particle of interest is a rigid sphere in some viscous medium. Thus we can use the Stokes drag coefficient, i.e. $\gamma = \gamma_0 = 6\pi\eta a$ (see appendix, equation 7-36) where η is the viscosity of the medium and a is the radius of our sphere. We then consider the "ensemble" or "average" trajectory of our particle. By considering averages, we can remove the stochastic term $\xi(t)$ so that we are left with only physical constants. To start, we multiply both sides of equation 3-2 by x and take the ensemble average, i.e.

$$m\langle x\ddot{x}\rangle + \gamma_0\langle x\dot{x}\rangle = \langle xF_{\text{thermal}}\rangle, \tag{3-3}$$

where $\langle A\rangle$ denotes the ensemble average of A. Because the thermal force is uncorrelated with position and has a mean of zero, the term on the righthand side must also be zero. Now, we note that $\frac{d}{dt}\langle x\dot{x}\rangle = \langle x\ddot{x}\rangle + \langle\dot{x}^2\rangle$ and rewrite the above equation as

$$m\left(\frac{d}{dt}\langle x\dot{x}\rangle - \langle\dot{x}^2\rangle\right) + \gamma_0\langle x\dot{x}\rangle = 0\,. \tag{3-4}$$

The equipartition theorem tells us that at thermal equilibrium (which we are implicitly assuming here), the thermal energy is shared equally among all degrees of freedom, so for a spherical particle moving in one dimension, the average kinetic energy is $\frac{1}{2}m\langle\dot{x}^2\rangle = \frac{1}{2}k_{\mathrm{B}}T$, where k_{B} is Boltzmann's constant, and T is the absolute temperature. Substituting the kinetic energy into equation 3-4 results in

$$m\frac{d}{dt}\langle x\dot{x}\rangle = k_BT - \gamma_0\langle x\dot{x}\rangle\,. \tag{3-5}$$

Now, let $A = \langle x\dot{x}\rangle$ for simplicity and divide out the mass:

$$\frac{d}{dt}A = \frac{k_{\mathrm{B}}T}{m} - \frac{\gamma_0}{m}A\,. \tag{3-6}$$

Here we take the ansatz $A = A_0e^{-\gamma_0 t/m} + A_1$ where A_0 and A_1 are constants. Inserting our ansatz into equation 3-6 yields $A_1 = k_BT/\gamma_0$. Noting that the first term in equation 3-6 decays exponentially we take the limit as $t \to \infty$ to get

[52] $\xi(t)$ also has the restriction that upon integration of the variance over some interval results in $\int_0^t\langle\xi^2(t)\rangle\,\mathrm{d}t = t$.

$$\lim_{t\to\infty} A = \lim_{t\to\infty}\langle x\dot{x}\rangle = \frac{k_B T}{\gamma_0}\,. \tag{3-7}$$

Now, given $\frac{d}{dt}\langle x^2\rangle = 2\langle x\dot{x}\rangle$ and solving for $\langle x^2\rangle|_{t\to\infty}$ gives

$$\langle x^2\rangle = \frac{2k_B T}{\gamma_0}t = 2Dt\,. \tag{3-8}$$

The term $\langle x^2\rangle$ is known as the Mean Squared Displacement (MSD) and is useful in characterizing the diffusion of Brownian particles. As shown above, the mean squared displacement grows linearly in time with a proportionality constant, D, known as the diffusivity, which depends on both the thermal energy of the medium and the drag coefficient.[53]

Now, returning to the Langevin equation for a free Brownian particle (equation 3-2) and taking the long-time limit so that we can discard the inertial term, we have

$$\dot{x} = \frac{\varrho}{\gamma_0}\xi \rightarrow x = \frac{\varrho}{\gamma_0}\int_0^t \xi(t')dt'\,, \tag{3-9}$$

where we have set the origin such that $x(t=0)=0$. Squaring both sides of equation 3-9 and taking the ensemble average yields[54]

$$\langle x^2\rangle = \frac{\varrho^2}{\gamma_0^2}\int_0^t \langle\xi^2\rangle dt\,. \tag{3-10}$$

By definition $\langle\xi^2\rangle = 1$, therefore

$$\langle x^2\rangle = \frac{\varrho^2}{\gamma_0^2}t + C_0\,, \tag{3-11}$$

where C_0 is some arbitrary constant that must equal zero by our definition of the origin. Equating equation 3-11 and 3-8, we can now solve for the "amplitude" of our thermal (stochastic) force, ϱ, as:

$$\varrho = \sqrt{2k_B T\gamma_0}\,. \tag{3-12}$$

[53] Note that if the particle were diffusing in 3-dimensions then we would have MSD = 6Dt

[54] Note that for Itô stochastic integrals the transition from equation 3-9 to 3-10 is permitted according to Itô isometry.

The above result, known as the fluctuation-dissipation theorem, shows how the stochastic process that induces Brownian motion is inextricably linked to the dissipative forces that inhibit directional motion, i.e. the drag force.

It can also be useful to consider the distribution of frequencies in the trajectory of our Brownian particle. To see this, we can take the Fourier transform of our Langevin equation, once again ignoring inertial contributions, i.e.

$$-i\omega\gamma_0\tilde{x} + K\tilde{x} = \sqrt{2k_BT\gamma_0}\tilde{\xi}\,, \tag{3-13}$$

where $\tilde{x}$ is the Fourier transform of x. With a view to later applications, we have left in the spring constant K to include the possibility that the particle is contained by a harmonic potential. After solving for $\tilde{x}$, we can obtain the power spectral density in the long-time limit as $\mathrm{PSD} = \lim_{t\to\infty}\langle|\tilde{x}|^2/t\rangle$, i.e.

$$\mathrm{PSD} = \frac{2k_\mathrm{B}T\gamma_0}{K^2 + \omega^2\gamma_0^2}\,. \tag{3-14}$$

At this point, we can make a change of variables by defining a characteristic frequency associated with the potential as $f_c = K/2\pi\gamma_0$, thus

$$\mathrm{PSD} = \frac{D}{2\pi^2(f_c^2 + f^2)}\,. \tag{3-15}$$

Shown in Figure 19 are numerical simulations for Brownian motion in 1D under the inertial free approximation for both the case of a free particle and a particle in a harmonic potential. Over short time scales, the trajectories are similar in both situations (see Figure 19a inset); however, at longer time scales, the particle within a harmonic potential is confined while the free particle continues to diffuse unimpeded. This effect is highlighted in the MSD of an ensemble (see Figure 19b). Additionally, the particle in the harmonic potential shows large attenuation at frequencies below the "corner" frequency, f_c, as shown in Figure 19c.

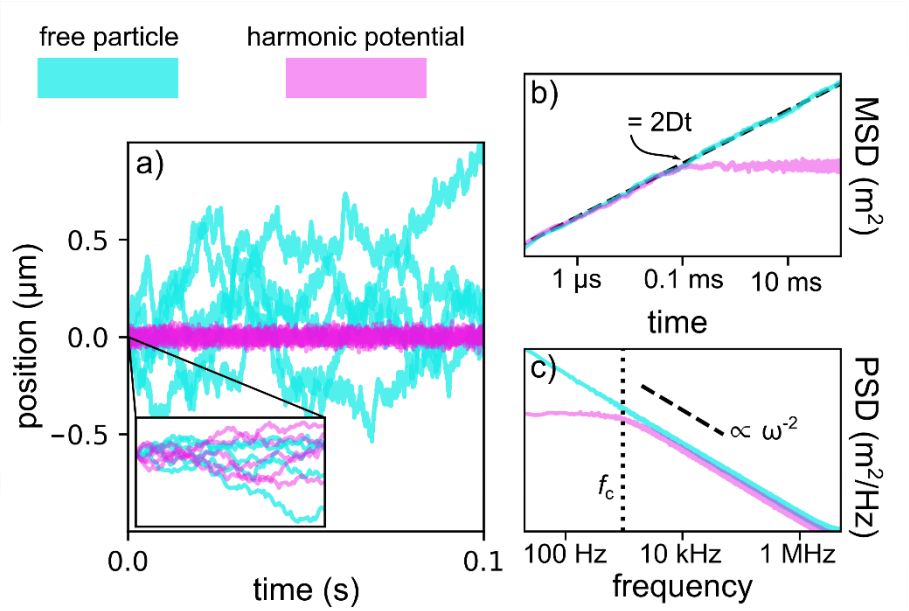

Figure 19 Simulated Brownian motion for a free particle (blue) and particle in a harmonic potential (pink). a) Simulated trajectories (N=5). a-inset) Zoom-in of the first 10 μs. b) Ensemble mean squared displacement (N=100). c) Ensemble averaged power spectral density (N=100). Data shown is for a massless rigid sphere ($a = 100$ nm) in water at $T = 300$ K. Harmonic potential has a spring constant $\kappa = 10\ pN/\mu m$. All particles initially at $x = 0$.

Hydrodynamic Brownian motion

Thus far, the discussion of Brownian motion has assumed the drag coefficient is constant, i.e. independent of the frequency of motion. At long time scales, this approximation is justified; however, hydrodynamic effects become significant at short time scales. For an incompressible fluid, such as water, no single fluid molecule can move without displacing other fluid molecules. Therefore, a time scale exists at which hydrodynamic effects will induce correlations between the velocity at time t and $t + \delta t$.(*63*) This concept is discussed further in the appendix (see sections 7.2 and 7.2.1 – "frequency-dependent" effects). To get a rough estimate for the time scale at which these effects become significant, we can consider the time scale over which fluid relaxation occurs on the length scale of our probe particle: $\tau_f = a^2\rho_f/\eta$, where ρ_f is the fluid density, and η is the viscosity. For the particle investigated in Figure 19, this would correspond to $\tau_f \approx 10$ ns, and even for $a = 1$ μm the time scale would still be as low as $\tau_f \approx 1$ μs. Therefore the "low frequency" model introduced above is generally valid for the time scales investigated in this thesis.

3.2 Thermophoresis

When a colloidal particle is placed within an external temperature gradient, there is a tendency for it to move parallel to the temperature gradient, a process known as thermophoresis.(*64*) This tendency towards directed motion is given by the simple equation

$$\vec{r}_{\text{drift}} = -D_T \nabla T \,, \tag{3-16}$$

where D_T is known as the thermal diffusion coefficient (or more correctly, the thermophoretic mobility). The magnitude of D_T has been experimentally observed to fall within the range of $10^{-8} - 10^{-7}\ \text{cm}^2\text{s}^{-1}\text{K}^{-1}$ in many cases, although the exact value is highly system-specific and can be positive or negative depending on the salinity of the solvent.(*65*) For colloidal suspensions with relatively low concentration,[55] the thermophoretically induced particle flux, $J_{\varsigma,\text{thermal}}$, will be opposed by a diffusive particle flux (due to Brownian motion), $J_{\varsigma,\text{diffusive}}$, which acts in opposition to the concentration gradient, i.e.

$$J_{\varsigma,\text{net}} = J_{\varsigma,\text{thermal}} + J_{\varsigma,\text{diffusive}} = -\varsigma D_T \nabla T - D \nabla \varsigma \,, \tag{3-17}$$

where ς is the local concentration of colloidal particles, and D is the diffusion coefficient from Brownian motion (see section 3.1). Under steady-state conditions, the net particle flux must be zero, and thus the local relative colloid concentration due to the presence of a temperature gradient is given by(*66*)

$$\frac{\varsigma}{\varsigma_0} = \exp\left(-\frac{D_T}{D}\nabla T\right). \tag{3-18}$$

The ratio between the thermophoretic mobility and the diffusion coefficient is often referred to as the Soret coefficient ($S_T = D_T/D$) and is the parameter that determines the extent of depletion or accumulation that occurs for particles due to thermophoretic effects. The thermophoretic mobility has generally been found to be insensitive to particle size, instead depending mainly on the specific interactions at the particle/solvent interface.(*67–69*) However, since the diffusion coefficient is inversely proportional to the particle radius (for spherical particles under the Stokes drag approximation – see the appendix), therefore the Soret coefficient is linearly dependent on the particle radius. Thus, smaller particles tend to be affected less by thermophoresis since they have a higher diffusivity due to Brownian motion. Additionally, it has been found that the

[55] So that interparticle interactions can be safely neglected.

Soret coefficient does show some temperature dependence,[56] being well approximated by the empirically obtained relation(*70*)

$$S_T(T) = S_T^{\infty}\left[1 - \exp\left(\frac{T^{\star} - T}{T_0}\right)\right], \qquad 3\text{-}19$$

where S_T^{∞} is the high-temperature limit, $T^{\star}$ is the critical temperature at which the behaviour changes from thermophilic to thermophobic, and T_0 determines how strongly the Soret coefficient depends on temperature.

Physical mechanisms of thermophoresis.

Part of the reason for the highly system-specific values for D_T stems from the multiple physical mechanisms which give rise to thermophoretic motion. Arguably the most fundamental mechanism for thermophoresis results from thermo-osmotic flows at the particle/solvent interface. This interfacial flow arises due to thermally induced inhomogeneities in the electric double layer surrounding the colloid.(*71*) The counterion cloud adjacent to the charged surface of the colloid follows a Poisson-Boltzmann concentration distribution which is temperature-dependent. Therefore, a thermal gradient induces a concentration gradient of counterions across the particle surface, which creates an osmotic pressure imbalance (see Figure 20a). This pressure imbalance causes the surrounding liquid to flow along the temperature gradient towards the hot side of the colloid. Because of this interfacial fluid flow, the colloid will move with the same velocity gradient but in the opposite direction, i.e. against the temperature gradient / towards cooler temperatures (Figure 20c).

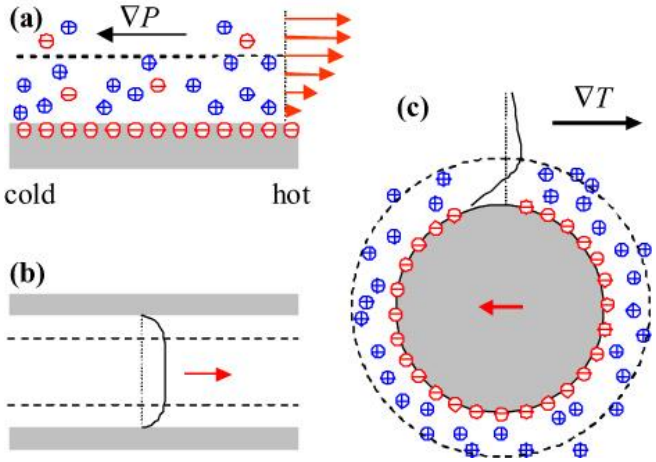

Figure 20 Thermo-osmotic flows due to a temperature gradient. a) Thermo-osmotic flow near a charged surface under a temperature gradient. b) Analogous case of thermo-osmotic flows in a microchannel. c) Thermo-osmotic flows around a charged colloidal sphere cause the particle to drift in the opposite direction as the temperature gradient. The solid black line shows the fluid velocity profile in the laboratory frame of reference. Reprinted with permission from(71). Copyright 2010 IOP Publishing. All rights reserved.

[56] Beyond what would be expected simply due to the dependence of the diffusion coefficient on temperature.

Another contribution to thermophoretic motion is due to the temperature-dependent density of most solvents. Typically, liquids will decrease in density at elevated temperatures. Van der Walls interactions are often dominant for colloidal particles in many liquids. As a result, the colloidal particle will be more strongly attracted to regions of higher liquid density, which typically occur at lower temperatures (see Figure 21). Due to the stronger attraction on the cold side, there tends to be a net solvent flow along the colloid/solvent interface towards higher temperature regions. It is interesting to note that the thermophoretic mobility of many colloidal particles in water changes sign (i.e. thermophobic to thermophilic) at around $5°C$, which is also the temperature where water density is at a maximum.(*72*) This tendency for particles to migrate towards regions of high solvent density further illustrates why, for many systems, colloidal particle motion is usually thermophobic.

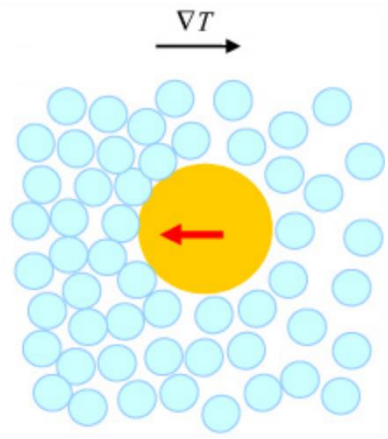

Figure 21 Density driven thermophoresis. A colloidal particle where the surrounding liquid has a temperature-dependent density with higher densities at lower temperatures. Dispersion forces attract the colloid towards the cold side (regions of higher density). Reprinted with permission from(71). Copyright 2010 IOP Publishing. All rights reserved.

From the thermophoresis mechanisms described above, it would appear that colloidal particles *always* exhibit thermophobic behaviour (i.e. $D_T > 0$). While thermophobic behaviour is often observed, controlling the properties of the solvent can have a drastic effect on the magnitude of thermophoretic mobility and even cause sign reversal ($D_T \rightarrow D_T < 0$), thus creating thermophilic behaviour. Putnam and Cahill have observed that for solutions with high salt concentrations, the thermophoretic mobility could be changed over an exceedingly large range ($D_T = -0.9 \times 10^{-7} \rightarrow +1.5 \times 10^{-7}\ \mathrm{cm^2 s^{-1} K^{-1}}$) by changing the type of dissolved ions.(*65*) This interesting result can be understood by considering the motion of the dissolved ions in response to a temperature gradient. In addition to the intrinsic thermophoretic motion of the colloid, dissolved ions will also respond in an analogous fashion. The thermophoretic motion of the dissolved ions (which can vary in magnitude and sign) results in ionic concentration gradients, thereby creating an electric potential. This thermophoretic response of the ionic solution thus induces electrophoretic motion of the colloidal particle under study.(*71*) Depending on the surface

properties of the colloid and the ionic concentration of the solvent (including the ionic species), thermophoretically induced electrophoresis of the colloid can dominate the overall thermophoretic motion and generate either a thermophilic or thermophobic response.

One field where the utilization of thermophoretic effects shows great promise is in quantifying biomolecular interactions.(*8*, *9*, *73*) The thermophoretic mobility for complex molecules (such as proteins) is highly sensitive to molecular properties such as the size, charge, hydration shell, and conformation. The extent of thermophoretic depletion, therefore, can change drastically upon molecular binding. This technique, known as microscale thermophoresis, has recently been introduced as a competitor to more established techniques such as surface plasmon resonance (SPR) sensing. Thermophoretic forces have also been demonstrated as a means by which a force can be imparted on a particle to induce or restrict motion. This technique is analogous to optical tweezers (see sections 4.3 and 4.4) but utilizes a temperature gradient instead of an optical electric field intensity gradient to impart forces. Some recent works have utilized the inherent thermophobic response of particles and dynamic temperature fields to induce trapping.(*74*, *75*) In contrast, other studies have engineered the system to produce a thermophilic response.(*76*, *77*) Additionally, one can also design particles to generate their own temperature gradient and thus create their own thermophoretic propulsion.(*78–83*)

3.3 Flow Induced Transport

Flow-induced transport is simply the transport of particles due to an externally imposed fluid flow. This type of mass transport is often discussed in the context of analytes that are suspended in a host fluid. Generally, these analytes will follow the fluid streamlines,[57] and therefore, the external flow can bring these analytes into a region of interest, e.g. into contact with sensors on the substrate of a microfluidic channel. At microscopic length scales, the process of flow induced transport directly competes with Brownian motion, and thus the former is only of consequence if it is substantially more impactful than the latter.

To compare these two processes, it is instructive to compare the time scale for transport for each process (similar to what was done while comparing convective heat transport to conductive heat transport in section 2.2.3). If we consider uniform fluid flow with speed u, and wish to transport the analytes over a distance L then the time scale for flow induced transport is[58]

[57] In principle there is no such thing as a "perfect" tracer particle that faithfully follows the fluid streamlines, but for many micro/nanoparticles with a density similar to that of the host fluid this approximation is generally valid.

[58] Equation 3-20 implicitly assumes that the desired trajectory of the particle is parallel with flow velocity. If these two parameters are not parallel, then a better definition is $\tau_{\text{flow}} = L^2/(\vec{u} \cdot \vec{L})$.

$$\tau_{\text{flow}} \approx \frac{L}{u}. \tag{3-20}$$

Meanwhile, the time scale for diffusion over the same distance is

$$\tau_{\text{diffusion}} \approx \frac{L^2}{D}, \tag{3-21}$$

where D is the diffusivity of the analyte particle (see section 3.1). Once again, we can take the ratio of these two time scales to get a sense of which process is dominant. This dimensionless number is known as the Péclet number:

$$\text{Pe\#} = \frac{\tau_{\text{diffusion}}}{\tau_{\text{flow}}} = \frac{Lu}{D}. \tag{3-22}$$

Note that the diffusion coefficient is inversely proportional to the radius of the analyte, $D \propto a^{-1}$, and therefore the Péclet number scales according to $\text{Pe\#} \propto Lua$. Therefore, flow induced transport is most efficient for high flow speeds over long transport distances but tends to be less efficient for smaller analytes.

However, in most practical situations, the fluid flow is rarely uniform and not necessarily aligned with the desired transport vector. Now let us consider two infinite parallel planes (lying along the x-axis) separated by a distance h (along the y-axis) with a viscous fluid in between. Assume that a pressure gradient, $\partial_x P$, exists parallel to the symmetry axis of the channel, causing the fluid to flow. The steady-state solution, assuming an incompressible fluid and laminar flow, can be solved using the continuity equation as well as the Navier-Stokes equation (see appendix).

From the continuity equation for an incompressible fluid, we have

$$\frac{\partial u_x}{\partial x} + \frac{\partial u_y}{\partial y} = 0. \tag{3-23}$$

Because of the translational invariance along the x-axis, $\partial_x u_x = 0$ and therefore $\partial_y u_y = 0$. This reduces the Navier-Stokes equation along the x-axis to

$$\frac{\partial P}{\partial x} = \eta \frac{\partial^2 u_x}{\partial y^2}, \tag{3-24}$$

yielding the solution

$$u_x(y) = \frac{\partial P}{\partial x}\frac{1}{2\eta} y^2 + C_0 y + C_1. \tag{3-25}$$

Assuming the no-slip condition at the planar interfaces gives the boundary conditions $u_x(h) = u_x(0) = 0$, which allows us to solve for the integration constants as $C_1 = 0$ and $C_0 = -\partial_x Ph/2\eta$ resulting in a parabolic flow profile, i.e.

$$u_x(y) = \frac{\partial P}{\partial x}(y^2 - yh). \qquad 3\text{-}26$$

From equation 3-26, we can see that the flow speed decreases towards either of the boundaries and has a maximum speed equidistant between the planes. In the context of the model system, which involves transporting an analyte to a sensor on the surface of one of the planes, this externally imposed flow will be least efficient near the sensor, as shown in Figure 22.

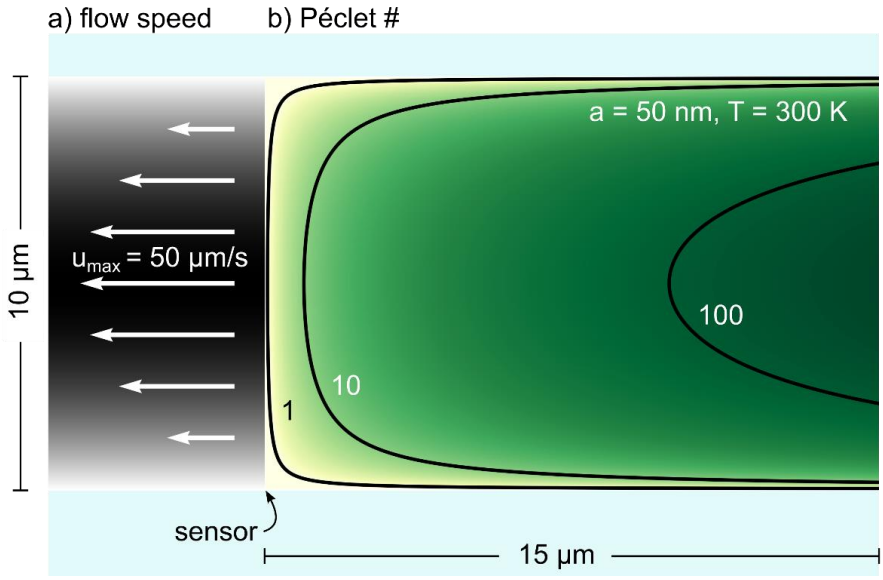

Figure 22 Flow-induced transport in water. a) laminar fluid velocity flow profile induced between two infinite parallel planes. b) Effective Péclet number (see note 58) for this flow profile to achieve analyte transport to a sensor at the indicated position. Numbers in b) indicate the effective Péclet number at the corresponding contour. The parameters for the test analyte diffusion coefficient are given in the top right.

In Figure 22a, we see the parabolic flow profile induced between two infinite parallel planes with a separation of 10 µm. Figure 22b shows that the effective Péclet number is shown across the microchannel cross-section, highlighting the regions where an externally imposed fluid flow is most/least effective. Note that the Péclet number has been modified to account for the difference between the flow direction and the displacement vector from the target sensor (see note 58). Clearly, this flow profile is very efficient in achieving mass transport at large displacements from the sensor. However, in the local vicinity of the sensor, diffusion (i.e. Brownian motion) is often dominant which can limit the overall detection rate.(*84*, *85*)

3.3.1 Thermocapillary Flow

One way of achieving flow near an interface is through the utilization of surface tension gradients. When a surface tension gradient exists at a liquid interface, it induces fluid flow, effectively creating a slip-velocity at the boundary. This phenomenon is known as the Marangoni effect. When the surface tension gradient is established by a temperature gradient, it is often referred to as thermocapillary flow (which happens to be particularly impactful in the context of thermal bubbles).

Consider a viscous fluid bounded by infinite planes at $y = 0$ and $y = h$. Along the interface at $y = 0$, suppose that a constant temperature gradient exists parallel to the x-axis and that this temperature gradient induces a constant surface tension gradient. The presence of a surface tension gradient causes the fluid to flow towards regions of higher surface tension since the fluid is more strongly bound there, resulting in an effective slip velocity at the interface: u_{slip}.

For illustrative purposes, we now consider two parallel planes with fluid in between and a constant thermocapillary induced slip velocity at the lower interface. Solving the incompressible, laminar, Navier-Stokes equation in the absence of other effects leads to

$$u_x(y) = C_0 y + C_1 \,. \tag{3-27}$$

With the boundary conditions: $u_x(0) = u_{\text{slip}}$ and $u_x(h) = 0$ this results in the following velocity field:

$$u_x(y) = u_{\text{slip}} \left(1 - \frac{y}{h}\right). \tag{3-28}$$

From equation 3-28, we can see that the fluid speed is fastest at the boundary because of the slip velocity induced by the thermocapillary effect.[59] This contrasts with the result obtained for externally driven flow (equation 3-26), where the flow speed becomes negligible at the boundary.

One area where these thermocapillary effects become particularly useful is in the context of thermally induced bubbles (see section 2.3). In this case, the thermally nucleated bubble has a pronounced temperature gradient along the surface, which causes a significant surface tension gradient, thereby inducing fluid flow. Generally, the resulting flow profile is difficult to predict analytically and often requires numerical calculation. However, if the fluid flow induced is significant enough such that appreciable speed occurs at a large distances from the bubble, then the symmetry of the problem allows one to approximate this effect as a

[59] Note that here there is no externally driven flow, so the fluid flow profile is driven only by the thermocapillary slip velocity at the interface.

force singularity oriented normal to the interface. This approximation is known as the "Stokeslet" approximation and will be discussed in the following section.

3.3.2 Stokeslet Approximation

The fundamental force singularity which describes translational motion for laminar flow in a viscous medium is called the *Stokeslet*. Using a Stokeslet to represent the driving force, one can describe the fluid flow in a homogeneous system. The response of a viscous fluid to a point force, $F_{\text{Stokeslet}}$, (for simplicity placed at the origin) can be obtained by solving the incompressible, laminar, Navier-Stokes equation. This results in the velocity field

$$u_{i,\text{Stokeslet}} = \frac{F_{j,\text{Stokeslet}}}{8\pi\eta}\left(\frac{\delta_{ij}}{r} + \frac{r_i r_j}{r^3}\right), \tag{3-29}$$

where the subscript i, j denotes the cartesian axis and $\vec{r} = (r_i, r_j)$ is the vector between the location of interest and the singularity.[60] The term δ_{ij} is the Kronecker delta function.

In the "model system" considered in this thesis (which is generally representative of many relevant *real* systems), there is also the influence of an infinite boundary to consider. The boundary conditions imposed by the substrate/interface requires that the fluid flow speed equals zero at the boundary (i.e. the no-slip condition). By incorporating higher-order force singularities to satisfy this boundary condition, the Stokeslet approximation can be extended to the physically relevant scenario of a force singularity near an infinite no-slip plane (e.g. which can be realized by a thermoplasmonically generated surface bubble and the resulting thermocapillary flows).

The image singularities needed to satisfy the no-slip boundary condition for a Stokeslet that is oriented normal to the interface and separated by a distance h from the interface are: Stokeslet, Stokes-doublet, and source-doublet located at $-h$.(*86*) This results in a velocity profile given by(*87*)

$$u_{i,\text{Stokeslet}}^{1-\text{plane}} = \frac{F_j}{8\pi\eta}\left[\left(\frac{\delta_{ij}}{r} + \frac{r_i r_j}{r^3}\right) - \left(\frac{\delta_{ij}}{R} + \frac{R_i R_j}{R^3}\right) - 2h\frac{\partial}{\partial R_j}\left\{\frac{hR_i}{R^3} - \left(\frac{\delta_{ij}}{R} + \frac{R_i R_j}{R^3}\right)\right\}\right], \tag{3-30}$$

where $\vec{r} = (x_i, x_j - h)$ is the vector to the Stokeslet singularity and $\vec{R} = (x_i, x_j + h)$ denotes the vector to the image singularities.

[60] Note that due to the symmetry of the problem only two spatial coordinates are needed for a single Stokeslet if the force vector is parallel to a coordinate axis.

The Stokeslet approximation can be extended even further to the case where there are two infinite no-slip planes parallel to one another (i.e. thermoplasmonically induced flow in a microchannel). Here one must use an infinite series of higher-order image singularities to satisfy the boundary conditions at both planes.(*88*)[61]

The key feature to the Stokeslet 1-plane and 2-plane velocity field solutions is that they provide significant flow close to the no-slip plane, which is highly suitable for providing efficient mass transport to a location (e.g. sensor) on the boundary of a microwell near the Stokeslet, as shown in Figure 23. Here we can see the flow profile for a Stokeslet near a single infinite no-slip plane (Figure 23a) or bounded by two infinite no-slip planes (Figure 23b).

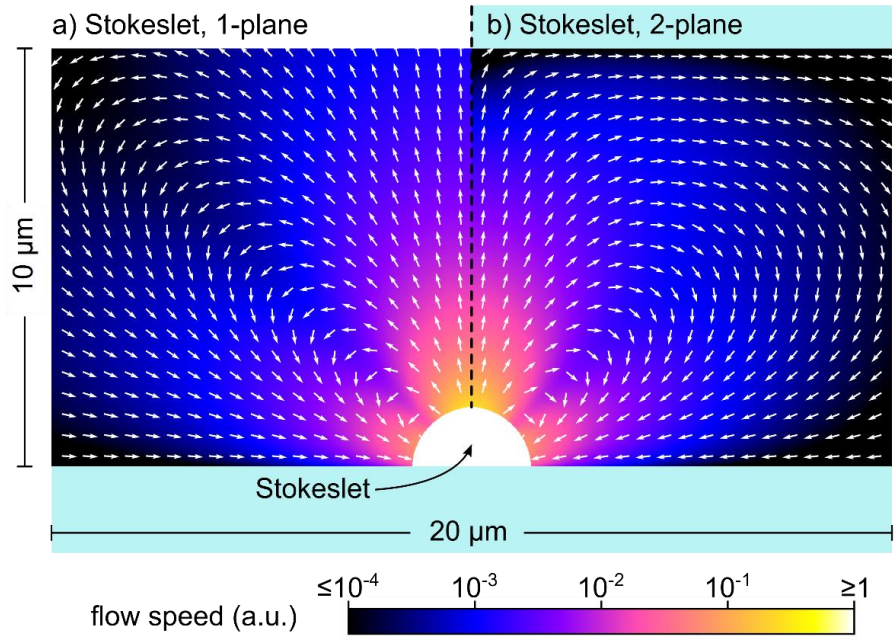

Figure 23 Stokeslet flow profile bounded by 1-plane (a) and 2-planes (b). White arrows indicate the flow direction.

[61] Note that for numerical evaluation of the Stokeslet between two parallel planes it is required to find the roots of the equation $\sinh^2 z = z^2$. In my experience neither the tabulated values nor the asymptotic limit provided by the reference were sufficient to obtain valid results. In order to evaluate for the velocity field it has been found that high precision numerical evaluation of the roots are required.

4 Experimental Methods

In the following chapter, the main experimental techniques used in the appended works are outlined.

4.1 Plasmonic Anti-Stokes Thermometry

When a laser illuminates a plasmonic particle, it will (subsequently) emit a broad inelastic radiation spectrum.(*89–91*) This emission, often referred to as the SERS background, has been explained by several mechanisms, such as fluorescence via hot carrier recombination following plasmon decay,(*92–95*) surface-enhanced fluorescence from contaminant molecules,(*96*) Raman scattering from electrons within the metal,(*97–99*) and damped image charges from nearby molecules.(*100*)

While the exact physical origin of the "SERS background" is still under debate, it has been demonstrated experimentally that the anti-Stokes[62] side of the emission spectrum shows a pronounced and well-defined dependence on temperature, which makes it suitable for thermometry purposes.(*97*, *101*, *102*) The theoretical anti-Stokes emission intensity, I_{AS}, varies with temperature, T, as:

$$I_{\mathrm{AS}}(\omega, \omega_{\mathrm{ex}}, T) \propto \aleph(\omega, \omega_{\mathrm{ex}}, T) \cdot C_S(\omega, \omega_{\mathrm{ex}}) \,. \qquad 4\text{-}1$$

Here, ω_{ex} is the frequency of the excitation light, and ω is the frequency of the emitted light. The factor $C_S(\omega, \omega_{\mathrm{ex}})$ accounts for how efficiently the plasmonic structure can scatter light into the far-field (essentially the scattering cross-section). The term $\aleph(\omega, \omega_{\mathrm{ex}}, T)$ is the Bose-Einstein thermal population factor,

$$\aleph(\omega, \omega_{\mathrm{ex}}, T) = \left[\exp\left(\frac{\hbar(\omega - \omega_{\mathrm{ex}})}{k_{\mathrm{B}} T}\right) - 1\right]^{-1} , \qquad 4\text{-}2$$

where $\hbar, k_{\mathrm{B}}$ are the reduced Plank's constant and Boltzmann's constant, respectively, while T is the absolute temperature.

By utilizing the anti-Stokes emission that occurs upon laser excitation of a plasmonic antenna, one can experimentally determine the antenna temperature. As seen from equations 4-1 and 4-2, if the coefficient C_S is known then the measured spectral distribution can be fit to these equations to obtain an experimental value for the temperature of the plasmonic antenna.[63]

[62] By "anti-Stokes side" of the emission spectrum I am referring to emitted light that has more energy per photon than the incident light.
[63] Note that this procedure assumes that the antenna temperature is approximately uniform. This approximation is generally valid and is justified in section 2.2.2.

However, for many applications, the coefficient C_S is not known (to a high enough precision). To circumvent this issue, a simple way to extract the antenna temperature is to measure two signals, one at a known temperature, T_{ref}, and the other at the temperature to be determined (T). Taking the ratio of the two spectra, the factor C_S is divided out, resulting in

$$\frac{I_{\mathrm{AS}}}{I_{\mathrm{AS,ref}}} = \frac{\aleph(\omega, \omega_{\mathrm{ex}}, T)}{\aleph(\omega, \omega_{\mathrm{ex}}, T_{\mathrm{ref}})} = \frac{\exp\left(\frac{\hbar(\omega - \omega_{\mathrm{ex}})}{k_{\mathrm{B}} T_{\mathrm{ref}}}\right) - 1}{\exp\left(\frac{\hbar(\omega - \omega_{\mathrm{ex}})}{k_{\mathrm{B}} T}\right) - 1}. \qquad 4\text{-}3$$

A schematic overview of the setup used to measure anti-Stokes photoluminescence is shown in Figure 24. Essentially, a monochromatic light source is focused on the plasmonic structure, and the same focusing optics can be used to collect the inelastic photoemission. The Rayleigh scattered light must be removed using optical filters, and the high energy inelastic photoluminescence is then sent to a spectrometer for spectral analysis. The laser excitation wavelength must be near a resonance of the structure to detect an appreciable anti-Stokes signal. For passive thermometry purposes, however, it is also imperative that the intensity of the excitation laser is sufficiently low so that it does not cause significant heating.

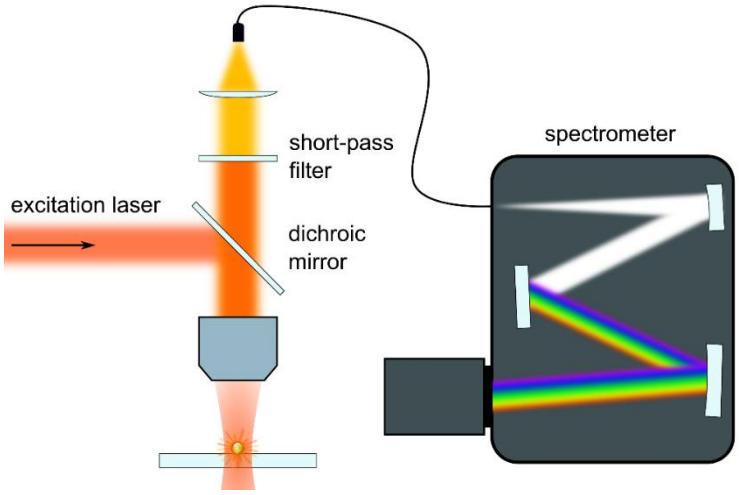

Figure 24 Schematic overview of the setup used to measure anti-Stokes photoluminescence from plasmonic nanostructures. An excitation laser is weakly focused onto a plasmonic structure by a microscope objective. The same objective is used to collect the inelastic photoluminescence emitted by the illuminated plasmonic structure. The collected light is then spectrally filtered to remove the Rayleigh scattered light. The high energy inelastic emission is sent to a spectrometer for spectral analysis. Note that the colours shown in the spectrometer are for illustrative purposes only and are not consistent with the colours used for the excitation laser and anti-Stokes inelastic emission.

4.2 Observing Thermophoretic Depletion

When a plasmonic particle is illuminated near a resonance, the enhanced absorption leads to a significant local temperature increase (see sections 2.1.2 and 2.2.2). As a results of this plasmonically induced temperature gradient, nearby colloids will tend to move towards colder temperature due to thermophoresis (see section 3.2). The thermophoretic depletion resulting from localized heating by a plasmonic nanoantenna can be monitored via imaging the distribution of fluorescently tagged nanoparticles in the local vicinity. This technique, illustrated in Figure 25, utilizes the projected fluorescence intensity profile to extract the local concentration of nanoparticles. It is important to note that the detected fluorescence intensity distribution has a significant contribution from out-of-focus fluorescent particles. Thus, to extract the actual nanoparticle concentration profile, a model-based deconvolution algorithm is required.

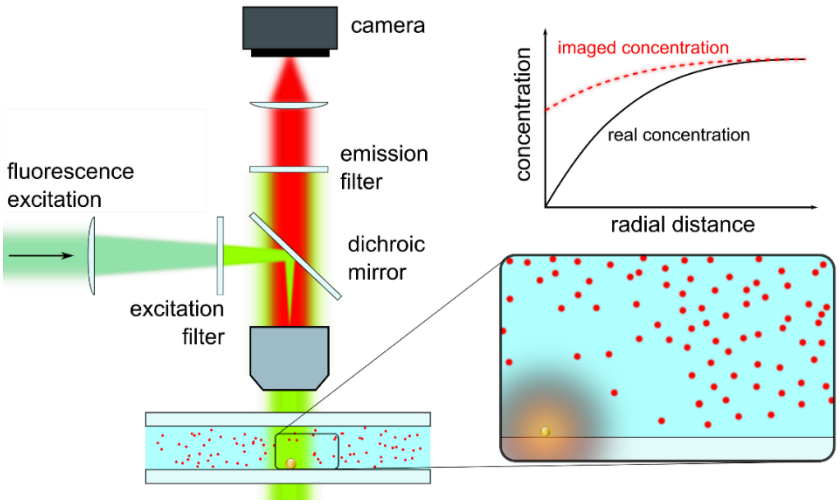

Figure 25 Schematic overview of the setup used to observe thermophoretic depletion.

The spatial light collection efficiency function (CEF) of the imaging objective must be determined to account for out-of-focus fluorophores. The CEF of microscope objectives has previously been studied in the context of particle flow cytometry experiments.(*103*, *104*) These results indicate good agreement between experimentally obtained CEFs and their theoretical approximations based on geometrical optics, wave optics, or Monte-Carlo ray-tracing simulations. A modified CEF based on the geometric optics "blue-circle" approximation is used here for its simplicity and numerical expediency. In this approximation of the CEF, an isotropic point source (e.g. a fluorescent nanoparticle) displaced from the image plane along the optical axis will project itself as a uniform intensity circle onto the camera detector array. The projected circle size depends on the distance from the image plane and the numerical aperture of the microscope objective. Therefore, this method accounts for the loss in spatial resolution of out-of-focus fluorophores as well as their significant contribution to the total detected intensity.

To utilize the CEF to reconstruct the *real* thermophoretic depletion from the observed projected intensity, an iterative least-squares fitting algorithm is used. This procedure assumes that the depletion profile is given by equation 3-18, and the temperature profile is given by equation 2-53.[64] For every observed point in the observed intensity profile, the detected intensity is calculated based on the CEF and the assumed concentration profile. The projected intensity distribution is then compared with the experimentally obtained results, and the parameters of the fit (i.e. the depletion profile) are updated until the projected intensity profile matches the experimental results. Additionally, the temperature dependence of the fluorescence emission can also be accounted for in this procedure. Once the projected intensity profile matches the experimental results, the corresponding depletion profile is then taken as the *real* depletion profile.

4.3 Optical Tweezers

The utilization of optical forces to manipulate particles precisely was pioneered by Arthur Ashkin in the 1970s.(*31*, *105*) The concept was then developed further in Ashkin's seminal work "Observation of a single-beam gradient force optical trap for dielectric particles" in 1986, which reported the technique that is now commonly referred to as optical tweezers.(*32*) The value of this technology was realized almost immediately and applied to studies of biological microparticles.(*106*) The next major advancement in optical tweezers came in the early 1990s when researchers began measuring external forces applied to trapped particles (referred to in this thesis as optical force microscopy).(*107*, *108*) Around this time, researchers also started to experiment with trapping multiple objects simultaneously using "beam-sharing" techniques based on galvo-mirrors and acousto-optic deflectors.(*109–111*) Finally, in the early 2000s, the technique of holographic optical tweezers was developed, which utilizes spatial light modulators to offer fascicle control of the 3D position of multiple optical traps.(*112*, *113*)

The basic configuration used in an optical trapping[65] experiment consists of a laser beam tightly focused by a high numerical aperture microscope objective. Particles with positive polarizability will experience a force which pulls them towards a point near the laser focal spot. Generally, the size of the probe particle and trapping wavelength are comparable, and therefore the Rayleigh approach, developed in section 2.1.4, is insufficient for accurately describing the optical forces involved (although the basic tenets of that analysis are still qualitatively true). Strictly speaking, this trapping regime is best suited for Mie theory;

[64] In principle other temperature profiles could also be accounted for if they are known either a-priori or have been experimentally determined. If large temperature variations are included, then the Soret coefficient temperature dependence (i.e. equation 3-19) can also be included in the fitting procedure.

[65] The terms "optical trapping" and "optical tweezers" are synonymous and will be used interchangeably.

however, a sufficient understanding of the working principles can be more intuitively obtained by considering the ray-optics approximation illustrated below in Figure 26.

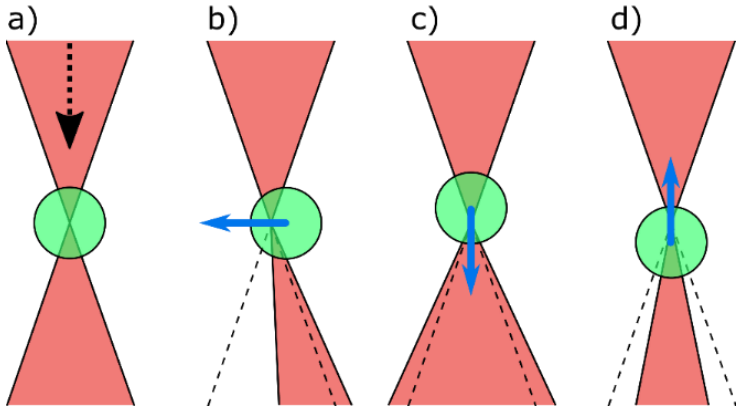

Figure 26 Overview of optical trapping gradient force in the "ray-optics" regime. The focused laser beam (red) is incident from the top with a dielectric microparticle (light-green) near the laser focal spot. a) Nominal position of the trapped particle at equilibrium. b)-d) Small displacements of the trapped particle showing the change in transmitted light propagation and the corresponding force that acts on the trapped particle (blue arrows) in response as required by conservation of momentum.

When the particle is centred at the focal spot, the system is symmetric about that point, and the transmitted light has the same angular intensity distribution as the incident light (Figure 26a) – thus, there is no change in momentum of the light and therefore no force acting on the particle. On the other hand, for small displacements of the probe particle, the net direction of transmitted light changes in response (Figure 26b-d). Therefore, as required by conservation of momentum, a restoring force is imparted on the trapped particle, which brings it back towards the focal spot of the trapping laser.

Because of the additional radiation pressure force (not illustrated in Figure 26), the particle tends to be displaced slightly away from the laser focal spot along the optical axis. For this reason, highly focused beams are typically required to ensure that any small perturbation of the trapped particle position will result in a resorting force towards the focal spot. Using this methodology, one can stably trap dielectric microspheres in water, being able to overcome other external forces (e.g. gravity) and Brownian motion to maintain confinement of the trapped particle. For small perturbations to the position of a trapped particle, the restoring optical force is approximately linear with displacement, i.e.

$$F_{i,\mathrm{trap}} = K_i \Delta r_i \,. \qquad 4\text{-}4$$

In addition to being able to confine the trapped particle, an additional layer of functionality is achieved if the trapped particle can be transported. The transport of a trapped particle is typically accomplished either by moving the environment around a stationary trap or by moving the laser focal spot. The second methodology, moving the focal spot, is often required when other constraints

force the environment to remain static.[66] One way to achieve control over the trapping laser focal spot position is to use a "4-f correlator," as shown in Figure 27. Using this setup, by controlling the convergence and direction (i.e. $\vec{k}$ spatial distribution) of light at a conjugate Fourier plane, the position of the focal spot can be specified in 3D.

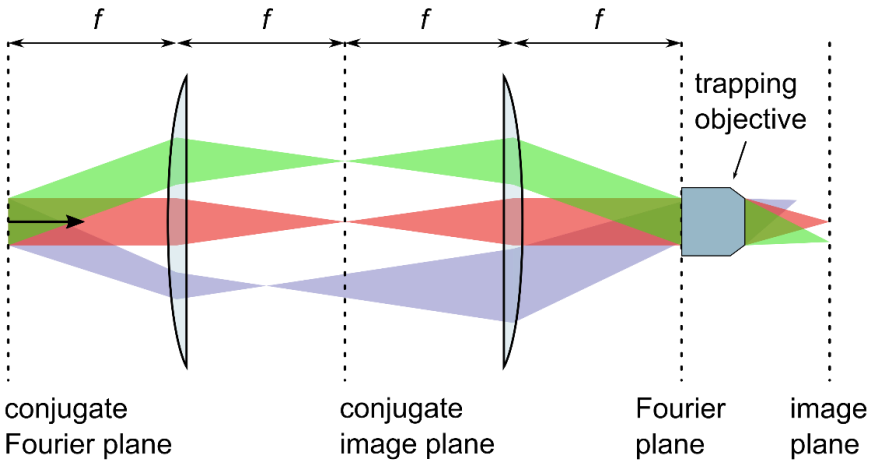

Figure 27 A 4-f correlator used to control the location of a laser focal spot. Three cases are shown: nominal beam path (red), deflected beam path (green), deflected and convergent beam path (blue).

4.3.1 Holographic Optical Tweezers

A convenient and versatile way of controlling the convergence/direction of light at a conjugate Fourier plane is through a spatial light modulator (SLM) in a technique known as *holographic* optical tweezers. A spatial light modulator is a device that enables precise control of the light phase profile at a specified plane. The most common realization of an SLM is a "liquid crystal on silicon"-SLM, which consists of a 2D array of liquid crystal cells on top of a reflective silicon mirror. Each element in the 2D array of liquid crystal cells can have the applied voltage independently controlled, which changes the orientation of the liquid crystal molecules. The effective optical path length through the cell and, therefore, the phase profile of the reflected wavefront can be controlled, as shown in Figure 28a.

[66] As is the case in appended Paper iii.

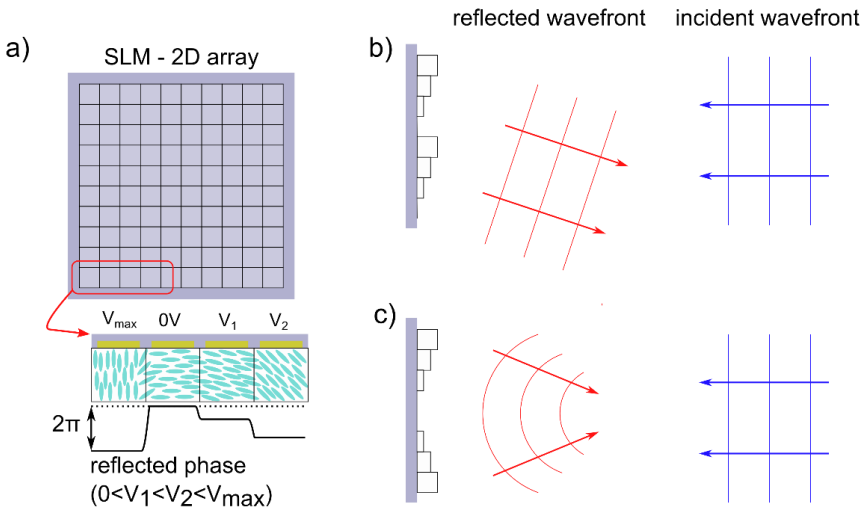

Figure 28 Liquid crystal on silicon SLM operation. a) Working principle. b) SLM acting as an angled mirror. c) SLM acting as a concave mirror. In b) and c) the square blocks correspond to the discretized relative wavefront of the reflected beam.

By creating a specified optical path length for each pixel in the 2D array, the SLM can impart a controllable phase profile onto the reflected beam, thereby controlling the wavefront. Thus, by placing the SLM at a conjugate Fourier plane, the spatial $\vec{k}$ distribution can be uniquely controlled with high spatial and phase precision and a relatively high address rate.[67] Note that the controllable order of the SLM is in the +1st diffracted order,[68] and the 0th order light is often physically blocked from reaching the sample.

The simplest way to control an SLM for controlling the 3D position of a focal spot is by creating a superposition of a prism and a lens.(*112*) Control over the optical trap position within a plane orthogonal to the optical axis is achieved by using the SLM to apply a linear phase profile (along each axis) to the reflected laser beam, i.e. acting as a prism (Figure 28b, equation 4-5). Displacement of the optical trap along the optical axis can be controlled by using the SLM to apply a variable phase curvature to the reflected beam, i.e. acting as a lens (Figure 28c, equation 4-6). These phase effects can be expressed as

$$\phi_{\text{prism}} = m_x x_i + m_y y_i \qquad 4\text{-}5$$

and

$$\phi_{\text{lens}} = m_z((x_i - x_0)^2 + (y_i - y_0)^2)\,, \qquad 4\text{-}6$$

where, x_i and y_i correspond to the location of pixels on the SLM, and x_0,y_0 is the centre pixel. For simplicity is also assumed that the SLM coordinate axis is

[67] Address rate ≈ 30 Hz for the device used in this study.
[68] In principle any diffraction order could be used however over 80% of the reflected light intensity is contained in the +1st order.

aligned with the coordinate axes in the frame of reference of the optical trap. The coefficients m_x, m_y, and m_z are scaling coefficients that dictate the displacement of the optical trap from its nominal position along the x, y, and z axes, respectively.

Because the phase depth of the SLM is limited, and because the phase offset is cyclical in nature, the actual phase profile applied to the SLM is modulated by 2π. Thus the actual phase profile corresponds to the superposition of a blazed grating and a Fresnel lens:

$$\phi^{\mathrm{SLM}} = \mathrm{mod}_{2\pi}\left(\phi_{\mathrm{prism}} + \phi_{\mathrm{lens}}\right) \qquad 4\text{-}7$$

4.3.2 Optical Force Microscopy

In addition to being able to impart forces on trapped objects, the change in transmission direction that occurs when a trapped particle is perturbed can also be used to measure external forces. This is achieved by collecting the transmitted light and analyzing changes in the $\vec{k}$-vector distribution, which corresponds to changes in the intensity distribution at a conjugate Fourier plane. Therefore, by measuring these intensity changes, the position of the trapped particle can be determined, as outlined in Figure 29.[69]

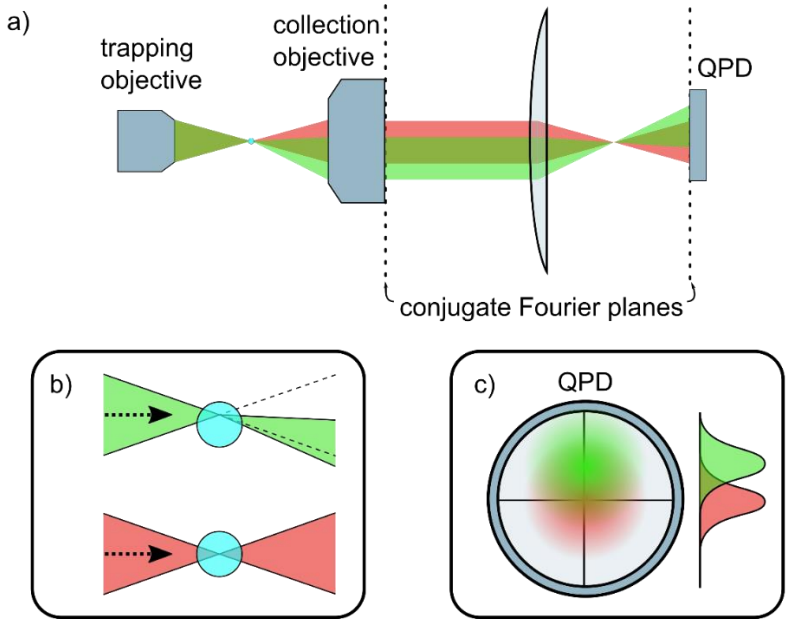

Figure 29 Measuring trapped particle displacement via transmitted light. a) Overview of the experimental setup. The back focal plane (Fourier plane) of the collection objective is imaged onto a QPD. b) Example of how particle displacement causes a change in the transmitted light. c) Intensity distribution on QPD that results from particle displacement.

[69] The actual drawing of the light trajectories shown in Figure 29 is slightly misleading and is only for pedagogical purposes. In reality the two light paths essentially overlap and only the intensity distribution changes.

Often the intensity distribution changes are is measured with a quadrant photodiode (QPD). A QPD is essentially just four photodiodes arranged in a 2×2 array (Figure 29c). The QPD outputs three voltages as signals which correspond to the difference between the top and bottom row (ΔTB); left and right column (ΔLR); as well as the sum of all four quadrants (Σ). Changes in these three output signals correspond to particle displacements along the x, y, and z axes respectively.[70] When the trapped particle is located at its nominal position, the QPD position is adjusted so that the $\Delta TB = 0$ and $\Delta LR = 0$. Then movement of the particle (along any axis) will correspond to a change in the voltage output for each signal.

A key requirement of this measurement technique is that a linear change in particle position corresponds to a linear change in the signal output from the QPD. This also implies that a linear change in particle position corresponding to a linear change in the output light momentum, ensuring that the restoring force is Hookean (equation 4-4). To check this, the trapped bead is adhered to a microscope slide, and the trapping focal spot is scanned through the centre along each principal axis. The QPD response to particle displacement is shown in Figure 30. Also shown here are histograms of measured displacements during an experiment that confirms that we are operating within the linear regime for both detection and restoring force.

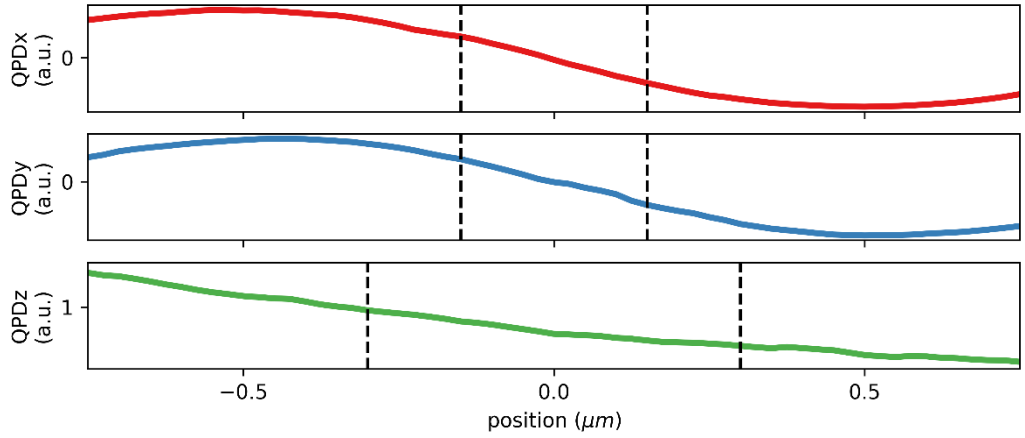

Figure 30 Testing that particle displacements are within the linear regime. A 2 μm microsphere is attached to a glass slide and scanned through the laser focal spot along each coordinate axis. The lines show the QPD response vs the bead displacement from its nominal position. In general, the displacements of the bead are within approximately ±150 nm along the x-axis and y-axis and ±300 nm along the z axis (indicated by dashed vertical lines).

The final step towards being able to monitor the position of the trapped particle (and therefore able to extract forces from the Hookean model) is to calibrate the QPD response. One method that provides a simple in-situ calibration is through

[70] Note that ΔTB and ΔLR can correspond to either x and y; y and x; or some linear combination of the two depending on the orientation of the QPD. With proper alignment it can be made soe that the QPD frame of reference properly matches the particle frame of reference (as dictated by the camera, microscope stage, SLM etc).

analysis of the power spectrum.(*114*) While within the linear regime of optical trapping, the trapped particle is well approximated as a Brownian particle in a harmonic potential.[71] Thus, as discussed in section 3.1, the power spectral density is described by equation 3-15 (or 3-14) and shown in Figure 19c. Therefore, this time series from the QPD can be converted into a PSD and fit with equation 3-15 (or 3-14) to experimentally determine the trap stiffness K and a conversion factor β which converts our signal in volts to the particle displacement in metres.[72]

Removing the SLM phase ripple

SLMs have an inherent phase instability that results from the refresh rate of the phase pixels. Thus, in addition to calibration of the optical trap, this phase instability must also be removed. The SLM phase instability manifests itself as an oscillation in the 1st order diffracted beam intensity at a discrete set of frequencies. In the setup used in appended Paper iii, these phase oscillations corresponded to less than 2% of the reflected light intensity; however, this can still result in a measurable change in the transmitted signal distinct from the Brownian motion of the particle. To remove this component of the signal high quality-factor digital notch filters were applied anywhere the phase instability was observed is the power spectral density. With the application of these filters, these digital filters, the phase oscillations could be removed while causing essentially no perturbation to the remainder of the signal.

Transient force measurements with optical tweezers

To measure forces with an optical tweezer, most past works have typically been limited to a time resolution of $1/f_c$. The reason for this is that most studies use the approximation

$$F_{\text{ex}} \approx Kx\,. \tag{4-8}$$

Therefore at time scales smaller than $\approx 1/f_c$, when the drag force $(-\gamma_0\dot{x})$ is dominant over the spring force, then strictly applying equation 4-8 would underestimate the force acting on the particle. However, this time resolution can be significantly increased if the velocity term from the Langevin equation is included, i.e.

$$F_{\text{ex}} = \gamma_0\dot{x} + Kx\,. \tag{4-9}$$

[71] Note that the simple Lorentzian model for confined Brownian motion was compared to a more correct hydrodynamic model. It was found that the Lorentzian model (given in section 3.1) was found to be sufficient for our purposes. See ref (*114*) and the appendix (sections 7.2 and 7.2.1 – "frequency-dependent" effects) for further details on the hydrodynamic model.

[72] This is done simultaneously for all three axes, so as to give three trap stiffnesses and conversion factors.

There are two requirements to perform this type of "transient" force measurement with optical tweezers: 1) the drag coefficient of the particle must be known, and 2) for time scales $< 1/f_c$ the particle velocity must have an autocorrelation that is not a delta function. As a note with regards to appended Paper iii, in cases where the external force is driven by fluid flow, and it is the local flow velocity that is desired, equation 4-9 can be rewritten in terms of the local flow velocity by using the relation $\vec{F}_{\mathrm{ex}} = \vec{u}\gamma_0$, thus

$$u_i = \dot{x}_i + 2\pi f_{c,i} x_i \,. \qquad 4\text{-}10$$

4.4 Plasmonic Optical Tweezers

From the discussion in section 2.1.4, it would appear that smaller particles are *easier* to trap than large particles since for dielectric nanoparticles $F_{\mathrm{gradient}} \propto a^3$ and $F_{\mathrm{radiation}} \propto a^6$, thus the gradient force will typically be more dominant relative to the radiation pressure force as a particle gets smaller.[73] However, as we saw in section 3.1, the Brownian motion of a particle tends to increase as the particle size decreases, i.e. $D \propto a^{-1}$. Because of this increase in Brownian motion and the significant decrease in amplitude of the gradient force, small particles are typically more difficult to stability trap when compared to large particles.

One method of overcoming this limitation is through the use of plasmonic optical tweezers. In this methodology, a plasmonic antenna is used to amplify and confine the local electric field intensity in order to enhance the optical gradient force (equation 2-37). If the force is enhanced sufficiently, it can overcome the effects of Brownian motion and even trap dielectric nanoparticles.(*3*, *115–118*) The general strategy employed for plasmonic optical trapping is to illuminate a noble metal nanoantenna so that plasmonic resonances create local regions of electric field enhancement as shown in Figure 31. If a nanoparticle is brought into the immediate vicinity of the illuminated antenna, the nanoparticle can be trapped by the plasmonically enhanced electric field.

[73] Note that this is strictly only true for non-absorbing particles. For absorbing particles, the radiation pressure force will also scale with volume, i.e. $F_{\mathrm{radiation}} \propto a^3$.

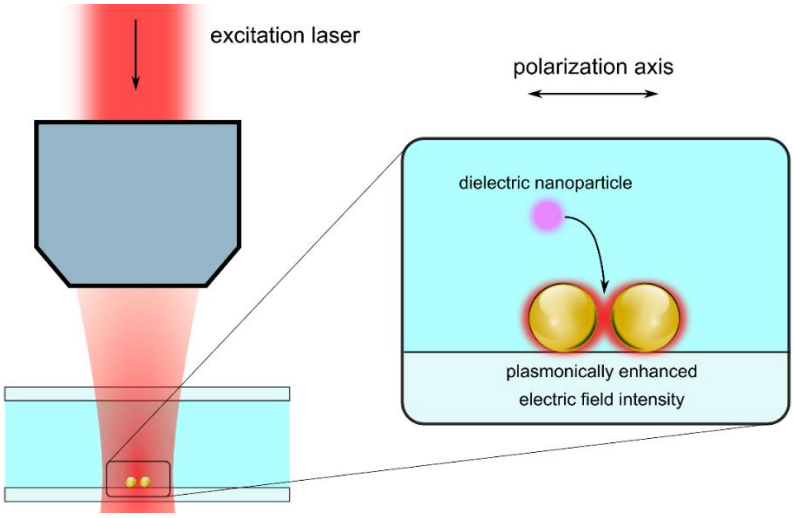

Figure 31 Principle of plasmonic optical tweezers. An excitation laser illuminates a plasmonic nanostructure to generate local regions of electric field enhancement. The resulting high-intensity field/gradients increase the optical gradient force permitting the trapping of nearby dielectric nanoparticles.

4.5 Thermoplasmonic Bubble Generation

Recently there has been significant interest in utilizing plasmonically enhanced heating to generate bubbles in water. One field where thermoplasmonic bubbles show perhaps the most promise is as active manipulation elements in microfluidic systems. Flow control via bubble formation has been demonstrated where a thermoplasmonic bubble can physically block fluid flow. This was demonstrated in 2011 by Zhang et al., where chromium pads were used to absorb 980 nm light to generate a bubble in a microfluidic channel.(*119*) The presence of a bubble could then be used to block a microfluidic channel, thereby acting as a valve providing far-field optical control of the microfluidic system. The authors also showed how the expansion or contraction of a bubble could induce fluid flow and act as a pump. This technique was extended to a fibre-optically controlled system in 2014 by Kim et al.; here, a fibreoptic microheater was created by the deposition of titanium on the tip of a fibre attached to a microfluidic channel.(*120*) Once again, the plasmonically enhanced absorption was used to thermally generate a bubble that could inhibit fluid flow.

Thermoplasmonic bubbles can also be used to actively generate flows within a microfluidic system via Marangoni/thermo-capillary convection (see section 3.3.1 and 3.3.2). Such flows have been experimentally observed from bubbles generated on gold films,(*121*) and around plasmonic nanoparticle clusters.(*122*) The ability for such flows to be utilized as extremely versatile active microfluidic controlled elements has been investigated by Namura et al., where they have found that by controlling the temperature gradient profile, different flow patterns, including particle jets, could be formed,(*123*) and that by changing the solvent properties the flow can be suppressed or even reversed.(*124*) In 2017 it was shown that by limiting the bubble diameter to approximately 10 µm via degassed water, extreme flow speeds approaching 1 m/s could be achieved.(*56*)

These Marangoni flows have previously been demonstrated as a means of direct particle printing as particles in a solution are driven by the flows and deposited at the intersection line where the bubble meets the substrate.(*125*, *126*)

Past works on thermoplasmonic bubble generation have typically utilized either semicontinuous plasmonic films(*56*, *126*) or 2D nanoparticle arrays.(*50*, *52*) This methodology enables simple alignment as well as control of the position of the generated bubble but tends to result in bubbles that are large (diameter $>$ 10 μm) and thus slowly dissipating (see section 2.3.1). Restricting bubble growth can be achieved by utilizing degassed water; however, this is impractical for many applications. To generate bubbles that are small and quickly dissipating within air equilibrated water (and thus permitting fast bubble modulation), it is critical to use an isolated heating structure such that the overall volume of heated water remains constrained. Previously, bubbles have been formed around a single colloidal gold nanosphere at a glass-water interface; however, this resulted in a temperature increase upon bubble nucleation, which destroyed the gold nanosphere creating a cluster of remnant nanoparticles.(*122*, *127*) Thus, to maintain a well-defined heat source density, it is necessary that sufficient thermal coupling exists between the plasmonic nanoantenna and the substrate (see section 2.3.2 and ref(*44*)).

A generic overview of using isolated plasmonic nanostructures for bubble generation is shown in Figure 32. When the heating laser intensity is high enough such that the local water temperature is above the kinetic spinodal temperature (see section 2.3), then a bubble can form. These bubbles are adhered to the substrate and encompass the plasmonic structure. Additionally, once formed, the bubble will persist as long as the heating laser intensity is maintained. Generally, large collections of plasmonic nanostructures will generate large bubbles because of the increase in the volume of heated water. See appended Paper ii for further details about bubble generation around isolated thermoplasmonic structures.

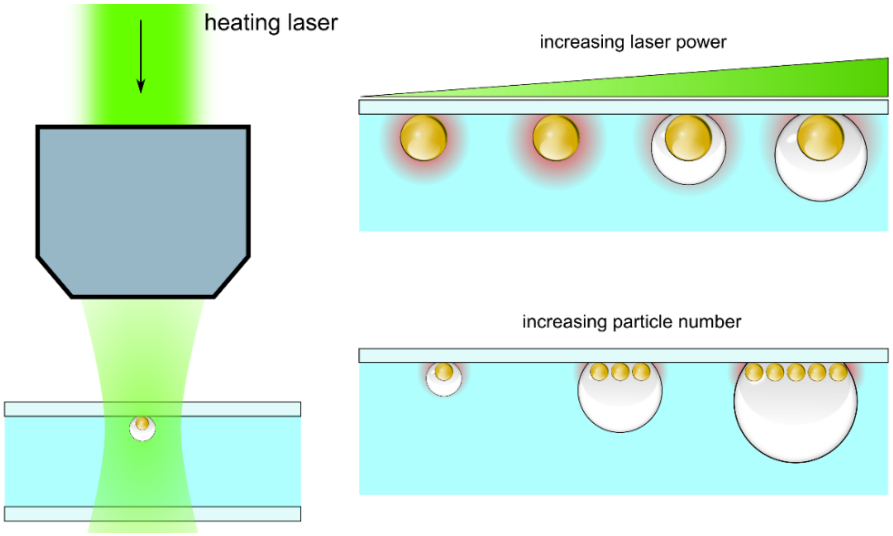

Figure 32 Thermoplasmonic bubble generation. A resonant laser illuminates a plasmonic nanoparticle surrounded by water to generate local superheating. Once the local temperature has passed the kinetic spinodal threshold a bubble if formed. Larger collections of nanostructures lead to more efficient heating as well as larger volumes of heated water, and therefore larger bubbles.

4.6 Thermoplasmonic Bubble Detection

The bubbles formed around isolated thermoplasmonic nanoantennas are, in general, too small to be accurately imaged with standard microscopic techniques (e.g. darkfield/brightfield imaging). This is both a technical and fundamental limitation. For some of the bubbles investigated, the bubble size is near the diffraction limit, and thus no spatial information is possible to be resolved with optical imaging. For some of the larger bubbles formed,[74] while above the diffraction limit, the optical contrast of the bubble is obfuscated by other effects such as plasmonically enhanced fluorescence from the glass/nanoantennas. Additionally, the fast dynamics of these bubbles are too quick to provide sufficient integration time (with standard scientific cameras) to accurately image even if all other obfuscating effects were absent.

Therefore, to detect bubble formation and dissipation, we utilized a scattering detection technique inspired by ref(*128*). In this method, a detection laser is coaligned with the plasmonic nanoantenna/heating laser. Changes in the backscattered or transmitted light are used to infer the presence/absence of a bubble, as shown in Figure 33. Using this technique, the presence/absence of a bubble can be detected with high temporal accuracy. Generally, the detection signal increases/decreases when a bubble is present for the backscattered/transmission-based detection schemes (respectively). However, the signal is highly nonlinear with bubble size as predicted by numerical simulations and confirmed via experimental results. This non-linear response, in conjunction with uncertainty about the bubble contact angle, prevents the signal from being used as a direct measurement of the bubble size. Regardless, this

[74] Note that even these “larger” bubbles are still “small” as defined in section 2.3.

detection methodology is sufficient for providing a binary measure of if a bubble is/is-not present.

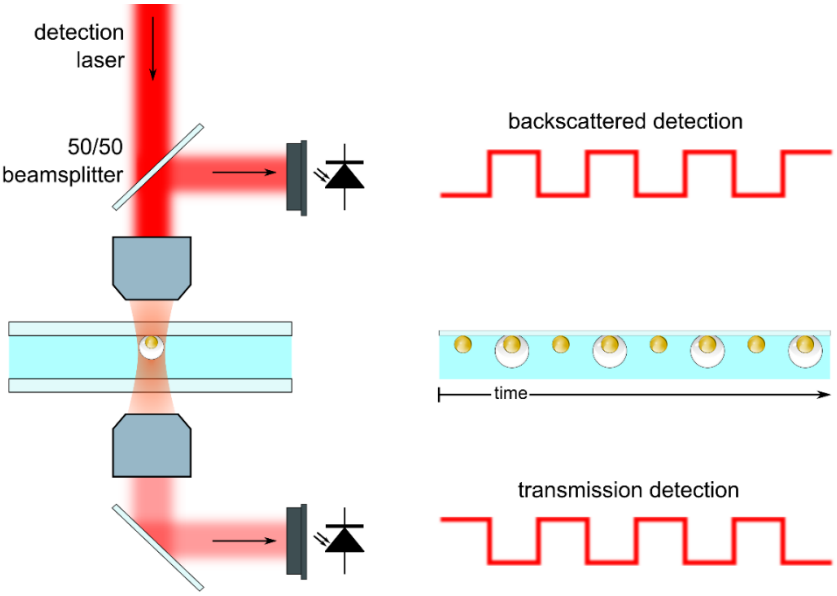

Figure 33 Bubble detection via backscattering and transmission of a detection laser. A detection laser is focused onto a thermoplasmonic structure used for bubble generation. The formation of a bubble results in a signal change to the backscattered/transmitted light that can be detected with a photodiode.

4.6.1 Estimating Bubble Size

Although this bubble detection method cannot directly measure bubble size, it can measure the lifetime of the bubbles after the heating laser has been turned off. This is achieved by monitoring how long the backscattered/transmitted signal takes to return to its baseline "pre-bubble" state. From the measured lifetime, it is possible to extract an effective bubble size with equations 2-77 and 2-78 from section 2.3.1.[75]

[75] Note that the full nonlinear form of the bubble lifetime equation was used.

5 Summary of Appended Works

5.1 Paper i: Photothermal Heating of Plasmonic Nanoantennas: Influence on Trapped Particle Dynamics and Colloid Distribution

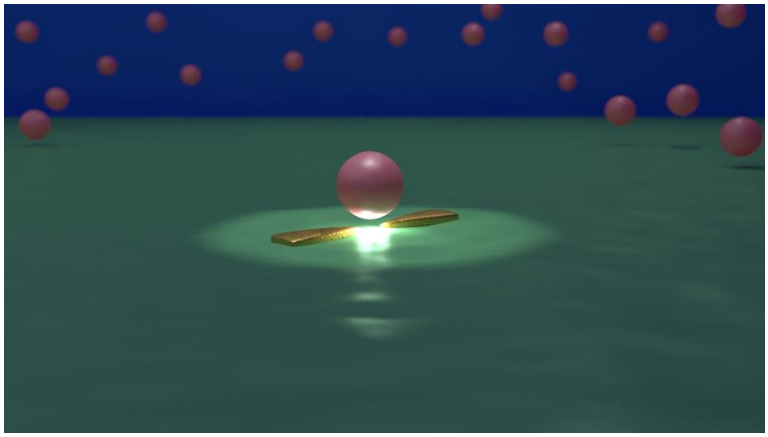

Figure 34 Table of contents figure from Paper i. Reproduced with permission from ref(117). Copyright 2018 American Chemical Society.

This study was motivated by the field of plasmonic optical trapping (section 4.4) and specifically the associated thermal effects. In plasmonic optical trapping, the electric field confinement provided by plasmonic nanostructures is used to enhance the optical gradient force, thereby allowing smaller particles to be trapped than is possible with a conventional optical trapping setup (i.e. one using only "far-field" optics).(*44*)This method can be combined with other spectroscopic interrogation techniques to identify/analyze the trapped particle.(*118*, *129*) While the ability of plasmonic optical traps to impart forces and localize small dielectric nanoparticles has been demonstrated on many occasions, often the associated thermal effects have been ignored. The absence of specific studies investigating the interplay between optical forces and thermal effects is noteworthy since studies directly use thermal forces to manipulate particles in an experimental configuration remarkably similar to those used in plasmonic optical trapping.(*74*, *75*)

In this work,(*117*) a standard optical trapping platform was implemented, utilizing gold bowtie nanoantennas as optical transducers to impart forces on colloidal dielectric nanoparticles. Facilitated by recent advances in thermometry of plasmonic structures (see section 4.1), the temperature of the plasmonic antennas were directly measured. Utilizing these temperature measurements, the behaviour of the trapped particle was investigated in relation to the local temperature as well as the antenna resonance conditions.

As expected, if the resonance wavelength of the plasmonic antenna was close to the excitation wavelength, then enhanced confinement was observed at lower powers. This simply results from the fact that there is greater interaction between

the antenna and the excitation laser resulting in more electric field enhancement and, therefore, greater optical forces. However, structures that are resonant with the excitation laser are also heated more efficiently. When the trapping characteristics were instead compared to the local temperature, a surprising invariance was observed with respect to the resonance condition. Essentially, the degree of particle confinement for all structures was nearly identical for the same local temperature. Although a resonant structure can reduce the input power required to plasmonically trap a particle, this result implies that there is essentially no benefit to using resonant structures for trapping temperature-sensitive analytes because heat is also generated more efficiently.

Of even greater importance is the effect of this plasmonic heating on nearby particles that have not been optically trapped. As discussed in section 3.2, the presence of a temperature gradient induces particles to move thermophoretically, typically towards colder regions, i.e. away from the plasmonic antenna. This is significant since plasmonic optical traps are not (typically) mobile. The standard method used to trap a particle is to optically excite the antenna and wait for the analyte to randomly diffuse towards the antenna, where it will then be held by optical forces. However, since the induced temperature gradient effectively repels particles from the antenna, this can prohibit optical trapping or make it significantly less likely. Because the temperature profile extends for several microns away from the antenna while optical forces are only significant for a few hundred nanometres at best, particles will typically only experience these thermophoretic effects. Using epifluorescence microscopy, it was possible to observe the extent of thermophoretic depletion (section 3.2) and compare this with the local temperature increase of the plasmonic antenna. This depletion was found to extend several microns away from the antenna and could even cause nearly 100% depletion in its local vicinity.

This result is significant regarding making an efficient plasmonic trapping platform and also has implications in other fields. For instance, many works have used plasmonic structures for passive sensing. One such scheme is to functionalize the gold surface and monitor the resonance condition via darkfield scattering. As analytes bind to the functionalized surface, they modify the local refractive index and, therefore, the resonance condition. This is the basis of localized surface plasmon resonance sensors. While the intensity of white light used in these schemes is often much less than the laser intensity used in plasmonic optical trapping, there can still potentially be a local temperature increase of at least a few Kelvin. Because of the exponential dependence of local analyte concentration on temperature, this can induce non-negligible effects on the observed signal response, which affects the extracted binding parameters. In this regard, Paper i serves as a guideline for how thermophoretic depletion can affect any system that utilized plasmonic particles as a means of manipulating or sensing analytes in solution.

5.2 Paper ii: Ultrafast Modulation of Thermoplasmonic Nanobubbles

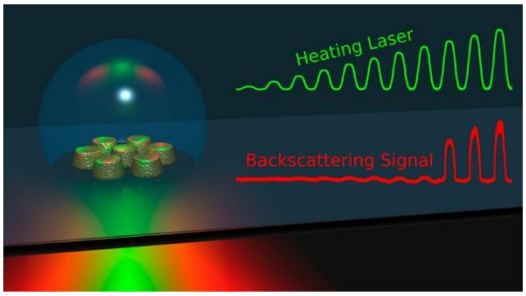

Figure 35 TOC figure from Paper ii. Reprinted with permission from ref(44). Copyright 2019 American Chemical Society.

Recently there has been significant interest in the formation of bubbles around plasmonic structures that are excited by a continuous wave laser.(*50*, *52*) The formation of a bubble can induce many interesting effects, such as thermocapillary flow, which may be useful for mass transport.(*56*, *121*) Recent studies on bubble formation/dissipation and the associated thermocapillary flows have been focused on large microbubbles that tend to be relatively stable. This stability means that even after the laser illumination has stopped, the bubble will persist for a significant amount of time (tens to hundreds of seconds). This is a problem for many high throughput applications since the long dissipation time effectively limits the rate at which the system can be addressed. One method to improve the effective throughput is by creating smaller nano-bubbles.

There are two difficulties with creating smaller nano-bubbles. First, it is difficult to prevent a thermoplasmonic bubble from growing into a microbubble in many experimental configurations. Second, it is difficult to observe nano-bubble formation/dissipation, which creates a barrier to investigating the process. In Paper ii,(*44*) we utilized optical backscattering to directly observe nanobubble formation (see section 4.6) and study how the bubble formation is affected by the plasmonic heating structure (section 4.5). Our findings show that the size of the plasmonic structure determines how small a bubble can be made, which dictates the minimum bubble dissipation time and, therefore, the maximum modulation rate. This results from the efficiency that a plasmonic structure can heat its environment. Essentially, the smaller a structure is, the more localized the heating will be and, therefore, the smaller the bubble size. In this work, the dissipation times of these bubbles were directly measured. It was found that they could vary from several tens of microseconds to tens of milliseconds depending on the structure size and heating laser power. Such bubble sizes correspond to maximum bubble modulation rates on the order of 100 Hz for the large thermoplasmonic nanoantennas to more than a kilohertz for the small antennas.

5.3 Paper iii: Strong Transient Flows Generated by Thermoplasmonic Bubble Nucleation

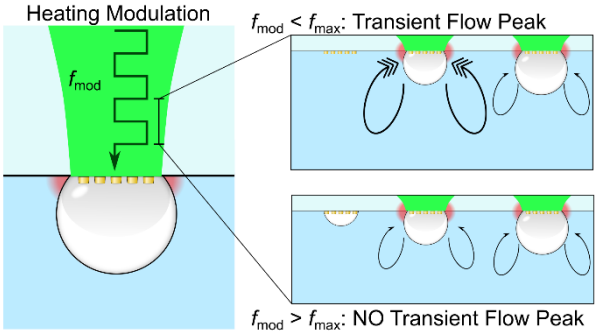

Figure 36 TOC figure from Paper iii.

As a direct continuation of the study initiated by Paper ii, it became of paramount interest to determine the flow speeds/forces achievable by the bubbles generated around these thermoplasmonic nanoantennas. Past studies on such flows have predominantly been focused on large bubbles (diameter $> 10\ \mu m$) under steady-state conditions and primarily used tracer particles to visualize the flow pattern. For the small bubbles introduced in Paper ii, tracer particles are not suitable because of their propensity to adhere to the bubble and perturb the system during measurements.[76] Additionally, because of the high modulation rates accessible by these bubbles, transient effects become imperative to understand.

For these reasons, it was decided to develop a holographic optical tweezer force measuring system to perform transient velocimetry measurements during the bubble modulation cycles (section 4.3). This velocimetry technique has the advantage of offering high spatial precision of the probe location and significantly increased time resolution compared to what is achievable with most video microscopy systems. Furthermore, this method provides a full vectorial resolution of the local flow speed, which can be difficult to achieve with standard imaging techniques based on tracer particles.

Our results showed that the small bubbles generated by an isolated thermoplasmonic antenna were able to create an impressively fast local flow speed ($\approx 200\ \mu m/s$ at a distance of $7\ \mu m$ from the antenna/bubble) that is well approximated by a Stokeslet, and thus extends far into the surrounding medium. It was also observed that immediately upon nucleation, a strong transient flow peak occurs, which is approximately an order of magnitude faster than the subsequent persistent flow speed ($\approx 4\ mm/s$ at a distance of $7\ \mu m$ from the antenna/bubble). This transient flow peak exhibits the same qualitative flow profile as the subsequent persistent flow. The presence of this transient flow peak

[76] For larger bubbles this is less of a concern as the tracer particles are much smaller than the bubble.

is intrinsically tied to the bubble nucleation event as evidenced by the complete absence of a transient peak when bubbles are modulated at rates too fast to permit full bubble dissipation before the start of the next cycles (i.e. no nucleation event). Further investigation on bubble formation in different aqueous glycerol solutions suggests that the origin of the transient flow peak is due to the physical expulsion of water during nucleation instead of thermocapillary effects.

The presence of a transient flow peak and its dependence on the nucleation event highlights the need for fast bubble modulation rates to be achievable to fully optimize the performance of these bubbles in the context of active manipulation devices. Such bubbles are envisioned as efficient flow actuation devices coupled to conventional surface-based sensors in confined microfluidic environments to increase the interaction rates between the sensor and analytes, particularly when attempting to sense analytes a low concentration.

6 Outlook

The ability for plasmonic nanostructures to act as efficient, localized heat sources provides many opportunities that may be exploited in microfluidic systems. An interesting avenue is to tailor the system to generate a specific heat source density profile such that a controllable temperature profile is produced.(*130*, *131*) This type of system design can be utilized to exploit the inherent thermophobic response of many particles to create controlled diffusion of the particles through an environment. Furthermore, variation in the thermophoretic properties of different particles might permit particle separation/filtering or even sensing applications. Recently, a biomolecular binding sensing technique, microscale thermophoresis,(*8*, *9*, *73*) has emerged that utilizes changes in the thermophoretic behaviour before/after a binding event to determine the binding affinity in situations where conventional plasmonic sensors are generally insensitive to the change. This type of sensing configuration is highly suited for future speed and sensitivity enhancements through integration with plasmonic heat sources.

Continuing with the thread of thermoplasmonically generated bubbles, such systems have been shown as advantageous for localized flow generation in microfluidic environments, thus enabling signal enhancement in sensing applications(*7*, *132–134*) as well as for lithographic purposes.(*125*, *126*, *135–137*) Further advances may be possible by creating a controllable flow profile. This is potentially achievable either by breaking the symmetry of the system via geometric confinement or alternatively, by optically controlling the heat source density. Furthermore, it has already been demonstrated that the solvent type profoundly influences the established Marangoni flow speed.(*124*) Thus, further optimization can therefore be expected from finding specific solvent conditions that generate large surface tension gradients and therefore high flow speeds. Regarding the transient flow peak observed, higher bubble modulation rates may be possible to better utilize this phenomenon. Beyond optimizing the individual bubble actuator, the full potential of this flow generation methodology has yet to be seen, especially if multiple elements can be created to work in tandem, both spatially and temporally. In particularly if a high degree of flow directionality can be established for each unit element, arrays of such bubbles may be able to generate bulk fluid motion or even programmable fluid flow profiles that are controllable, in real-time, via structured illumination from the far-field.

7 Appendix A – Fluid Mechanics

In this section, the physics of fluid mechanics is discussed as it pertains to the contents of the main text. Specifically, the discussion is restricted to that of homogeneous, incompressible, and Newtonian fluids since these approximations can be used to effectively describe the behaviour of water on the length and time scales investigated here. In addition to discussing some of the fundamental principles of fluid mechanics, the specific situation of the drag force acting on a sphere due to relative fluid flow is investigated. Much of the following section is adapted from the textbook "Fluid Mechanics" by Landau and Lifshitz.(*46*)

7.1 Fluid Flow

To investigate the mechanics of fluid motion, we begin by considering some arbitrary volume V_0 within a simple fluid with density ρ_f. At any region on the surface of V_0 the mass flux across surface element dS, due to local fluid velocity $\vec{u}$, is given by $\rho_f \vec{u} \cdot d\vec{S}$ where $d\vec{S}$ is the normal vector of the surface element, which has area $|d\vec{S}|$. Thus, the total mass transport across the surface of V_0 is

$$\oint_S \rho_f \vec{u} \cdot d\vec{S} \,. \tag{7-1}$$

From the principle of conservation of mass, the rate of change of mass within V_0 must be equal to the total mass transport across the surface, i.e.

$$\frac{\partial}{\partial t}\int_{V_0} \rho_f \, dV = -\oint_S \rho_f \vec{u} \cdot d\vec{S} \,. \tag{7-2}$$

The expression on the right-hand side of 7-2 can be converted into a volume integral via Green's theorem, and after collecting terms, has the following form:

$$\int_{V_0} \left[\frac{\partial \rho_f}{\partial t} + \nabla \cdot \left(\rho_f \vec{u}\right)\right] dV = 0 \,. \tag{7-3}$$

Since V_0 is arbitrary the integrand of 7-3 must be identically zero everywhere, therefore

$$\frac{\partial \rho_f}{\partial t} + \rho_f \nabla \cdot \vec{u} + \vec{u} \cdot \nabla \rho_f = 0 \,. \tag{7-4}$$

Equation 7-4 is the continuity equation for fluid mechanics. Importantly, since this discussion is restricted to incompressible fluids ($\rho_f = \text{constant}$), the continuity equation can be greatly simplified to

$$\nabla \cdot \vec{u} = 0\,. \tag{7-5}$$

To determine fluid motion in response to a stimulus, such as a pressure field, an equation of motion is needed. Starting from Newton's second law, $m\vec{a} = \sum F_i$, we explicitly list the forces considered and use the chain rule to expand the acceleration in terms of the velocity. For an infinitesimal volume element, this becomes

$$\rho_f \left[\frac{\partial \vec{u}}{\partial t} + (\vec{u} \cdot \nabla)\vec{u}\right] = \mathrm{f}_{\mathrm{pressure}} + \mathrm{f}_{\mathrm{dissipative}}\,, \tag{7-6}$$

where, f denotes the force density acting on each fluid element. The first term on the right-hand side, $\mathrm{f}_{\mathrm{pressure}}$, describes the response of the fluid element to a pressure differential. For any finite volume element $F_{\mathrm{pressure}} = -\oint_S P\, dS = -\int_{V_0} \nabla P\, dV$ and thus $\mathrm{f}_{\mathrm{pressure}} = \nabla P$.

The second term, $\mathrm{f}_{\mathrm{dissipative}}$, describes the frictional losses which occur due to the local velocity gradient, i.e. the friction between fluid elements. Therefore, the dissipative effects depend on the spatial derivatives of the velocity and can be represented by a tensor, χ, known as the viscous stress tensor. For a Newtonian fluid, the stresses are linearly related to the first derivative of the velocity. Additionally, χ can have no terms that are independent of the velocity gradient, and, for an incompressible fluid, derivatives of the form $\partial_{x_i} u_i$ cannot be present. The most general tensor of rank 2 satisfying these conditions is

$$\chi_{ik} = \eta\left(\frac{\partial u_i}{\partial x_k} + \frac{\partial u_k}{\partial x_i}\right), \tag{7-7}$$

where the proportionality constant η is known as the viscosity of the fluid. The force associated with these effects is given by

$$\mathrm{f}_{\mathrm{dissipative}} = \frac{\partial \chi_{ik}}{\partial x_k} = \eta \nabla^2 u\,. \tag{7-8}$$

Thus, the equation of motion for our fluid is

$$\frac{\partial \vec{u}}{\partial t} + (\vec{u} \cdot \nabla)\vec{u} = \frac{1}{\rho_f}\left[-\nabla P + \eta \nabla^2 \vec{u}\right]. \tag{7-9}$$

The above equation is known as the Navier-Stokes equation, and together with the continuity equation (7-5), it can be used to determine the flow of viscous fluids. In many instances, the Navier-Stokes equation can be considerably

simplified. First, if *steady* flows are considered, i.e. the flow profile is constant with respect to time, then $\partial\vec{u}/\partial t = 0$. Second, if the flow speed is low enough such that inertial effects can be neglected, then $(\vec{u}\cdot\nabla)\vec{u} \approx 0$. This regime is referred to as "Laminar flow." To determine the flow speed that is "low enough" to permit the Laminar approximation, we note that for fluid moving past a distance L the time scale associated with the term $(\vec{u}\cdot\nabla)\vec{u}$ scales as $\sim u^2/\mathrm{L}$ while the term $\eta\nabla^2\vec{u}/\rho_f$ scales as $\sim\eta u/\rho_f L^2$. The ratio of these two time-scales is known as the Reynolds number, i.e.

$$\mathrm{Re\#} = \frac{\rho_f u L}{\eta}\,. \qquad 7\text{-}10$$

For low Reynolds numbers, the flow is laminar and thus dominated by the viscous effect, whereas at high Reynolds numbers, the flow profile tends to be dictated by inertial effects. The threshold for "low" vs "high" Reynolds numbers varies for different situations/geometries. For the case of a sphere moving through a fluid, a threshold of $R\# \approx 1$ is often valid.(*138*) Under the low Reynolds number approximation, the Navier-Stokes equation for steady flows is

$$\frac{1}{\rho_f}[-\nabla P + \eta\nabla^2\vec{u}] = 0\,. \qquad 7\text{-}11$$

7.2 Drag Coefficient in Laminar Flow

An important problem for this thesis is to determine the drag force acting on a sphere with a constant velocity vector ($\vec{v}$) moving through a stationary viscous fluid. This problem is identically equivalent to that of uniform fluid flow pasing a sphere that is fixed in space. We set the origin at the centre of the sphere for simplicity since all variations in fluid velocity will be relative to this point. In this frame of reference, the fluid boundary conditions are $\vec{u}|_{r=a} = 0$[77] and $\vec{u}|_{r\to\infty} = \vec{v}$ (where a is the radius of the sphere). If we let $\vec{w} = \vec{u} - \vec{v}$, i.e. the linear transformation to a coordinate frame *not* fixed to the sphere, since the continuity condition must hold for any reference frame, is

$$\nabla\cdot\vec{w} = \nabla\cdot(\vec{u}-\vec{v}) = \nabla\cdot\vec{u} = 0\,. \qquad 7\text{-}12$$

Given the above relation, the vector $\vec{w} = \vec{u} - \vec{v}$ can therefore be expressed as the curl of some vector $\vec{A}$,[78] i.e.

[77] Here we have assumed the "no-slip" condition on the surface of the sphere which is an often-used approximation for solid-liquid interfaces.

[78] Since $\nabla\cdot(\nabla\times\vec{A}) = 0 \;\forall\; \vec{A}$

$$\vec{u} - \vec{v} = \nabla \times \vec{A} \,. \tag{7-13}$$

The vector $\vec{A}$ must be linearly dependent on $\vec{v}$ since the equation of motion and all boundary conditions are linear. Additionally, due to the symmetry of the problem, there is no preferred direction other than along $\vec{v}$ and $\vec{A}$ must therefore be symmetric for all coordinate axes where $\vec{r} \cdot \vec{v} = 0$. The general form of $\vec{A}$ that satisfies all of these requirements is $\vec{A}(r) = f'(r)\hat{r} \times \vec{v} = \nabla f(r) \times \vec{v}$. This allows the equation for the fluid velocity to be expressed as

$$\vec{u} = \vec{v} + \nabla \times (\nabla f(r) \times \vec{v}) = \vec{v} + \nabla \times (\nabla \times f\vec{v}) \,. \tag{7-14}$$

Note that the last term is obtained by noting that $\vec{v}$ is a constant, as established by the problem definition. The explicit dependence of f on r has been dropped for clarity but is always implied (i.e. $f(r) \to f$).

By taking the curl of the low Reynolds number Navier-Stokes equation 7-11 we get

$$\nabla \times (\eta \nabla^2 \vec{u} - \nabla P) = \nabla^2 (\nabla \times \vec{u}) = 0 \,. \tag{7-15}$$

Meanwhile, by taking the curl of the fluid velocity equation gives

$$\begin{aligned} \nabla \times \vec{u} = \nabla \times \left(\vec{v} + \nabla \times (\nabla \times f\vec{v})\right) &= (\nabla(\nabla \cdot) - \nabla^2)(\nabla \times f\vec{v}) \\ &= -\nabla^2 (\nabla \times f\vec{v}) \,. \end{aligned} \tag{7-16}$$

Therefore, by combining equations 7-15 and 7-16, we obtain

$$\nabla^2 (\nabla \times \vec{u}) = -\nabla^4 (\nabla \times f\vec{v}) = -\left(\nabla^4 (\nabla f)\right) \times \vec{v} = 0 \,. \tag{7-17}$$

Since $\vec{v}$ is constant, it must hold that $\nabla^4(\nabla f) = 0$ and upon integration $\nabla^4 f = \mathrm{C}_0$ where C_0 is a constant. $C_0 = 0$ since $\vec{w} = \vec{u} - \vec{v}$ and its derivatives vanish as $r \to \infty$. This equation is then expanded into terms of the second derivative since this is how the velocity was defined, i.e.

$$\nabla^4 f = \frac{1}{r^2} \frac{d}{dr} \left(r^2 \frac{d}{dr} \right) \nabla^2 f = 0 \tag{7-18}$$

and

$$\nabla^2 f = \frac{2C_1}{r} + C_2 \,. \tag{7-19}$$

Again, due to the boundary condition at infinity $C_2 = 0$. Further integration yields:

$$f = C_1 r + \frac{C_3}{r}. \tag{7-20}$$

Putting f into the velocity equation yields

$$u = v - C_1 \frac{\vec{v} + \hat{r}(\vec{v}\cdot\hat{r})}{r} + C_3 \frac{3\hat{r}(\vec{v}\cdot\hat{r}) - \vec{v}}{r^3}. \tag{7-21}$$

These constant coefficients can now be determined by applying the no-slip boundary condition, $\vec{u}|_{r=a} = 0$, i.e.

$$-\vec{v}\left(1 - \frac{C_1}{a} - \frac{C_3}{a^3}\right) + \hat{r}(\vec{v}\cdot\hat{r})\left(-\frac{C_1}{a} + \frac{3C_3}{a^3}\right) = 0\,, \tag{7-22}$$

Thus the coefficients are $C_1 = \frac{3}{4}a$ and $C_3 = \frac{1}{4}a^3$. Finally, solving for the velocity:

$$f = \frac{3}{r}ar + \frac{a^3}{4r} \tag{7-23}$$

$$\vec{u} = -\frac{3}{4}a\left(\frac{\vec{v} + \hat{r}(\vec{v}\cdot\hat{r})}{r}\right) - \frac{1}{4}a^3\frac{\vec{v} - 3\hat{r}(\vec{v}\cdot\hat{r})}{r^3} + \vec{v} \tag{7-24}$$

Equation 7-24 can be expressed in spherical polar coordinates, with the symmetry axis parallel to $\vec{v}$ as

$$u_r = v\cos\theta\left[1 - \frac{3a}{2r} + \frac{a^3}{2r^3}\right] \tag{7-25}$$

and

$$u_\theta = -v\sin\theta\left[1 - \frac{3a}{4r} - \frac{a^3}{4r^3}\right]. \tag{7-26}$$

Now, using the Navier-Stokes equation (7-11), the pressure can be determined as

$$\nabla P = \eta\nabla^2\vec{u} = \eta\nabla^2(\nabla\times\nabla\times f\vec{v}) = \eta\nabla^2(\nabla(\nabla\cdot f\vec{v}) - \vec{v}\nabla^2 f)\,. \tag{7-27}$$

And since $\nabla^4 f = 0$ we have

$$\nabla P = \nabla[\eta\nabla^2(\nabla\cdot f\vec{v})] = \nabla\big(\eta\vec{v}\cdot\nabla(\nabla^2 f)\big) \tag{7-28}$$

and

$$P = \eta\vec{v}\cdot\nabla(\nabla^2 f) + P_0\,, \tag{7-29}$$

where P_0 is the ambient pressure. Using the definition of f obtained above results in

$$P = P_0 - \frac{3}{2}\eta\frac{\vec{v}\cdot\hat{r}}{r^2}a\,. \tag{7-30}$$

To obtain the force acting upon the sphere, we must integrate the stresses over the surface (due to pressure and viscous friction), i.e.

$$F_{\text{drag}} = \oint_S (-P\cos\theta + \chi_{rr}\cos\theta + \chi_{r\theta}\sin\theta)\,dS \tag{7-31}$$

with[79]

$$\chi_{rr} = 2\eta\frac{\partial u_r}{\partial r}, \quad \text{and} \quad \chi_{r\theta} = \eta\left(\frac{1}{r}\frac{\partial u_r}{\partial\theta} + \frac{\partial u_\theta}{\partial r} - \frac{u_\theta}{r}\right). \tag{7-32}$$

Therefore, at the surface of the sphere

$$\chi_{rr}|_{r=a} = 0\,, \quad \chi_{r\theta}|_{r=a} = -\frac{3\eta}{2a}\vec{v}\sin\theta\,, \tag{7-33}$$

and

$$P|_{r=a} = P_0 - \frac{3\eta}{2a}\vec{v}\cos\theta \tag{7-34}$$

resulting in[80]

$$F_{\text{drag}} = -\frac{3\eta\vec{v}}{2a}\oint_S dS = \frac{3\eta\vec{v}}{2a}\cdot 4\pi a^2 \tag{7-35}$$

$$F_{\text{drag}} = -6\pi\eta a\vec{v}\,. \tag{7-36}$$

This last equation (7-36) is the well-known Stokes drag with the factor $\gamma_0 = 6\pi\eta a$ as the Stokes drag coefficient.

[79] Note that here the viscous stress tensor is being represented in cylindrical coordinates.
[80] Note that the ambient pressure, P_0, disappears from the integration over the sphere because it is a constant along the surface.

Frequency-dependent viscous drag:

The Stokes drag derived above (equation 7-36) is only valid for constant rectilinear motion at moderate velocities. A more general equation for the viscous drag force acting on a sphere is known as the Basset force:(*139*, *140*)

$$F_{\text{Basset}}(t) = -\left[\frac{m_f}{2}\frac{d\vec{v}(t)}{dt} + \gamma_0\left(\vec{v}(t) + \sqrt{\frac{\tau_f}{\pi}}\int_{-\infty}^{t}\frac{d\vec{v}(t)}{dt}\frac{1}{\sqrt{t-t'}}dt'\right)\right]. \quad 7\text{-}37$$

Here m_f is the mass of the fluid displaced by the particle and τ_f is the fluid relaxation time over the radius of the particle. This incorporates the fact that the past motion of the particle caused the surrounding fluid to move, which affects the current velocity gradients and, therefore, the viscous stresses. For the analogous problem of simple oscillatory motion at a constant frequency ω, a frequency-dependent drag coefficient can be obtained given by(*46*)

$$\gamma(\omega) = \gamma_0\left(1 + \delta + \frac{\delta^2}{9}\right) \quad 7\text{-}38$$

with $\delta = \sqrt{-i\omega\tau_f}$ where $\tau_f \approx a^2\rho_f/\eta$ and ρ_f is the fluid density. It can be shown that the Basset force can be obtained from the frequency-dependent drag coefficient by a suitable Laplace transformation. The advantage of equation 7-38 is that multiplication in the frequency domain is often easier than convolution in the time domain for many situations. Both equations 7-37 and 7-38 are still only valid for laminar flow.

In practice, the Stokes drag coefficient (i.e. the low-frequency approximation) is often sufficient for many applications since the fluid relaxation time is on the order of $\tau_f \approx 1$ µs for microspheres in water. Thus equation 7-38 does not deviate significantly from the Stokes drag for moderate oscillation frequencies as shown in Figure 37.

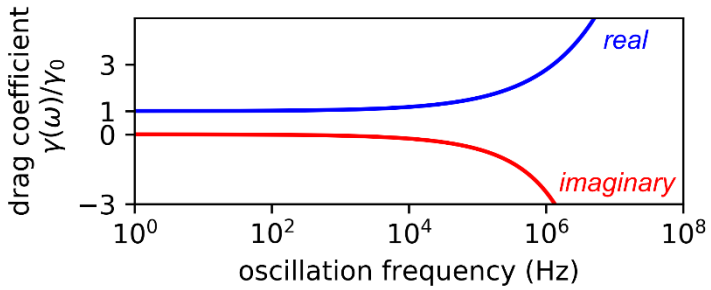

Figure 37 Frequency-dependent drag coefficient for a microsphere ($a = 1$ µm) in water.

7.2.1 Boundary Effects

The results obtained above are only valid for a sphere in a homogeneous medium. The presence of a boundary can cause a significant perturbation to these results that are often important for many practical applications. In particular, an infinite planar interface near the sphere (which is also subject to the no-slip boundary condition) results in an increased drag force as well as breaking the symmetry of the situation. First-order correction factors were originally derived by Lorentz in 1907 for the drag coefficient parallel and perpendicular to an infinite no-slip interface, i.e.(*141*, *142*)

$$\gamma_{\parallel} = \left(1 + \frac{9}{8}\frac{a}{h}\right)\gamma_0 \quad \text{and} \quad \gamma_{\perp} = \left(1 + \frac{9}{18}\frac{a}{h}\right)\gamma_0 \,, \tag{7-39}$$

where h is the distance from the centre of the sphere to the interface. The above approximation is generally valid for $a/h \gg 1$ but becomes unreliable at short distances. Higher-order terms for the parallel drag coefficient were obtained by Faxén, and the drag coefficient is often approximated as(*143*, *144*)

$$\gamma_{\parallel} = \left(1 - \frac{9}{8}\left(\frac{a}{2h}\right) + \left(\frac{a}{2h}\right)^3 - \frac{45}{16}\left(\frac{a}{2h}\right)^4 - 2\left(\frac{a}{2h}\right)^5\right)^{-1}\gamma_0 \,. \tag{7-40}$$

Approximations for the perpendicular drag coefficient are generally more mathematically complex such as:(*145*)

$$\gamma_{\perp} = \left(\frac{4}{3}\sinh\beta \sum_{n=1}^{\infty}\left[\frac{n(n+1)}{(2n-1)(2n+3)} \cdot \left(\frac{2\sinh\big((2n+1)\beta\big) + (2n+1)\sinh 2\beta}{4\sinh^2\big((n+.5)\beta\big) - (2n+1)\sinh^2\beta} - 1\right)\right]\right)\gamma_0 \tag{7-41}$$

with $\beta = \cosh^{-1}(h/a)$. Both equations 7-40 and 7-41 have been experimentally verified to hold down to small displacements of the sphere from an interface.(*146*)

Frequency-dependent boundary effects

As with the case for the homogeneous drag coefficient, the hydrodynamic effect of harmonic oscillations near a no-slip interface has also been investigated. Provided below are two such approximations for the frequency-dependent parallel and perpendicular drag correction factors for a spherical particle near a no-slip interface:(*147*, *148*)

$$\chi_{\parallel}^{\omega} = -\frac{1}{32\xi^4}\frac{a}{h}\big[36 + 27\xi + 6\xi^2 + 6(6 + 12\xi + 11\xi^2 + 6\xi^3 + 4\xi^4)e^{-2\xi} - (144 + 144\xi + 72\xi^2 + 24\xi^3 - 6\xi^4 + 2\xi^5 - \xi^6 + \xi^7)e^{-\xi} + \xi^8 E_1(\xi) + 12\xi^3\big(2\xi K_2(2\xi) + 3K_3(2\xi)\big) + 6\pi\xi^3\big\{2\xi\big(Y_2(2\xi) - H_{-2}(2\xi)\big) - 2\big(Y_3(2\xi) + H_{-3}(2\xi)\big)\big\}\big] \quad 7\text{-}42$$

$$\chi_{\perp}^{\omega} = -\frac{1}{16\xi^4}\frac{a}{h}\big[6(6 + \xi^2 + 8\xi^3) + 6(6 + 12\xi + 9\xi^2 + 2\xi^3)e^{-2\xi} - (144 + 144\xi + 48\xi^2 - 6\xi^4 + 10\xi^5 + \xi^6 - \xi^7)e^{-\xi} + \xi^6(12 - \xi^2)E_1(\xi) + 72\,\xi^2 K_0(2\xi) + 36\xi(2 + \xi^2)K_1(2\xi) + 6\pi\xi\big\{2\xi(2 - \xi^2)\big(Y_0(2\xi) - H_0(2\xi)\big) - (6 - 5\xi^2)\big(Y_1(2\xi) - H_1(2\xi)\big)\big\}\big] \quad 7\text{-}43$$

where E_1 is the exponential integral; H_n, Y_n, and K_n are the Struve function, Bessel function of the second kind, and modified Bessel function of the second kind (order n). $\xi = \sqrt{-i\omega\tau_h}$ and τ_h is the fluid relaxation time over the separation distance. The total drag coefficient, therefore, becomes:(*142*)

$$\gamma_{\parallel,\perp}(\omega, h) = i\omega m_f + \gamma_0 \frac{1 + \delta + \delta^2/3}{1 + [1 + \delta + \delta^2/3] \cdot \chi_{\parallel,\perp}}. \quad 7\text{-}44$$

Recent reports, based on experiments and molecular dynamics simulations, have suggested that this form of the drag coefficient is suitable for explaining the behaviour of particles near an interface.(*149*, *150*)

Bibliography

1. M. Bauch, K. Toma, M. Toma, Q. Zhang, J. Dostalek, Plasmon-Enhanced Fluorescence Biosensors: A Review. *Plasmonics*. **9**, 781–799 (2014).
2. K. M. Mayer, J. H. Hafner, Localized Surface Plasmon Resonance Sensors. *Chemical Reviews*. **111**, 3828–3857 (2011).
3. T. Shoji, Y. Tsuboi, Plasmonic Optical Tweezers toward Molecular Manipulation: Tailoring Plasmonic Nanostructure, Light Source, and Resonant Trapping. *Journal of Physical Chemistry Letters*. **5**, 2957–2967 (2014).
4. J. Garcia-Guirado, R. A. Rica, J. Ortega, J. Medina, V. Sanz, E. Ruiz-Reina, R. Quidant, Overcoming Diffusion-Limited Biosensing by Electrothermoplasmonics. *ACS Photonics*. **5**, 3673–3679 (2018).
5. J. C. Ndukaife, A. v. Kildishev, A. G. A. Nnanna, V. M. Shalaev, S. T. Wereley, A. Boltasseva, Long-range and rapid transport of individual nano-objects by a hybrid electrothermoplasmonic nanotweezer. *Nature Nanotechnology*. **11**, 53–59 (2016).
6. J. C. Ndukaife, Y. Xuan, A. G. A. Nnanna, A. v. Kildishev, V. M. Shalaev, S. T. Wereley, A. Boltasseva, High-Resolution Large-Ensemble Nanoparticle Trapping with Multifunctional Thermoplasmonic Nanohole Metasurface. *ACS Nano*. **12**, 5376–5384 (2018).
7. Z. Kang, J. Chen, H.-P. Ho, Surface-enhanced Raman scattering: Via entrapment of colloidal plasmonic nanocrystals by laser generated microbubbles on random gold nano-islands. *Nanoscale*. **8**, 10266–10272 (2016).
8. C. J. Wienken, P. Baaske, U. Rothbauer, D. Braun, S. Duhr, Protein-binding assays in biological liquids using microscale thermophoresis. *Nature Communications*. **1**, 100–7 (2010).
9. S. A. I. Seidel, P. M. Dijkman, W. A. Lea, G. van den Bogaart, M. Jerabek-Willemsen, A. Lazic, J. S. Joseph, P. Srinivasan, P. Baaske, A. Simeonov, I. Katritch, F. A. Melo, J. E. Ladbury, G. Schreiber, A. Watts, D. Braun, S. Duhr, Microscale thermophoresis quantifies biomolecular interactions under previously challenging conditions. *Methods*. **59**, 301–315 (2013).
10. A. M. Gobin, M. H. Lee, N. J. Halas, W. D. James, R. A. Drezek, J. L. West, Near-Infrared Resonant Nanoshells for Combined Optical Imaging and Photothermal Cancer Therapy. *Nano Letters*. **7**, 1929–1934 (2007).
11. S. Lal, S. E. Clare, N. J. Halas, Nanoshell-Enabled Photothermal Cancer Therapy: Impending Clinical Impact. *Accounts of Chemical Research*. **41**, 1842–1851 (2008).
12. V. Giannini, A. I. Fernández-Domínguez, S. C. Heck, S. A. Maier, Plasmonic Nanoantennas: Fundamentals and Their Use in Controlling the Radiative Properties of Nanoemitters. *Chemical Reviews*. **111**, 3888–3912 (2011).
13. P. B. Johnson, R. W. Christy, Optical Constants of the Noble Metals. *Physical Review B*. **6**, 4370–4379 (1972).
14. S. Maier, *Plasmonics: Fundamentals and Applications* (Springer, New York, first edition., 2007).

15. D. Jackson, *Classical Electrodynamics* (Wiley, New York, third edition., 1999).
16. J. Stratton, *Electromagnetic Theory* (McGraw-Hill, New York, first edition., 1941).
17. C. Bohren, D. Huffman, *Absorption and Scattering of Light by Small Particles* (Wiley, New York, first edition., 1998).
18. A. O. Govorov, W. Zhang, T. Skeini, H. Richardson, J. Lee, N. A. Kotov, Gold nanoparticle ensembles as heaters and actuators: Melting and collective plasmon resonances. *Nanoscale Research Letters*. **1**, 84–90 (2006).
19. G. Baffou, R. Quidant, Thermo-plasmonics: using metallic nanostructures as nano-sources of heat. *Laser and Photonics Reviews*. **7**, 171–187 (2013).
20. A. D. Rakic´, A. B. Djurišic´, J. M. Elazar, M. L. Majewski, Optical properties of metallic films for vertical-cavity optoelectronic devices. *Applied Optics*. **37**, 5271–5283 (1998).
21. B. Sharma, R. R. Frontiera, A.-I. Henry, E. Ringe, R. P. van Duyne, SERS: Materials, applications, and the future. *Materials Today*. **15**, 16–25 (2012).
22. F. Neubrech, C. Huck, K. Weber, A. Pucci, H. Giessen, Surface-enhanced infrared spectroscopy using resonant nanoantennas. *Chemical Reviews*. **117**, 5110–5145 (2017).
23. J. R. Ferraro, K. Nakamoto, C. W. Brown, *Introductory Raman Spectroscopy* (Academic Press Inc., London, second edition., 2003).
24. P. L. Stiles, J. A. Dieringer, N. C. Shah, R. P. van Duyne, Surface-Enhanced Raman Spectroscopy. *Annual Review of Analytical Chemistry*. **1**, 601–626 (2008).
25. E. C. le Ru, E. Blackie, M. Meyer, P. G. Etchegoin, Surface Enhanced Raman Scattering Enhancement Factors: A Comprehensive Study. *Journal of Physical Chemistry C*. **111**, 13794–13803 (2007).
26. H. X. Xu, E. J. Bjerneld, M. Käll, L. Börjesson, Spectroscopy of single hemoglobin molecules by surface enhanced Raman scattering. *Phys. Rev. Lett.* **83**, 4357–4360 (1999).
27. E. C. le Ru, P. G. Etchegoin, Single-Molecule Surface-Enhanced Raman Spectroscopy. *Annual Review of Physical Chemistry*. **63**, 65–87 (2012).
28. S. S. Aćimović, H. Šípová-Jungová, G. Emilsson, L. Shao, A. B. Dahlin, M. Käll, T. J. Antosiewicz, Antibody−antigen interaction dynamics revealed by analysis of single-molecule equilibrium fluctuations on individual plasmonic nanoparticle biosensors. *ACS Nano*. **12**, 9958–9965 (2018).
29. K. M. Mayer, F. Hao, S. Lee, P. Nordlander, J. H. Hafner, A single molecule immunoassay by localized surface plasmon resonance. *Nanotechnology*. **21**, 255503–8 (2010).
30. S. Chen, M. Svedendahl, R. P. V. Duyne, M. Käll, Plasmon-enhanced colorimetric ELISA with single molecule sensitivity. *Nano Letters*. **11**, 1826–1830 (2011).
31. A. Ashkin, Acceleration and Trapping of Particles by Radiation Pressure. *Physical Review Letters*. **24**, 156–159 (1970).

32. A. Ashkin, J. M. Dziedzic, J. E. Bjorkholm, S. Chu, Observation of a single-beam gradient force optical trap for dielectric particles. *Optics Letters*. **11**, 288–290 (1986).
33. P. H. Jones, O. M. Marago, G. Volpe, *Optical Tweezers Principles and Applications* (Cambridge University Press, Cambridge, first edition., 2015).
34. M. Kerker, *The Scattering of Light and Other Electromagnetic Radiation* (Academic Press Inc., New York, first edition., 1969).
35. Y. Harada, T. Asakura, Radiation forces on a dielectric sphere in the Rayleigh scattering regime. *Optics Communications*. **124**, 529–541 (1996).
36. J. P. Gordon, Radiation Forces and Momenta in Dielectric Media. *Physical Review A*. **8**, 14–21 (1973).
37. D. Griffiths, R. College, *Introduction to electrodynamics* (Cambridge University Press, Cambridge, fourth edition., 1999).
38. A. Salazar, On thermal diffusivity. *European Journal of Physics*. **24**, 351–358 (2003).
39. A. Karbalaei, R. Kumar, H. J. Cho, Thermocapillarity in microfluidics-A review. *Micromachines*. **7**, 1–41 (2016).
40. G. Baffou, R. Quidant, C. Girard, Thermoplasmonics modeling: A Green's function approach. *Physical Review B*. **82**, 165424–11 (2010).
41. G. Baffou, H. Rigneault, Femtosecond-pulsed optical heating of gold nanoparticles. *Physical Review B*. **84**, 035415–13 (2011).
42. G. Baffou, *Thermoplasmonics* (Cambridge University Press, Cambridge, first edition., 2018).
43. P. Berto, M. Mohamed, H. Rigneault, G. Baffou, Time-harmonic optical heating of plasmonic nanoparticles. *Physical Review B*. **90**, 035439–12 (2014).
44. S. Jones, D. Andrén, T. J. Antosiewicz, M. Käll, Ultrafast Modulation of Thermoplasmonic Nanobubbles in Water. *Nano Letters*. **19**, 8294–8302 (2019).
45. J. S. Donner, G. Baffou, D. McCloskey, R. Quidant, Plasmon-Assisted Optofluidics. *ACS Nano*, 5457–5462 (2011).
46. L. D. Landau, E. M. Lifshitz, *Fluid Mechanics* (Pergamom Press, Oxford, second edition., 1987).
47. Y. A. Cengel, *Heat transfer: a practical approach* (McGraw-Hill, Boston, second edition., 2003).
48. J. Lombard, T. Biben, S. Merabia, Nanobubbles around plasmonic nanoparticles: Thermodynamic analysis. *Physical Review E*. **91**, 043007–18 (2015).
49. X. Li, Y. Wang, M. E. Zaytsev, G. Lajoinie, H. le The, J. G. Bomer, J. C. T. Eijkel, H. J. W. Zandvliet, X. Zhang, D. Lohse, Plasmonic Bubble Nucleation and Growth in Water: Effect of Dissolved Air. *Journal of Physical Chemistry C*. **123**, 23586–23593 (2019).
50. G. Baffou, J. Polleux, H. Rigneault, S. Monneret, Super-Heating and Micro-Bubble Generation around Plasmonic Nanoparticles under CW Illumination. *Journal of Physical Chemistry C*. **118**, 4890–4898 (2014).
51. Y. Wang, M. E. Zaytsev, G. Lajoinie, H. Le-The, J. C. T. Eijkel, A. van den Berg, M. Versluis, B. M. Weckhuysen, X. Zhang, H. J. W. Zandvliet, D. Lohse, Giant and explosive plasmonic bubbles by delayed nucleation. *PNAS*. **115**, 7676–7681 (2018).

52. Y. Wang, M. E. Zaytsev, H. le The, J. C. T. Eijkel, H. J. W. Zandvliet, X. Zhang, D. Lohse, Vapor and Gas-Bubble Growth Dynamics around Laser-Irradiated, Water-Immersed Plasmonic Nanoparticles. *ACS Nano*. **11**, 2045–2051 (2017).
53. M. E. Zaytsev, G. Lajoinie, Y. Wang, D. Lohse, H. J. W. Zandvliet, X. Zhang, Plasmonic Bubbles in n-Alkanes. *Journal of Physical Chemistry C*. **122**, 28375–28381 (2018).
54. X. Liu, L. Bao, M. Dipalo, F. de Angelis, X. Zhang, Formation and dissolution of microbubbles on highly-ordered plasmonic nanopillar arrays. *Scientific Reports*. **5**, 18515–9 (2015).
55. S. Deguchi, S. Takahashi, H. Hiraki, S. Tanimura, Direct measurement of force exerted during single microbubble generation. *Applied Physics Letters*. **102**, 084101–5 (2013).
56. K. Namura, K. Nakajima, M. Suzuki, Quasi-stokeslet induced by thermoplasmonic Marangoni effect around a water vapor microbubble. *Scientific Reports*. **7**, 45776–8 (2017).
57. M. E. Zaytsev, Y. Wang, Y. Zhang, G. Lajoinie, X. Zhang, A. Prosperetti, H. J. W. Zandvliet, D. Lohse, Gas-vapor Interplay in Plasmonic Bubble Shrinkage. *The Journal of Physical Chemistry C*. **124**, 5861–5869 (2020).
58. P. S. Epstein, M. S. Plesset, On the Stability of Gas Bubbles in Liquid-Gas solutions. *The Journal of Chemical Physics*. **18**, 1505–1509 (1950).
59. S. Ljunggren, J. C. Eriksson, The lifetime of a colloid-sized gas bubble in water and the cause of the hydrophobic attraction. *Colloids and Surfaces A: Physicochemical and Engineering Aspects*. **129–130**, 151–155 (1997).
60. R. Brown, A brief account of microscopical observations made in the months of June, July and August 1827, on the particles contained in the pollen of plants; and on the general existence of active molecules in organic and inorganic bodies. *The Philosophical Magazine*. **4**, 161–173 (1828).
61. A. Einstein, Über die von der molekularkinetischen Theorie der Wärme geforderte Bewegung von in ruhenden Flüssigkeiten suspendierten Teilchen. *annalen der physik*. **322**, 549–560 (1905).
62. A. Einstein, A. D. Cowper, Investigations on the theory of the Brownian movement [English translation] (1956).
63. D. Selmeczi, S. F. Tolić-Nørrelykke, E. Schäffer, P. H. Hagedorn, S. Mosler, K. Berg-Sørensen, N. B. Larsen, H. Flyvbjerg, Brownian motion after Einstein and Smoluchowski: some new applications and experiments. *ACTA Physica Polonica B*. **38**, 2407–2431 (2007).
64. R. Piazza, Thermophoresis: moving particles with thermal gradients. *Soft Matter*. **4**, 1740–1744 (2008).
65. S. A. Putnam, D. G. Cahill, Transport of nanoscale latex spheres in a temperature gradient. *Langmuir*. **21**, 5317–5323 (2005).
66. S. Duhr, D. Braun, Thermophoretic depletion follows Boltzmann distribution. *Physical Review Letters*. **96**, 168301–4 (2006).
67. A. Würger, Hydrodynamic Boundary Effects on Thermophoresis of Confined Colloids. *Physical Review Letters*. **116**, 138302–5 (2016).
68. S. A. Putnam, D. G. Cahill, G. C. L. Wong, Temperature dependence of thermodiffusion in aqueous suspensions of charged nanoparticles. *Langmuir*. **23**, 9221–9228 (2007).

69. M. Braibanti, D. Vigolo, R. Piazza, Does thermophoretic mobility depend on particle size? *Physical Review Letters*. **100**, 108303–4 (2008).
70. S. Iacopini, R. Piazza, Thermophoresis in protein solutions. *Europhysics Letters*. **63**, 247–253 (2003).
71. A. Würger, Thermal non-equilibrium transport in colloids. *Reports on Progress in Physics*. **73**, 126601–35 (2010).
72. S. Iacopini, R. Rusconi, R. Piazza, The "macromolecular tourist": Universal temperature dependence of thermal diffusion in aqueous colloidal suspensions. *European Physical Journal E*. **19**, 59–67 (2006).
73. M. Jerabek-Willemsen, C. J. Wienken, D. Braun, P. Baaske, S. Duhr, Molecular Interaction Studies Using Microscale Thermophoresis. *ASSAY and Drug Development Technologies*. **9**, 342–353 (2011).
74. M. Braun, A. P. Bregulla, K. Günther, M. Mertig, F. Cichos, Single Molecules Trapped by Dynamic Inhomogeneous Temperature Fields. *Nano Letters*. **15**, 5499–5505 (2015).
75. M. Braun, F. Cichos, Optically Controlled Thermophoretic Trapping of Single Nano-Objects. *ACS Nano*. **7**, 11200–11208 (2013).
76. L. Lin, M. Wang, X. Peng, E. N. Lissek, Z. Mao, L. Scarabelli, E. Adkins, S. Coskun, H. E. Unalan, B. A. Korgel, L. M. Liz-Marzán, E. L. Florin, Y. Zheng, Opto-thermoelectric nanotweezers. *Nature Photonics*. **12**, 195–201 (2018).
77. L. Lin, X. Peng, Z. Mao, X. Wei, C. Xie, Y. Zheng, Interfacial-entropy-driven thermophoretic tweezers. *Lab on a Chip*. **17**, 3061–3070 (2017).
78. H. Šípová-Jungová, D. Andrén, S. Jones, M. Käll, Nanoscale Inorganic Motors Driven by Light: Principles, Realizations, and Opportunities. *Chemical Reviews*. **120**, 269–287 (2020).
79. K. Kroy, D. Chakraborty, F. Cichos, Hot microswimmers. *European Physical Journal: Special Topics*. **225**, 2207–2225 (2016).
80. A. P. Bregulla, H. Yang, F. Cichos, Stochastic localization of microswimmers by photon nudging. *ACS Nano*. **8**, 6542–6550 (2014).
81. L. Baraban, R. Streubel, D. Makarov, L. Han, D. Karnaushenko, O. G. Schmidt, G. Cuniberti, Fuel-free locomotion of janus motors: Magnetically induced thermophoresis. *ACS Nano*. **7**, 1360–1367 (2013).
82. C. M. Maier, M. A. Huergo, S. Milosevic, C. Pernpeintner, M. Li, D. P. Singh, D. Walker, P. Fischer, J. Feldmann, T. Lohmüller, Optical and Thermophoretic Control of Janus Nanopen Injection into Living Cells. *Nano Letters*. **18**, 7935–7941 (2018).
83. S. Nedev, S. Carretero-Palacios, P. Kühler, T. Lohmüller, A. S. Urban, L. J. E. Anderson, J. Feldmann, An optically controlled microscale elevator using plasmonic janus particles. *ACS Photonics*. **2**, 491–496 (2015).
84. T. M. Squires, R. J. Messinger, S. R. Manalis, Making it stick: Convection, reaction and diffusion in surface-based biosensors. *Nature Biotechnology*. **26**, 417–426 (2008).
85. P. E. Sheehan, L. J. Whitman, Detection limits for nanoscale biosensors. *Nano Letters*. **5**, 803–807 (2005).
86. J. R. Blake, A note on the image system for a stokeslet in a no-slip boundary. *Mathematical Proceedings of the Cambridge Philosophical Society*. **70**, 303–310 (1971).

87. J. R. Blake, A. T. Chwang, Fundamental singularities of viscous flow. Part I: The image systems in the vicinity of a stationary no-slip boundary. *Journal of Engineering Mathematics*. **8**, 23–29 (1974).
88. N. Liron, S. Mochon, Stokes flow for a stokeslet between two parallel flat plates. *Journal of Engineering Mathematics*. **10**, 287–303 (1976).
89. W. Akemann, A. Otto, Continuous secondary light emission from silver films: on the origin of the inelastic background in SERS. *Surface Science*. **307–309**, 1071–1075 (1994).
90. P. Apell, R. Monreal, S. Lundqvist, Photoluminescence of noble metals. *Physica Scripta*. **38**, 174–179 (1988).
91. K. Lin, J. Yi, J. Zhong, S. Hu, B. Liu, J. Liu, C. Zong, Z. Lei, B. Ren, X. Wang, J. Aizpurua, Plasmonic photoluminescence for recovering native chemical information from surface-enhanced Raman scattering. *Nature Communications*. **8**, 1489–9 (2017).
92. Z. Ma, Y. Yu, S. Shen, H. Dai, L. Yao, Y. Han, X. Wang, J. B. Han, L. Li, Origin of the Avalanche-Like Photoluminescence from Metallic Nanowires. *Scientific Reports*. **6**, 18857–9 (2016).
93. T. Haug, P. Klemm, S. Bange, J. M. Lupton, Hot-Electron Intraband Luminescence from Single Hot Spots in Noble-Metal Nanoparticle Films. *Physical Review Letters*. **115**, 067403–5 (2015).
94. Y. Y. Cai, E. Sung, R. Zhang, L. J. Tauzin, J. G. Liu, B. Ostovar, Y. Zhang, W. S. Chang, P. Nordlander, S. Link, Anti-stokes emission from hot carriers in gold nanorods. *Nano Letters*. **19**, 1067–1073 (2019).
95. B. Ostovar, Y.-Y. Cai, L. J. Tauzin, S. A. Lee, A. Ahmadivand, R. Zhang, P. Nordlander, S. Link, *ACS Nano*, in press, doi:10.1021/acsnano.0c06771.
96. K. Ikeda, S. Suzuki, K. Uosaki, Enhancement of SERS background through charge transfer resonances on single crystal gold surfaces of various orientations. *Journal of the American Chemical Society*. **135**, 17387–17392 (2013).
97. J. T. Hugall, J. J. Baumberg, Demonstrating Photoluminescence from Au is Electronic Inelastic Light Scattering of a Plasmonic Metal: The Origin of SERS Backgrounds. *Nano Letters*. **15**, 2600–2604 (2015).
98. A. Otto, J. Timper, J. Billmann, G. Kovacs, I. Pockrand, Surface roughness induced electronic raman scattering. *Surface Science*. **92**, 55–57 (1980).
99. H. Portales, E. Duval, L. Saviot, M. Fujii, M. Sumitomo, S. Hayashi, Raman scattering by electron-hole excitations in silver nanocrystals. *Physical Review B*. **63**, 233402–4 (2001).
100. S. M. Barnett, N. Harris, J. J. Baumberg, Molecules in the mirror: How SERS backgrounds arise from the quantum method of images. *Physical Chemistry Chemical Physics*. **16**, 6544–6549 (2014).
101. X. Xie, D. G. Cahill, Thermometry of plasmonic nanostructures by anti-Stokes electronic Raman scattering. *Applied Physics Letters*. **109**, 183104–5 (2016).
102. A. Carattino, M. Caldarola, M. Orrit, Gold nanoparticles as absolute nano-thermometers. *Nano Letters*. **18**, 874–880 (2017).
103. P. M. Goodwin, W. P. Ambrose, J. C. Martin, R. a Keller, Spatial dependence of the optical collection efficiency in flow cytometry. *Cytometry*. **21**, 133–44 (1995).

104. J. Enderlein, W. P. Ambrose, Optical collection efficiency function in single-molecule detection experiments. *Applied optics*. **36**, 5298–302 (1997).
105. A. Ashkin, J. M. Dziedzic, Optical levitation by radiation pressure. *Applied Physics Letters*. **19**, 283–285 (1971).
106. A. Ashkin, J. M. Dziedzic, T. Yamane, Optical trapping and manipulation of single cells using infrared laser beams. *Nature*. **330**, 769–771 (1987).
107. L. P. Ghislain, N. A. Switz, W. W. Webb, Measurement of small forces using an optical trap. *Review of Scientific Instruments*. **65**, 2762–2768 (1994).
108. R. M. Simmons, J. T. Finer, S. Chu, J. A. Spudich, Quantitative Measurements of Force and Displacement Using an Optical Trap. *Biophysical Journal*. **70**, 1813–1822 (1996).
109. K. Sasaki, M. Koshioka, H. Misawa, N. Kitamura, H. Masuhara, Pattern formation and flow control of fine particles by laser-scanning micromanipulation. *Optics Letters*. **16**, 1463–1465 (1991).
110. K. Visscher, G. J. Brakenhoff, J. J. Krol, Micromanipulation by "Multiple" Optical Traps Created by a Single Fast Scanning Trap Integrated With the Bilateral Confocal Scanning Laser Microscope. *Cytometry*. **14**, 105–114 (1993).
111. K. Visscher, S. P. Gross, S. M. Block, Construction of Multiple-Beam Optical Traps with Nanometer-Resolution Position Sensing. *IEEE Journal of Selected Topics in Quantum Electronics*. **2**, 1066–1076 (1996).
112. J. Liesener, M. Reicherter, T. Haist, H. J. Tiziani, Multi-functional optical tweezers using computer-generated holograms. *Optics Communications*. **185**, 77–82 (2000).
113. J. E. Curtis, B. A. Koss, D. G. Grier, Dynamic holographic optical tweezers. *Optics Communications*. **207**, 169–175 (2002).
114. K. Berg-Sørensen, H. Flyvbjerg, Power spectrum analysis for optical tweezers. *Review of Scientific Instruments*. **75**, 594–612 (2004).
115. M. L. Juan, R. Gordon, Y. Pang, F. Eftekhari, R. Quidant, Self-induced back-action optical trapping of dielectric nanoparticles. *Nature Physics*. **5**, 915–919 (2009).
116. X. Haitian, S. Jones, B.-C. Choi, R. Gordon, Characterization of Individual Magnetic Nanoparticles in Solution by Double Nanohole Optical Tweezers. *Nano Letters*. **16**, 2639–2643 (2016).
117. S. Jones, D. Andrén, P. Karpinski, M. Käll, Photothermal Heating of Plasmonic Nanoantennas: Influence on Trapped Particle Dynamics and Colloid Distribution. *ACS Photonics*. **5**, 2878–2887 (2018).
118. S. Jones, A. A. al Balushi, R. Gordon, Raman spectroscopy of single nanoparticles in a double-nanohole optical tweezer system. *Journal of Optics*. **17**, 102001–5 (2015).
119. K. Zhang, A. Jian, X. Zhang, Y. Wang, Z. Li, H. Tam, Laser-induced thermal bubbles for microfluidic applications. *Lab on a chip*. **11**, 1389–1395 (2011).
120. H. Kim, H. Bai, Z. Zhang, A. Kusimo, M. Yu, Optofluidic microvalve-on-a-chip with a surface plasmon-enhanced fiber optic microheater. *Biomicrofluidics*. **8**, 054126–10 (2014).

121. K. Namura, K. Nakajima, K. Kimura, M. Suzuki, Photothermally controlled Marangoni flow around a micro bubble. *Applied Physics Letters*. **106**, 043101–5 (2015).
122. K. Setoura, S. Ito, H. Miyasaka, Stationary bubble formation and Marangoni convection induced by CW laser heating of a single gold nanoparticle. *Nanoscale*. **9**, 719–730 (2017).
123. K. Namura, K. Nakajima, K. Kimura, M. Suzuki, Sheathless particle focusing in a microfluidic chamber by using the thermoplasmonic Marangoni effect. *Applied Physics Letters*. **108**, 071603–4 (2016).
124. K. Namura, K. Nakajima, M. Suzuki, Investigation of transition from thermal- to solutal-Marangoni flow in dilute alcohol/water mixtures using nano-plasmonic heaters. *Nanotechnology*. **29**, 065201–7 (2018).
125. Y. Zheng, H. Liu, Y. Wang, C. Zhu, S. Wang, J. Cao, S. Zhu, Accumulating microparticles and direct-writing micropatterns using a continuous-wave laser-induced vapor bubble. *Lab on a chip*. **11**, 3816–3820 (2011).
126. L. Lin, X. Peng, Z. Mao, W. Li, M. N. Yogeesh, B. B. Rajeeva, E. P. Perillo, A. K. Dunn, D. Akinwande, Y. Zheng, Bubble-Pen Lithography. *Nano Letters*. **16**, 701–708 (2016).
127. K. Setoura, Y. Okada, S. Hashimoto, CW-laser-induced morphological changes of a single gold nanoparticle on glass: Observation of surface evaporation. *Physical Chemistry Chemical Physics*. **16**, 26938–26945 (2014).
128. L. Hou, M. Yorulmaz, N. R. Verhart, M. Orrit, Explosive formation and dynamics of vapor nanobubbles around a continuously heated gold nanosphere. *New Journal of Physics*. **17**, 013050–9 (2015).
129. S. Kerman, C. Chen, Y. Li, W. van Roy, L. Lagae, P. van Dorpe, Raman Fingerprinting of Single Dielectric Nanoparticles in Plasmonic Nanopores. *Nanoscale*. **7**, 18612–18618 (2015).
130. G. Baffou, R. Quidant, F. J. García De Abajo, Nanoscale control of optical heating in complex plasmonic systems. *ACS Nano*. **4**, 709–716 (2010).
131. G. Baffou, E. B. Ureña, P. Berto, S. Monneret, R. Quidant, H. Rigneault, Deterministic temperature shaping using plasmonic nanoparticle assemblies. *Nanoscale*. **6**, 8984–8989 (2014).
132. F. Karim, E. S. Vasquez, Y. Sun, C. Zhao, Optothermal microbubble assisted manufacturing of nanogap-rich structures for active chemical sensing. *Nanoscale*. **11**, 20589–20597 (2019).
133. Y. Kim, H. Ding, Y. Zheng, Enhancing Surface Capture and Sensing of Proteins with Low-Power Optothermal Bubbles in a Biphasic Liquid. *Nano Letters*. **20**, 7020–7027 (2020).
134. Y. Yamamoto, S. Tokonami, T. Iida, Surfactant-Controlled Photothermal Assembly of Nanoparticles and Microparticles for Rapid Concentration Measurement of Microbes. *ACS Applied Bio Materials*. **2**, 1561–1568 (2019).
135. B. Bangalore Rajeeva, L. Lin, E. P. Perillo, X. Peng, W. W. Yu, A. K. Dunn, Y. Zheng, High-Resolution Bubble Printing of Quantum Dots. *ACS Applied Materials and Interfaces*. **9**, 16725–16733 (2017).
136. B. B. Rajeeva, P. Kunal, P. S. Kollipara, P. v. Acharya, M. Joe, M. S. Ide, K. Jarvis, Y. Liu, V. Bahadur, S. M. Humphrey, Y. Zheng,

Accumulation-Driven Unified Spatiotemporal Synthesis and Structuring of Immiscible Metallic Nanoalloys. *Matter*. **1**, 1606–1617 (2019).

137. S. Fujii, R. Fukano, Y. Hayami, H. Ozawa, E. Muneyuki, N. Kitamura, M. aki Haga, Simultaneous Formation and Spatial Patterning of ZnO on ITO Surfaces by Local Laser-Induced Generation of Microbubbles in Aqueous Solutions of [Zn(NH3)4]2+. *ACS Applied Materials and Interfaces*. **9**, 8413–8419 (2017).
138. M. Kawaguti, The Critical Reynolds Number for the Flow past a Sphere. *Journal of the Physical Society of Japan*. **10**, 694–699 (1955).
139. A. B. Basset, On the motion of a sphere in a viscous liquid. *Philosophical Transactions of the Royal Society of London*. **179**, 43–63 (1888).
140. T. Franosch, M. Grimm, M. Belushkin, F. M. Mor, G. Foffi, L. Forró, S. Jeney, Resonances arising from hydrodynamic memory in Brownian motion. *Nature*. **478**, 85–88 (2011).
141. H. A. Lorentz, Ein allgemeiner Satz, die Bewegung einer reivenden Flüssigkeit betreffend, nebst einigen Anwendungen desselben. *Abhandlungen über theretische Physik*, 23–42 (1907).
142. A. Simha, thesis, Austin (2017).
143. H. Faxén, thesis, Uppsala (1921).
144. P. Sharma, S. Ghosh, S. Bhattacharya, A high-precision study of hindered diffusion near a wall. *Applied Physics Letters*. **97**, 104101–3 (2010).
145. H. Brenner, The slow motion of a sphere through a viscous fluid towards a plane surface. *Chemical Engineering Science*. **16**, 242–251 (1961).
146. L. Liu, A. Woolf, A. W. Rodriguez, F. Capasso, Absolute position total internal reflection microscopy with an optical tweezer. *Proceedings of the National Academy of Sciences*. **111**, E5609–E5615 (2014).
147. B. U. Felderhof, Effect of the wall on the velocity autocorrelation function and long-time tail of Brownian motion. *Journal of Physical Chemistry B*. **109**, 21406–21412 (2005).
148. B. U. Felderhof, Erratum: Effect of the wall on the velocity autocorrelation function and long-time tail of Brownian motion. *Journal of Physical Chemistry B*. **110**, 13304–13304 (2006).
149. S. Jeney, B. Lukić, J. A. Kraus, T. Franosch, L. Forró, Anisotropic memory effects in confined colloidal diffusion. *Physical Review Letters*. **100**, 240604–5 (2008).
150. K. Huang, I. Szlufarska, Effect of interfaces on the nearby Brownian motion. *Nature Communications*. **6**, 8558–6 (2015).